Cell Manipulations with Dielectrophoresis

by

James Ting-Yu Lin

A thesis
presented to the University of Waterloo
in fulfillment of the
thesis requirement for the degree of
Master of Applied Science
in
Systems Design Engineering

Waterloo, Ontario, Canada, 2007

Author's Declaration

I hereby declare that I am the sole author of this thesis. This is a true copy of the thesis, including any required final revisions, as accepted my examiners.

I understand that my thesis may be made electronically available to the public.

Abstract

Biological sample analysis is a costly and time-consuming process. It involves highly trained technicians operating large and expensive instruments in a temperature and dust controlled environment. In the world of rising healthcare cost, the drive towards a more cost-effective solution calls for a point-of-care device that performs accurate analyses of human blood samples. To achieve this goal, today's bulky laboratory instruments need to be scaled down and integrated on a single microchip of only a few square centimeters or millimeters in size. Dielectrophoresis (DEP), a phenomenon where small particles such as human blood cells are manipulated by non-uniform electric fields, stands to feature prominently in the point-of-care device. An original device that enhances DEP effect through novel geometry of the electrodes is presented. When activated with two inverting sinusoidal waveforms, the novel-shaped electrodes generate horizontal bands of increasing electric fields on the surface of the microchip. With these bands of electric fields, particles can be manipulated to form a straight horizontal line at a predictable location. Experimental results showing the collection, separation, and transportation of mammalian cells are presented. A strategy for simultaneous processing of two or more types of particles is also demonstrated. With capabilities for an accurate position control and an increased throughput by parallel processing, the novel microchip device delivers substantial improvements over the existing DEP designs. The research presented here explores the effects of novel electrode geometries in cell manipulations and contributes to the overall progress of an automated blood analysis system.

Acknowledgements

I would like to thank my parents Jiann-Ping Lin and Kee-Ping Kao for their support in my pursuit of a graduate degree. I also like to thank my supervisor, Dr. John T. W. Yeow, for his vision in MEMS technology. Without him, none of my research would be possible. I like to thank Dr. Perry Chou, Dr. Shirley Tang, and Dr. Eric Jervis for their advices and their support. Thank you goes to Michelle Zhou, Stéphanie Follonier, Parnian Ghaffari, and Liam Kelly for their expertise in laboratory biology. In addition, I would like to acknowledge the members of the lab who have always listened and never failed to provide valuable insights. Their friendship will be treasured for a long time.

Table of Contents

Author's Declaration ii
Abstract iii
Acknowledgements iv
Table of Contents v
List of Figures vii
List of Tables x
Chapter 1 Introduction 1
1.1 Definition of Cell Manipulation 1
1.2 Motivations for Microscale Cell Manipulation and Point-of-care Testing 2
1.3 Lab-On-A-Chip and Miniaturized Total Analysis System 5
1.4 Fabrication Tools 7
1.5 Aim of Work and Thesis Organization 8
Chapter 2 Dielectrophoresis 10
2.1 Derivation of DEP Force Formula 12
2.2 Factors of DEP Forces 19
2.3 Rotational and Translational Dielectrophoresis Effects 21
2.4 Comparison of Dielectrophoresis and Electrophoresis 23
Chapter 3 Introduction to Common DEP Devices 27
3.1 Introduction to Common DEP Devices 27
3.1.1 Two-Layer Parallel Electrode 27
3.1.2 Comb Electrode Design 28
3.1.3 Concentric Electrode Design 28
3.1.4 Circular Electrode Array Design 29
3.1.5 Parabolic Electrodes 30
3.1.6 Castellated Electrodes 31
3.1.7 Spiral Electrodes 32
3.1.8 Insulator-Based Devices 34
3.2 Manipulation Techniques 36
3.2.1 Field Flow Fractionation 36

3.2.2 Traveling Wave Dielectrophoresis 40
3.2.3 Deflector Design 42
3.2.4 Three-Dimensional Devices 44
Chapter 4 Current Cell Separation Design 47
4.1 Uniquely Shaped Electrode Design 47
4.2 Microfabrication 55
4.3 Device Packaging 57
4.4 Electrical control 59
4.5 Fluidic Control 60
4.6 Optics 61
4.7 Bead Experiment 61
4.8 Cells Experiments 62
4.8.1 HeLa 62
4.8.2 Yeast 63
4.8.3 Hematopoietic stem cell 64
Chapter 5 Experimental Results 66
5.1 Enhancing Dielectrophoresis Effects with Novel Electrode Geometry 66
5.2 Cell Collection, Separation and Transportation 74
5.3 Flip-flop Electrodes and 4-Directional Movement 78
Chapter 6 Future Outlook 86
6.1 Three Dimensional Design Enhancement 86
6.1.1 Simulation and Explanation 87
6.1.2 Advantages and Challenges 89
6.2 Cell Superhighway Concept 91
6.2.1 Simulation and Explanation 92
6.2.2 Advantages and Challenges in Superhighway Design 94
6.3 Field Programmable Gate Array Enhancement 96
6.3.1 New Circuit Design 96
6.3.2 Software Design 97
6.3.3 Improvements over Existing Design 100
6.4 Conceptual Blood Analysis System 101
6.5 Summary and Outlook 103

List of Figures

Figure 1 i-STAT Cost Projection [11] 4
Figure 2 Comparison of laboratory-based blood testing and point-of-care system [13] 5
Figure 3 A dipole in a non-uniform electric field 17
Figure 4 Frequency response of Re[K] when $\sigma_p < \sigma_m$ and $\varepsilon_p > \varepsilon_m$ 17
Figure 5 Frequency response of Re[K] when $\sigma_p > \sigma_m$ and $\varepsilon_p < \varepsilon_m$ 18
Figure 6 TWD Signals running at 1 MHz, 2 Volts (peak-to-peak) 22
Figure 7 Typical graph of Clausius-Mossotti factor vs. frequency 23
Figure 8 (A) Charged particle and (B) neutral particle under uniform electric fields 25
Figure 9 (A) Charged Particle and (B) neutral particle under non-uniform electric fields 25
Figure 10 Common electrode array designs: a) two-layer parallel array, b) two parallel arrays on sides of channel, c) array of concentric squares, d) array of metallic circles [51, 58-60] 30
Figure 11: Square Spiral Electrode Design 33
Figure 12: Circular Spiral Electrode Design 33
Figure 13 Typical designs of DEP electrodes: a) quad-pole parabolic electrodes, b) castellated electrodes, c) spiral electrodes, d) insulator-based device [31, 32, 35, 43, 61] 35
Figure 14: Schematic Diagram of a Flow- Through Cell Separation Device 37
Figure 15: A schematic of two chamber flow through device 38
Figure 16 a) Design of typical FFF device showing force vectors on particles, b) Flow profile and separation of particles 39
Figure 17: Typical deflector electrode design 43
Figure 18 Typical deflector design using insulator blocks 44
Figure 19 a) Top view of 3D grid electrodes, b) side view of 3D grid electrodes, c) side view of 3D elliptic electrode 45
Figure 20 Template of DEP chip showing 36 bonding pads 48
Figure 21 Parallel electrode array design 48
Figure 22 Wide triangular-shaped electrode array 49
Figure 23 Narrow triangular-shaped electrode array 50
Figure 24 Flip-flop electrode array design 51
Figure 25 Spiral Electrodes with 20 μm and 50 μm gaps 52

Figure 26 Final masks consisting of 4 separate designs 53
Figure 27 a) Wafer RCA-cleaned, b) deposition of chromium (grey) and gold (yellow), c) deposition of photoresist layer (dark blue), d) photoresist layer developed and etched, e) chromium and gold etched, f) removal of photoresist layer to expose gold electrodes 56
Figure 28 Schematic diagram of the DEP device showing the microchip and its packaging 57
Figure 29 Diagram of silicone rubber gasket showing dimensions 58
Figure 30 Photographs of the microchip after the completion of the microfluidic channel. (a) the microchip from the side with its dimension marked by a ruler, (b) a stereomicroscope photograph of the microfluidic channel and the electrode array underneath it 59
Figure 31 Block diagram of the electronic control for generating DEP and TWD signals 60
Figure 32 A photograph of the experimental setup showing (1) peristaltic pump, (2) inlet tube, (3) 10x objective lens, (4) outlet tube, and (5) the microchip device 61
Figure 33 Blue microbeads next to a group of 15 Hematopoietic stem cells 65
Figure 34 Configuration of the triangular-shaped electrode array 66
Figure 35 Surface diagrams of electric field of (a) triangular-shaped electrodes, (b) parallel track electrodes 68
Figure 36 Photographs of banding effect in a 1 mS/cm under 100 kHz DEP waveforms. (a) the positions of microbeads right after the activation of DEP signals, (b) the position of the microbeads after 43 seconds, (c) the position of the microbeads after 75 seconds, (d) the position of microbeads at 125 seconds 70
Figure 37 Vertical positions of the microbead bands with respective frequencies of the applied waveforms 71
Figure 38 Photographs of TWD effect on microbead band. From (a) to (d) the microbead band moved to the left without breaking formation. Its vertical position was maintained throughout. 73
Figure 39 Separation of two particles into distinct lanes 74
Figure 40 Conceptual drawing of the separation of 3 different types of particles into lane A, B, and C 74
Figure 41 (a) – (d) Concentration of HeLa cells in the middle of channel, (e) – (h) Transportation of cells to end of channel 75
Figure 42 (a) – (d) Simultaneous transportation and separation of microbeads and yeast 77
Figure 43 Color-coded flip-flop electrodes 79
Figure 44 Modified switch circuits for flip-flop electrodes 79

Figure 45 Photographs of shifting in vertical band positions 84
Figure 46 Conceptual drawing of a cell separator with 6 exits 85
Figure 47 Three dimensional parallel track design with electrode voltage 5 and -5 V 86
Figure 48 Simulation of electric field strength for 3D design 87
Figure 49 Transition of electric field minima from left to right 88
Figure 50 Cell superhighway concept 92
Figure 51 Cell superhighway with DEP voltage 5V and -5V 93
Figure 52 Modified electrodes with more elongated form 94
Figure 53 Schematic of isolation circuit 97
Figure 54 Flow chart diagram for FPGA 99
Figure 55 Role of FPGA in TWD experiments 100
Figure 56 Conceptual drawing of a blood analysis system 103

List of Tables

Table 1 Comparison of Different Etch Techniques 8
Table 2 Examples of particle types investigated by DEP 11
Table 3 List of typical conductivities at 20°C [49] 20
Table 4 List of common medium and their dielectric constants [50] 21
Table 5 Comparison of dielectrophoresis and electrophoresis [27] 26
Table 6 Summary of different electrode designs 54
Table 7 Electrode color code for upper and lower electrodes 80
Table 8 Waveform pattern for vertical movements 81
Table 9 Waveform pattern for medium band 82
Table 10 Waveform pattern for horizontal movements 83
Table 11 Electric field minima pattern 89
Table 12 Comparison of waveform generator and FPGA 101

Chapter 1
Introduction

1.1 Definition of Cell Manipulation

Cell manipulations refer to any interactions with a biological cell that result in a change in its normal behavior. Under this broad definition, examples of cell manipulations include the alteration of a cell's physical shape, the introduction of foreign particles into a cell, the transportation of a cell to the desired location, and even the killing of a cell. Various cell manipulation techniques such as electroporation and dielectrophoresis (DEP) are established procedures where the cause and effect are carefully monitored and well understood.

Today cell manipulation instruments are prevalent in all facilities that deal with biological samples (biosamples). However, even the most advanced laboratory today is still depended on large and expensive instruments that deal with biosamples in bulk. One ubiquitous example is the centrifuge. A centrifuge is a piece of laboratory equipment that puts a substance in rotation around a fixed axis in order for the centrifugal force to separate lighter and heavier substances. They are used in biology for isolating and separating compounds on the basis of molecular weight [1, 2]. One common usage of centrifuge is the separation of white and red blood cells. The white blood cells, being heavier than the red blood cells, will collect at the bottom of a test tube after centrifuging. The red blood cells along with the supernatant are siphoned out of the test tube leaving only the white blood cells behind for further studies. Another example is the electroporator. An electroporator performs electroporation, a phenomenon which creates pores on the cell membrane and hence increases its permeability [3]. An electroporator has two electrodes that can source large voltages across a cuvette loaded with a solution that contains cells and foreign particles. The voltage pulse creates temporary pores on the cell membrane which allow the foreign particles to diffuse inside the cells. The foreign particles often include DNA strands or molecular probes. Centrifuges and electroporators are examples of macroscale cell manipulations where the samples are collected or grown into applicable volumes before they are treated.

1.2 Motivations for Microscale Cell Manipulation and Point-of-care Testing

Macroscale cell manipulations have some very prohibitive disadvantages. First, dealing with large sample size requires large and expensive testing instruments that only a few laboratories can afford. The creation of a centralized laboratory means the biosamples need to be collected, stored, and transported from the local blood clinics. Time delay, lost samples, and mislabeling are just some of frequent accidents that may hamper timely diagnosis [4]. Gascoyne et al. reported that "90% of the cost and 95% of the time needed to obtain molecular diagnostic data today is associated with sample collection, transportation, and preparation" [5]. Furthermore, the separation of red and white blood cells via a centrifuge will often require a blood sample in the range of millimeters which contains millions of blood cells. Extractions of blood at this amount are undesirable for any patients that require frequent blood tests. There are inherent health concerns as well as cost issues with traditional ways to perform blood tests.

In the world of rising medical costs, the push is toward a simpler, safer, and less expensive alternative. Miniaturization of biological analysis tools will improve throughput, performance, and accessibility [6]. Miniaturized biological analyzers require sample size in the range of microliters or even picoliters, two or three magnitudes smaller than the traditional devices. As the sample size is reduced, little or no reagent will be used at all. The automation of miniaturized instruments will mean the creation of a decentralized health network. The new laboratory-clinical interface is represented by the "point-of-care (POC) testing" model. POC testing, or bedside testing, is the concept that accurate diagnostic test can happen near the site of the patient care rather than in the laboratory [7]. The ultimate version of POC testing is an over-the-counter product that consumers can purchase and use at the privacy of their own home. However, intermediate steps that put portable analyzers into the hands of healthcare professionals have already taken place. A successful analyzer should deliver fast and accurate results in a cost-effective manner. Several successful POC testing devices have been released into the US market and POC testing is a growing $4 billion industry in 2003 [4]. One of the more successful POC testing devices is the i-STAT whole blood analyzer from i-STAT Corporation. i-STAT whole blood analyzer is a cartridge-based

device. With the proper cartridge, it is capable of performing blood gas tests (oxygen and carbon dioxide content in blood), pH level measurement, detections for blood minerals (sodium, potassium and chloride), and blood urea level measurement. i-STAT analyzers have been deployed in surgical units to provide the last-second updates on patients' conditions [8-10]. Cost is one of the main motivations for POC testing devices. Figure 1 shows the cost projection of a traditional blood test versus an i-STAT analyzer by i-STAT Corporation. The biggest saving is in the reduction of labor cost where i-STAT claims to save 41 cents out of every dollar spent on blood tests and the overall saving is 48 cents out of every dollar [11]. In addition, POC testing has proven to save time by eliminating sample handling and decision making. Figure 2 compares the steps taken by traditional laboratory-based blood testing and the POC testing. One study shows that POC testing is able to reduce the turn-around-time for cardiac markers from 72 minutes to 20 minutes [12].

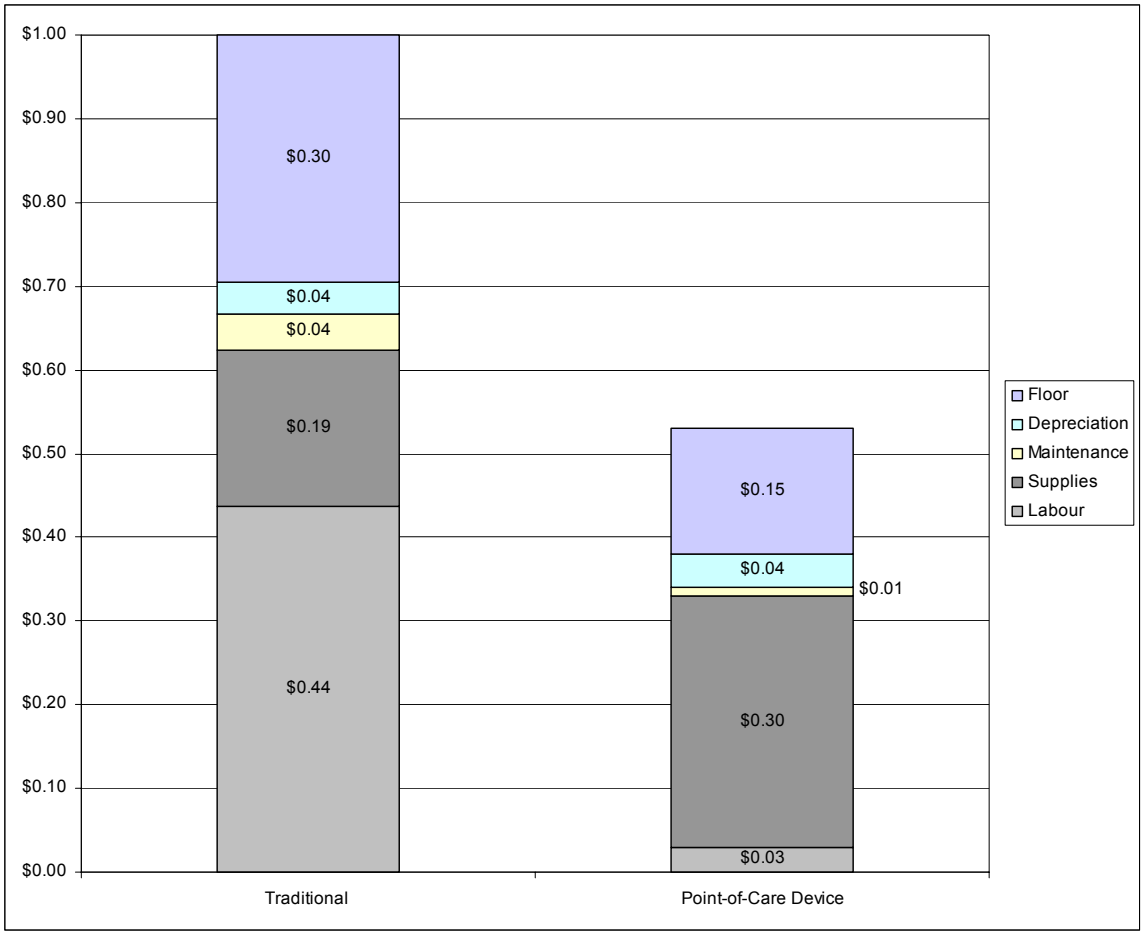

Figure 1 i-STAT Cost Projection [11]

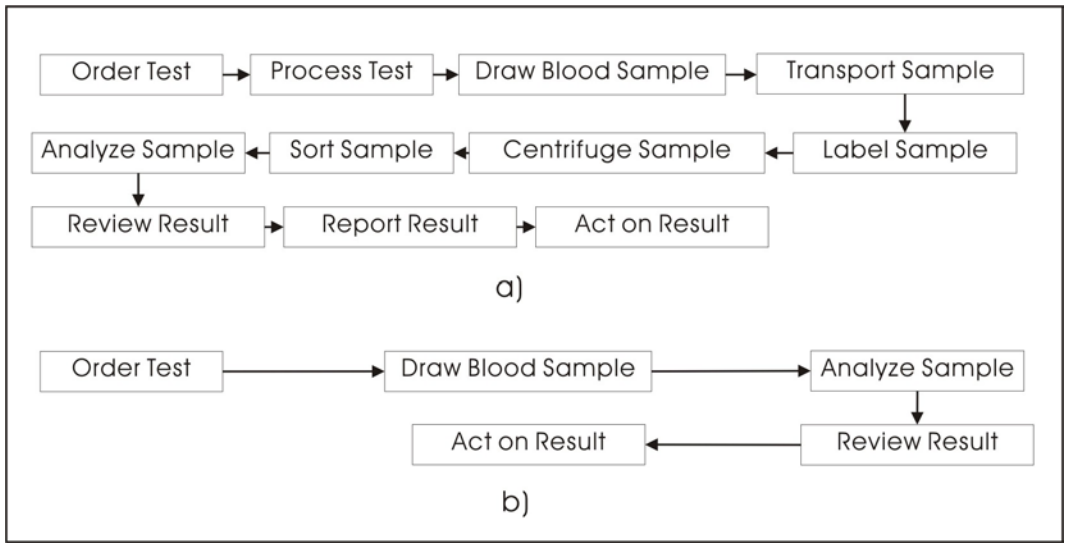

Figure 2 Comparison of laboratory-based blood testing and point-of-care system [13]

1.3 Lab-On-A-Chip and Miniaturized Total Analysis System

The push towards smaller and faster cell manipulation techniques has largely been fuelled by the Lab-On-a-Chip (LOC) initiative. Like its name suggests, LOC centers on the concept that today's bulky laboratory instruments can be scaled down and integrated on a single chip of only millimeters to a few square centimeters in size. This miniaturization is made possible by breakthroughs in semiconductor techniques that enable microstructures to be built on silicon-based substrates [14]. The increase in efficiency is caused by the enhanced chemical and physical effects from scaling. For example, diffusion occurs at a higher rate due the short distances between particles [15]. Heating is much faster due to the large surface to volume ratio in a miniaturized system [16]. The throughput is increased because of massive parallelization that is possible with small microchannels. In addition, low fluid consumption means less waste and less expensive reagents. Microfabrication of semiconductor material allows LOC devices to be mass produced and hence reduces fabrication costs. LOC technology reaches across a variety of disciplines including: chemistry, biology, bioengineering, physics, electronics, medical science, chemical engineering, and materials

science. Strictly speaking, LOC technology does not restrict itself in the analytical world. Any laboratory process, including manufacturing of chemical reagent, can potentially be an application for LOC. A subset of LOC that concentrates on the integration of total sequence of laboratory processes to perform chemical analysis is the miniaturized total analysis systems (μTAS). Manz and Widmer in 1990 first coined the term μTAS, from the downsizing of a total analysis system (TAS) [17, 18]. The technology springs from a need of rapid, on-line measurements at low concentration within the fields of chemical production, DNA analysis, drug discovery, pharmaceutical screening, medical diagnostic and environmental analysis [19]. A typical μTAS should perform the following tasks in order: sampling, sample pre-treatment, chemical reactions, analytical separations, analyte detection, product isolation and data analysis. For example, a successful μTAS device for HIV detection should [20],

1) transport the obtained blood sample to the detection site,

2) extract the white blood cells from the blood stream,

3) dissolve the cell membranes of the white blood cells,

4) detect the presence of HIV and

5) produce an analytical report on the findings.

To perform this wide array of tasks, a μTAS must employ techniques that benefit from miniaturization. Typically, a μTAS consists of a channel network through which all samples flow, a high-sensitivity detection, and a reactor chamber where mixing of the samples and chemical reagents take place. One of the most successful examples is the DNA microarray [21]. A DNA microarray contains an array of probes made of DNA fragments. The probe fragments bind to their appropriate complementary DNA in a hybridization process which activates varying colors of fluorescent emissions. The probes that are occupied with their complementary pairs are then counted. The quality and the quantity of the unknown DNA are determined by the strength of the fluorescence and the comparison to other known gene

expressions [22]. DNA microarray is considered as a breakthrough in DNA analysis systems because it is an fully integrated system containing compartments for growth, detection, and analysis.

1.4 Fabrication Tools

μTAS and LOC are subsets of the MicroElectroMechanical systems (MEMS) or micromachines. MEMS research encompasses a wide selection of systems that have at least one dimension in the micron range. Most of the MEMS system devices are implemented on silicon, the material for integrated circuits. However, some MEMS have use polymers and metals [23]. MEMS based on silicon are fabricated using various techniques perfected in semiconductor processes. Deposition of materials is implemented with electroplating, sputter deposition, physical vapor deposition, and chemical vapor deposition. The patterning of silicone is a two-step process involving photolithography and etching. Depending on the aspect ratio, etching depth and material characteristics, one or several of the following etching techniques are used: wet etching, reactive ion etching, and deep reactive ion etching. Selectivity describes how specific the etching is to the material. Etch rate refers to the rate the materials are etched. A low aspect ratio (closer to 1) means that etching is equally fast in all direction. While a high aspect ratio means that vertical etching rate is higher than the horizontal etching. Their characteristics are listed in Table 1.

Table 1 Comparison of Different Etch Techniques

Type of Etching	Selectivity	Etch Rate	Aspect ratio
Wet etching	Good Selectivity	Moderate Etch Rate	Low aspect ratio
Reactive ion etching	Low Selectivity	Good Etch Rate	High aspect ratio
Deep reactive ion etching	Low selectivity	Good etch rate	Very high aspect ratio

1.5 Aim of Work and Thesis Organization

The goal of this research is to explore novel cell manipulation techniques using DEP. The novel DEP techniques involved several novel shaped electrodes that generate very specific electric fields on the surface of a microchip. The manipulation of cells is performed using DEP and traveling wave dielectrophoresis (TWD) phenomena. In the first part of the experiments, the collection of microbeads is demonstrated as well as the selective shifting of the microbeads from one electrode to another electrode. In the second part, different cells are used in separation and transportation experiments. The experiments results and this report make meaningful contributions toward a portable whole blood analysis system. This report is organized into six chapters. The objective is to provide information on DEP and the experimental results on particle positioning and particle separation. This report focuses heavily on the experimental results. In the first chapter, several key technologies in miniaturization are introduced. The motivations for miniaturization, including higher efficiency and lower cost, are presented. The second chapter focuses on the theory behind DEP. It discusses the fundamental mathematics of DEP, the various factors impacting DEP, and the generations of static and translational DEP effects. Whenever possible, examples are presented to demonstrate key concepts. Chapter 3 provides detailed background information

on the current devices based on DEP effects as well as the integrations of optical, electrical, and fluidic systems. These current devices include several types of DEP arrays, electrodeless device, castellated, and parabolic electrodes. The advantages and shortcomings of each designed are discussed. Chapter 4 presents the step-by-step design of the DEP microchip from fabrication, packaging, to integration. The preparation steps for particles such as yeast, mammalian cells, and microbeads are also mentioned in detail. In Chapter 5, several experiments are demonstrated using the device illustrated in Chapter 4. The results are recorded and presented in this chapter in an organized fashion. The types of experiments include particle positioning, trapping, transportation, and separation. The results are analyzed and compared to simulations. In the sixth and the last chapter of this report, future enhancements of the current design are discussed in detail. The three-dimensional DEP structures, the cell superhighway and the FPGA enhancements are a few examples of novel devices based on the current design shown in Chapter 4. A conceptual whole blood analysis system based on the experiment results in Chapter 5 is illustrated with detailed comments within this chapter. The conceptual system includes several compartments for cell collection, separation, transportation, and lysing.

Chapter 2
Dielectrophoresis

DEP is a much-written topic of many review papers [24-26]. It is first reported by Dr. Herbert Pohl at the Princeton University in 1958 [27, 28]. DEP effect was demonstrated by Dr. Herbert Pohl to be able to suspend tiny droplets of water in mid air. Dr. Herbert Pohl wrote in his journal paper about DEP that the most interesting aspect is its ability to work with neutral particles that are "larger than molecules" [27]. In the last ten years, the dielectrophoresis (DEP) effects have garnered a lot of interests from the research and industry communities. This is no doubt due to DEP's ability in manipulating biological particles. DEP is suitable for manipulating biological particles because it is observed with AC excitation which allows the use of high frequency voltage waveforms that do not induce the electrolysis and the corrosion of the electrodes. The type of particles demonstrated to have dielectrophoretic effects included mammalian cells [29-31], yeast [32, 33], bacteria [34-36], virus [37-40], DNA [41], protein [42], and polystyrene beads [43, 44]. The range of particles investigated by DEP is shown in Table 2 and it is clear that particles with a wide range of sizes from μm to nm are susceptible to DEP forces.

Table 2 Examples of particle types investigated by DEP

Type of Particles	Example	Demonstrated Effects	Reference
Mammalian cells	Daudi cells and NCI-H929 cells from lymphoma patients	DEP, TWD, and electrorotation	[31]
	Human liver cell line HepG2 and human umbilical vein endothelial cells	Positioning liver cells to reconstruct lobule radial pattern of real liver tissue	[45]
Yeast cells	Common baking yeast (*Saccharomyces cerevisiae*)	Measurements of single yeast cell rotation speed and direction	[32]
Bacteria	*Listeria monocytogenes*	Capturing bacteria using positive DEP with 90% efficiency in a continuous flow	[46]
Virus	Hepatitis A virus	Trapping and accumulation of Hepatitis A virus using DEP and electrohydrodynamic flow	[38]
DNA	pTA250, a negatively supercoiled plasmid	Collection of DNA onto interdigitated electrodes by high frequency	[47]
Protein	*R*-phycoerythrin	Trapping single protein molecules by DEP	[42]
Polystyrene beads	Fluorescent latex spheres	Measurements of DEP responses of various submicrometer particles	[43]

2.1 Derivation of DEP Force Formula

To fully understand DEP, the derivation of the DEP model starts with elementary electronic physics. The derivation shown in this section is a summary of work by Ghallab and Badawy [6] and Jones [25]. Figure 3 shows a standard dipole with the separation distance of the charges defined by the magnitude of vector $\vec{d}$. $\vec{r}$ represents the vector from the position of the dipole to the position where the field is being measured and the dipole is under a non-uniform electric field represented by vector $\vec{E}(\vec{r})$. In this case, the position of the dipole is measured from the point of origin, *O*. The assumption of the simplified dipole model is that the magnitude of $\vec{d}$ is very small compared to that of $\vec{r}$ and the charge +q and –q are equal in magnitude. The dipole moment is defined as

$$\vec{p} = q\vec{d}, \tag{1}$$

and the forces on the positive and the negative charge of the dipole are

$$\vec{F}_p = q\vec{E}(\vec{r} + \vec{d}), \tag{2}$$

and

$$\vec{F}_n = q\vec{E}(\vec{r}) \tag{3}$$

respectively. The net force on the dipole then is the sum of the Equation (2) and (3):

$$\vec{F} = q\vec{E}(\vec{r} + \vec{d}) - q\vec{E}(\vec{r}) \tag{4}$$

The first term of Equation (4) is then expanded using Taylor series,

$$q\vec{E}(\vec{r}+\vec{d}) = q\vec{E}(\vec{r}) + q\vec{d}\cdot\nabla\vec{E}(\vec{r}) + additional\ terms \tag{5}$$

The additional term in Equation (5) are ignored because in the stated assumption, the magnitude of $\vec{d}$ is very small and hence the higher powers of $\vec{d}$ are negligible. Combine Equation (4) and (5), the resultant force is

$$\vec{F} = q\vec{d}\cdot\nabla\vec{E} \tag{6}$$

Further, with dipole moment definition in Equation (1), we can simplify the force equation to:

$$\vec{F} = \vec{\rho}\cdot\nabla\vec{E} \tag{7}$$

The ideal electric dipole moment p is a measure of the polarity of a system of electric charges. For small spherical neutral particle in a dielectric medium with permittivity ε_m, its effective dipole moment p_{eff} is derived by starting with the electrostatic potential of a dipole which is defined as,

$$\phi = \frac{\vec{\rho}\cdot\vec{r}}{4\pi\varepsilon_m r^3} \tag{8}$$

When the dipole is replaced by a small neutral sphere with radius a and permittivity of ε_p, the perturbed electric fields around the sphere either bend toward the sphere or away from it. The new electrostatic potential has the form,

$$\phi = \frac{(\varepsilon_p - \varepsilon_m) \cdot a^3 \cdot \vec{E} \cdot \vec{r}}{(\varepsilon_p + 2\varepsilon_m) r^3} \tag{9}$$

Equation (9) is in the identical form as Equation (8). The ideal dipole moment p in (8) is replaced with the sphere's effective dipole moment p_{eff}. By comparison of (8) and (9), p_{eff} is derived as the following,

$$\vec{p}_{eff} = 4\pi \cdot a^3 \varepsilon_m \cdot K \cdot \vec{E} \tag{10}$$

where K is known as the Clausius-Mossotti factor and is defined by:

$$K = \left(\frac{\varepsilon_p - \varepsilon_m}{\varepsilon_p + 2\varepsilon_m} \right) \tag{11}$$

The equivalent, charge-free, electric dipole in Equation (10) produces the same perturbation field for all $| r | > a$ when placed in the same dielectric medium as the dipole in Equation (1). However, in DEP, electrical losses are the results of the frequency-dependency of dielectrophoretic force. To introduce this aspect into Equation (10), the concept of a complex permittivity is introduced. The neutral sphere with complex permittivity ε_p^* in a medium of complex permittivity ε_m^* in the same environment described in Equation (10) now experience a frequency-dependent force (F_{DEP}) defined as,

$$(\vec{F}_{DEP}) = 2\pi a^3 \varepsilon_m \, \mathrm{Re}[K^*] \nabla E^2_{rms} \tag{12}$$

where

$$K^* = \left(\frac{\varepsilon_p^* - \varepsilon_m^*}{\varepsilon_p^* + 2\varepsilon_m^*} \right) \tag{13}$$

is the complex Clausius-Mossotti factor, and ε_p^* and ε_m^* are defined by the following equations respectively,

$$\varepsilon_p^* = \varepsilon_p - j\frac{\sigma_p}{\omega} \tag{14}$$

$$\varepsilon_m^* = \varepsilon_m - j\frac{\sigma_m}{\omega} \tag{15}$$

where σ_p and σ_m are the conductivity of the particle and the medium, respectively, and ω is the angular frequency of the applied electric field. Re[K] is expanded by substituting ε_p^* and ε_m^* defined in Equation (14) and (15) into (12):

$$\mathrm{Re}[K] = \frac{\varepsilon_p - \varepsilon_m}{\varepsilon_p + 2\varepsilon_m} + \frac{3(\varepsilon_m\sigma_p - \varepsilon_p\sigma_m)}{\tau_{MW}(\sigma_p + 2\sigma_m)^2(1 + \omega^2\tau_{MW}^2)}, \tag{16}$$

where τ_{MW} is the Maxwell-Wagner charge relaxation time:

$$\tau_{MW} = \frac{\varepsilon_p + \varepsilon_m}{\sigma_p + 2\sigma_m}. \tag{17}$$

It will be useful to calculate the high frequency response and the low frequency response of RE[K] by making ω approach infinity and 0 respectively:

$$\mathrm{Re}[K] = \frac{\varepsilon_p - \varepsilon_m}{\varepsilon_p + 2\varepsilon_m}, \text{ for } \omega >> 0 \tag{18}$$

$$\mathrm{Re}[K] = \frac{\sigma_p - \sigma_m}{\sigma_p + 2\sigma_m}, \text{ for } \omega \to 0 \tag{19}$$

At high frequencies, it is clear that permittivity is the predominant factor in determining Re[K]. Conversely, conductivity dominates at low frequencies. It is possible to categorize DEP effects into two cases. In the first case, the conductivity of the medium is much greater the conductivity of the particle but the permittivity of the particle dominates the permittivity of the particle. Essentially, restrictions on the permittivity and conductivity values of the medium and the particle are that $\sigma_p < \sigma_m$ and $\varepsilon_p > \varepsilon_m$. The frequency response is then graphed in Figure 4. In Figure 4, Re[K] starts from a negative value at low frequencies and becomes positive at high frequencies. In the second case, the conditions are reversed so that $\sigma_p > \sigma_m$ and $\varepsilon_p < \varepsilon_m$. The frequency response of the second case is shown in Figure 5. Re[K] starts positive at low frequencies and becomes negative at high frequencies. In each of the frequency responses, there exists a cross-over frequency (ω_c) at which Re[K] switches signs. At ω_c, the DEP effects are reduced to a minimal and ω_c is calculated as [48]

$$\omega_c = \sqrt{\frac{(\sigma_m - \sigma_p)(\sigma_p + 2\sigma_m)}{(\varepsilon_m - \varepsilon_p)(\varepsilon_p + 2\varepsilon_m)}} \tag{20}$$

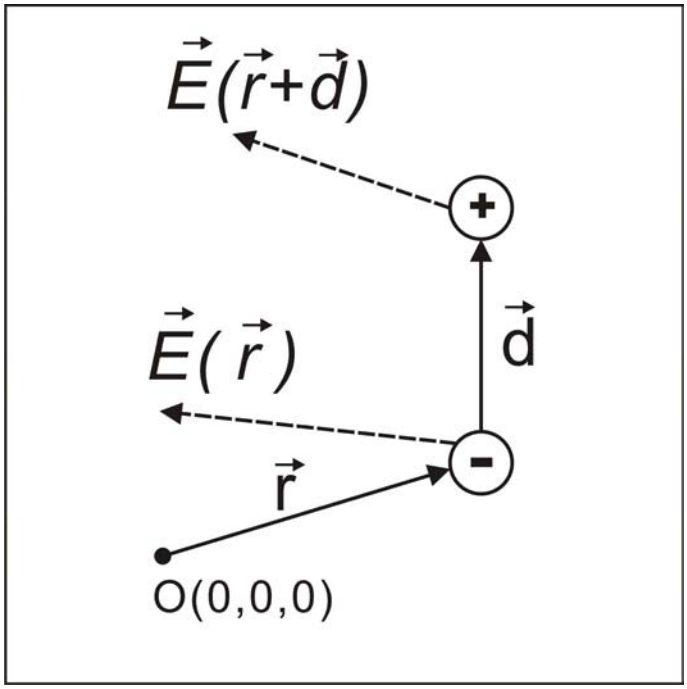

Figure 3 A dipole in a non-uniform electric field

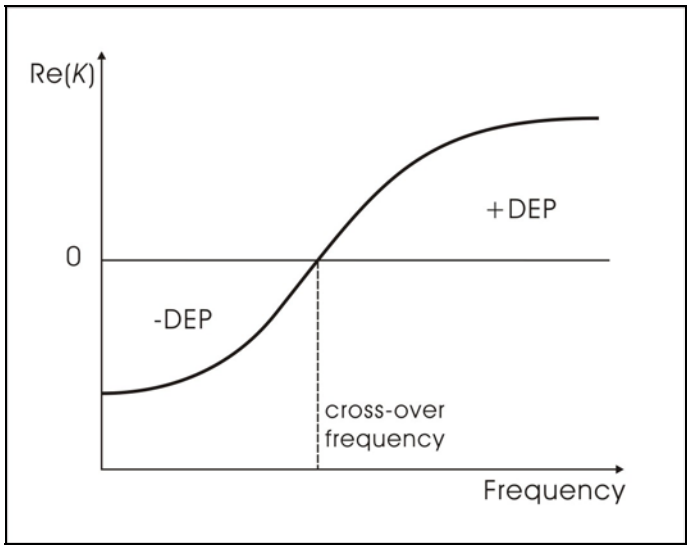

Figure 4 Frequency response of Re[*K*] when $\sigma_p < \sigma_m$ and $\varepsilon_p > \varepsilon_m$

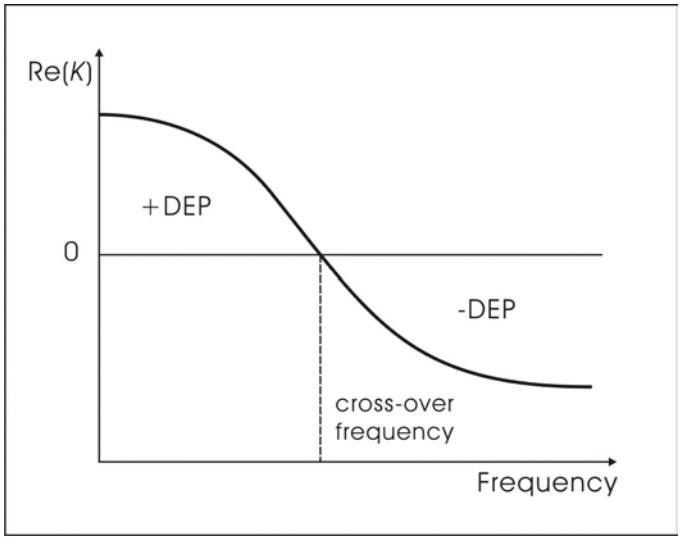

Figure 5 Frequency response of Re[K] when $\sigma_p > \sigma_m$ and $\varepsilon_p < \varepsilon_m$

2.2 Factors of DEP Forces

From Equation (12), it is clear that the magnitude of F_{DEP} is determined by the following factors: the size of the particle, the conductivity of the medium, the conductivity of the particle, and the magnitude of the electric fields. In contrast, the direction of F_{DEP} is determined by only one parameter, Re[K], the real part of the complex Clausius-Mossotti factor. It is the only parameter in Equation (12) that can become negative and the sign of Re[K] will be the indicator of the direction of the F_{DEP}.

When Re[K] > 0, F_{DEP} is positive and it directs particles toward regions of high electric field strengths. This attraction effect is called positive DEP (pDEP). When Re[K] < 0, an opposite effect, negative DEP (nDEP), dominates and the particles seek out regions of low electric field strengths. Further analysis of the complex Clausius-Mossotti factor in Equation (13) reveals a frequency dependency which is not apparent at the first glance. Since K^* is a complex number, frequency plays an important part in determine the sign of Re[K]. By adjusting the frequency of the signals and maintaining all the other variables, the target particles can display opposite behaviors. Frequency analysis of Re[K] in Figure 4 and Figure 5 reveal distinct regions of pDEP and nDEP. At the cross-over frequency, F_{DEP} reaches a minimum and the particles display neither pDEP nor nDEP behaviors.

It is worth noting that among all the variables, the magnitude of the electric field has the biggest impact on the strength of the DEP force. Their relationship is defined as

$$F_{DEP} \propto \nabla E^2{}_{rms} \tag{21}$$

where F_{DEP} increases with the square of magnitude of the electric field (E). Since E is determined mostly by the distance between two electrodes, the geometry of the electrodes has significant effect on the F_{DEP} and the behaviors of the particles. In addition, the magnitude of F_{DEP} is influenced by the choice of the medium used in the experiment. F_{DEP} increases with the differences in the conductivity and permittivity values of the medium and

the particle. For particles with low conductivity, for example, a conductive solution results in a larger F_{DEP} than a biological fluid with low conductivity.

Conductivity is defined as the material's ability to conduct electricity. In Table 3, we list the conductivities for some common materials. For example, copper has one of the highest conductivity for metals. Water, on the other hand, can have good to poor conductivity values. Its conductivity depends on the ions dissolved in it. In DEP experiments, common salts such as NaCl and KCl are used to adjust the conductivity of water to the desired levels.

Table 3 List of typical conductivities at 20°C [49]

Element	*Electrical Conductivity (S/m^{-1})*
Silver	63.01×10^6
Copper	59.6×10^6
Seawater	5
Drinking water	0.0005 to 0.05
Deionized water	5.5×10^{-6}

Permittivity is different from conductivity. It measures how easily the electric fields can be formed in a uniform material. It is defined by the equation,

$$D = \varepsilon_0 \cdot \varepsilon_r \cdot E \ , \tag{22}$$

where D is the electric displacement field, ε_r is the relative dielectric constant of the medium, ε_0 is the permittivity of free space, and E is the applied electric fields. The measure of permittivity hinges on the value ε_r. Materials with higher dielectric constants are more permeable to electric fields than those with lower dielectric constants. Table 4 shows the dielectric constant for some common material. In the case of water, its conductivity varies greatly with the temperature. In this paper, the dielectric constant for water is approximately 80 since the experiments are carried out in room temperatures.

Table 4 List of common medium and their dielectric constants [50]

Material	*Dielectric constant* ε_r
Vacuum	1
Air	1.00054
Polyethylene	2.1
Polystyrene	2.4-2.7
Pyrex	4.7
Silicon	11.68
Methanol	30
Water at (0, 20, 100, 200 °C)	(88, 80.1, 55.3, 34.5)
Formamide	84.0

2.3 Rotational and Translational Dielectrophoresis Effects

Electrorotation (ROT) and traveling wave dielectrophoresis (TWD) are rotational and translational DEP effects respectively. ROT and TWD differ from the static pDEP and nDEP effects in two major aspects. First, the target particle under ROT or TWD is in constant motion while under pDEP and nDEP the particle remains stationary once it reaches the local electric field maxima or minima. Second, unlike pDEP and nDEP, the rotational and translational forces are influenced by the imaginary part of the complex Clausius-Mossotti factor, Im[K]. ROT is activated with a set of quad-pole sinusoidal voltage waves. Particles under influence of ROT begin to rotate around their central axis. The direction and the speed of the rotation are useful characterization tools to determine the conductivity and the permeability of the particle. ROT experiments are often performed before TWD experiments to determine the optimal frequency and medium conductivity. Unlike the rotational force provided by ROT effect, TWD generates a translational force on the particle. Particles under TWD move across the activated parallel electrodes and the distance traveled is determined by the total number of the electrodes in the array. In addition, TWD depends on both Re[K] and Im[K], the real and imaginary part of the complex Clausius-Mossotti factor. For TWD to

occur, Re[K] is negative to provide a lifting force on the particles by the means of nDEP. This is achieved by adjusting the conductivity of medium to be higher than that of the particle. Further, Im[K] needs to be sufficiently large to provide a translational force. To generate significant Im[K], traveling waves composed of sinusoidal waves of the same frequency with the 90° consecutive phase differences are used. Figure 6 shows the snapshot of the four sinusoidal waves with the phase of 0°, 90°, 180°, and 270° as represented by the color yellow, magenta, green and cyan. In Figure 7, the frequency responses of Im[K] and Re[K] are overlapped to produce the shaded TWD zone where Re[K] is negative and Im[K] is sufficiently large.

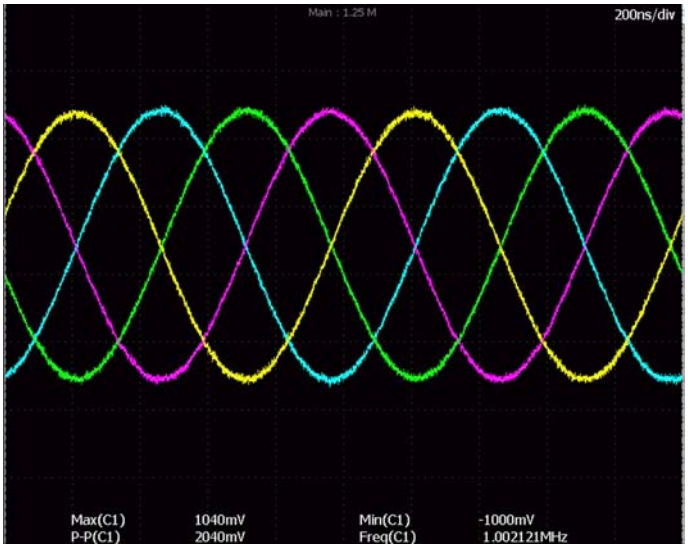

Figure 6 TWD Signals running at 1 MHz, 2 Volts (peak-to-peak)

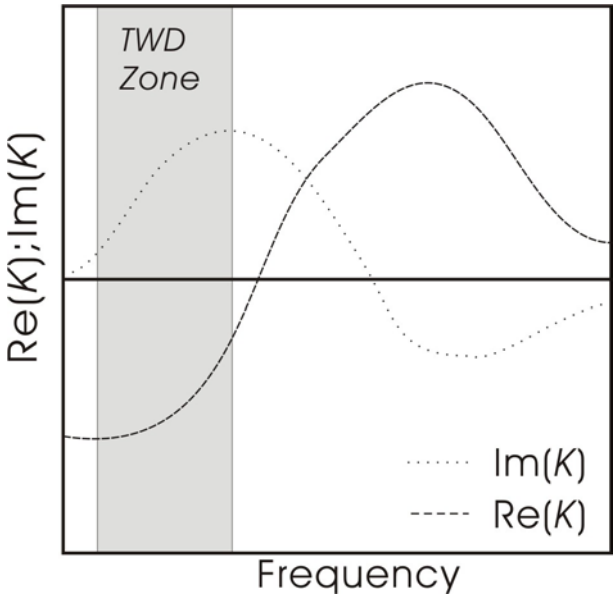

Figure 7 Typical graph of Clausius-Mossotti factor vs. frequency

2.4 Comparison of Dielectrophoresis and Electrophoresis

It is important to distinguish DEP from a similar effect, electrophoresis. Electrophoresis is a phenomenon where charged particles follow the path of the electric field lines. Since electrophoresis follows the principal that opposite charges attract and the similar charges repel, it works with both uniform and non-uniform electric fields. One of the most important applications of electrophoresis effect is DNA gel analysis where DNA strands loaded in a gel under constant electric fields are separated based on their electrophoretic mobility. The differences between electrophoresis and DEP are clearly defined. First, electrophoresis requires the particle to be charged while in DEP the particles are neutral. Second, in electrophoresis the charged particle moves along direction of the electric field lines. In DEP, the neutral particle moves to region of highest electric field strength regardless of the orientation of the electric fields. In fact, both direct current (DC) and alternating current (AC) electric fields can be used to induce DEP. In Figure 8, the charged particle (A) under uniform electric fields experiences electrophoresis effect and moves toward the negative electrode. The neutral particle (B) remains stationary because the attraction forces acting on the particle

from both positive and negative electrodes are equal in magnitude and opposite in direction. In Figure 9, the charged particle (A) under electrophoresis moves toward the negative electrodes in the direction of the electric field line. The neutral particle (B) under pDEP effect moves toward the region of the electric field maxima which is located near the edges of the shorter positive electrode. In Table 5, the two effects are compared in categories such as particle type, particle size, direction of motion, and field characteristics.

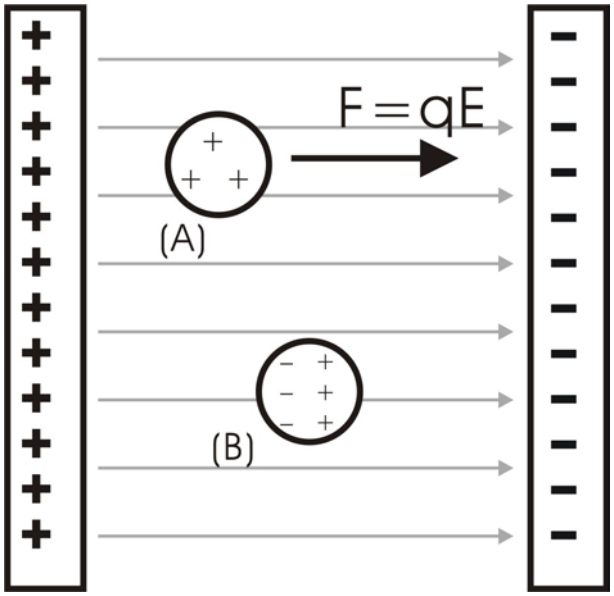

Figure 8 (A) Charged particle and (B) neutral particle under uniform electric fields

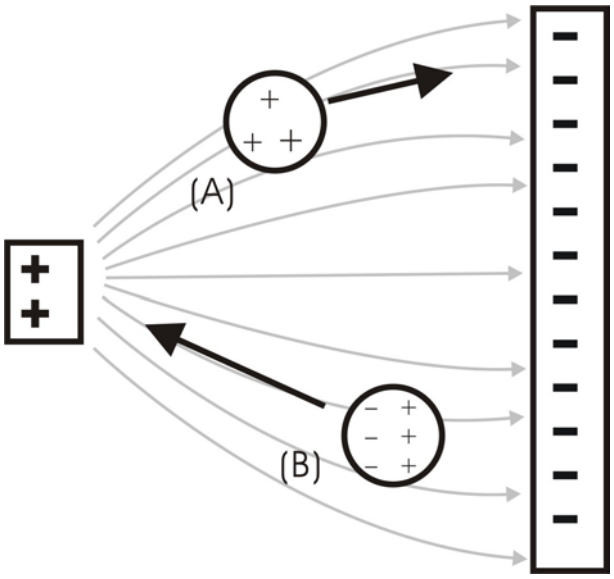

Figure 9 (A) Charged Particle and (B) neutral particle under non-uniform electric fields

Table 5 Comparison of dielectrophoresis and electrophoresis [27]

	Dielectrophoresis	***Electrophoresis***
Particle	Dielectric neutral particle	Particle with excessive charge
Particle Size	Micron and submicron	Any molecular size
Direction of Motion	Toward regions of highest field strength or regions of lowest field strength	Dependent on the direction of the field.
Type of Electric Fields	Non-uniform	Uniform and Non-uniform
Medium	Medium must have a different dielectric constant than the particle	Medium could have the similar dielectric constant than the particle
Field Strength	Must have high electric field strength	Use relatively low voltages
Field Characteristics	Both DC and AC electric fields	DC, no net movement under AC electric fields

Chapter 3
Introduction to Common DEP Devices

3.1 Introduction to Common DEP Devices

Some common DEP devices are shown in Figure 10 and Figure 13. The electrode array design is broken down into four separate designs shown in Figure 10 a) – d). The other DEP designs are shown in Figure 13 a) – d). Despite of having no electrodes, the inclusion of insulator-based device in the survey is justified by the use of non-uniform electric fields. Electrophoresis devices are not included in this chapter because electrophoresis is primarily a charged particle phenomenon as discussed in Section 2.4. The devices shown in Figure 10 and Figure 13 are representative of their categories but the list is not comprehensive and does not aim to cover all the designs found in DEP experiments. Instead, the target applications and the notable features of a few novel designs are discussed.

3.1.1 Two-Layer Parallel Electrode

The common parallel electrode array consists of rectangular electrodes that are long and thin in appearance. The electrodes are placed in such a way that they resemble the sleepers of a railway track and sometimes are known as the DEP track design. The gaps in between the electrodes are usually identical in width to the electrodes. Furthermore, the optimal width of a single electrode is similar to the diameter of the target particle. For manipulating mammalian cells, the electrode width is between 10 μm to 50 μm. The length of the electrodes varies but it rarely exceeds 1000 μm. The parallel electrode array is one of the most common designs to generate non-uniform electric fields for DEP experiments. Its advantages include the simplicity in design, the ability to perform both static DEP and TWD experiments, and the extensive simulation data available. The design for parallel electrode array used in TWD experiments is in need for novel solutions. Unless the electrodes are individually controlled, no more than three sets of wires can lie on a single plane without crossing. The fact that individually controlled electrodes need individual circuitry and

interconnect makes the design unattractive for large-scale TWD experiments. Figure 10 a) presents a two-layer electrode array. The purpose of the two metal layers is to extend the electrode array without adding additional overhead to the control circuits. The solution is to use novel microfabrication protocol which includes the etching of contact holes and multiple photolithography procedures [51]. The result is an array of 3000 electrodes with only four bonding sites. Each electrode is 10 μm wide and separated by a 10 μm gap. An additional increase in the number of electrodes is possible and the number of bonding sites stays constant. However, the cost and increased difficulties in microfabrication means the two-layer electrode array is hard to replicate in most of the laboratories.

3.1.2 Comb Electrode Design

Figure 10 b) shows the parallel electrode array device that has two electrode arrays at the opposite sides of the channel. The structure leaves a clear channel in between the electrode arrays. The transportation of the particles can then take place in the channel without the electrodes obscuring the view. Studies show that the comb-like device moves the target particles by two different techniques [24, 52, 53]. First, the target particles moved along the channel in the opposite direction of TWD signals. This occurs on top of the electrode and it is the same effect shown on parallel electrode arrays in Figure 10 a). In a separate mode, the target particles are pushed to the edge of electrodes in the clear channel. The particles then move in a zigzag manner in the same direction as the TWD signal. An anticlockwise rotation is also observed during the particle's movement. Since the two modes have directional and spatial differences, the comb design has demonstrated to separate two different particles by allowing them to travel in separate directions.

3.1.3 Concentric Electrode Design

Arrays of concentric electrodes with CMOS-like circuitry are becoming one of the most prevalent designs in particle trapping and sorting [54, 55]. The most common concentric designs are shown in Figure 10 c). Other shapes, including concentric circles and rings are commonly seen as well. The goal of the concentric design is to generate local non-uniform

electric fields. The repeatability of the concentric shapes means the device is scalable. The demonstration of a large scale concentric electrode array is as important as the design itself since the scaling makes the design attractive to cell assays applications. Each of the concentric squares in Figure 10 c) is addressable through a CMOS grid system. The device circuitry borrows the addressing system from a CMOS image sensor. The addressable circuitry makes the device highly customizable since each concentric electrode can be turned on for DEP trapping or off for DEP levitation. Each concentric electrode holds exclusively one target particle which makes cell patterning in the grid possible. Particle transportation from one electrode to another requires a coordinated sequence of release by the holding electrode using nDEP and immediately capture by a neighboring electrode using pDEP.

3.1.4 Circular Electrode Array Design

The array of metallic circles shown in Figure 10 d) is an early design in particle separation [56, 57]. The function of the array is to utilize nDEP and pDEP to separate two particles. The electric fields are the strongest near the edge of the electrodes while the minima exist in between the electrodes. In one application, *E. Coli* bacteria are separated from the blood cells. After washing the blood cells off the surface of the electrodes, bacterial DNA strands are released by high strength voltage via the electroporation of *E. Coli*. In a separate experiment, human cervical cancer cells are separated from human blood cells using the same procedure. The main advantage of this design is its scalability. Manufacturing the 80-μm-diameter platinum electrodes is considerably easier than creating each of the previous electrode array designs mentioned in this chapter. However, the need for a wash-off procedure means the accuracy of the particle separation is compromised.

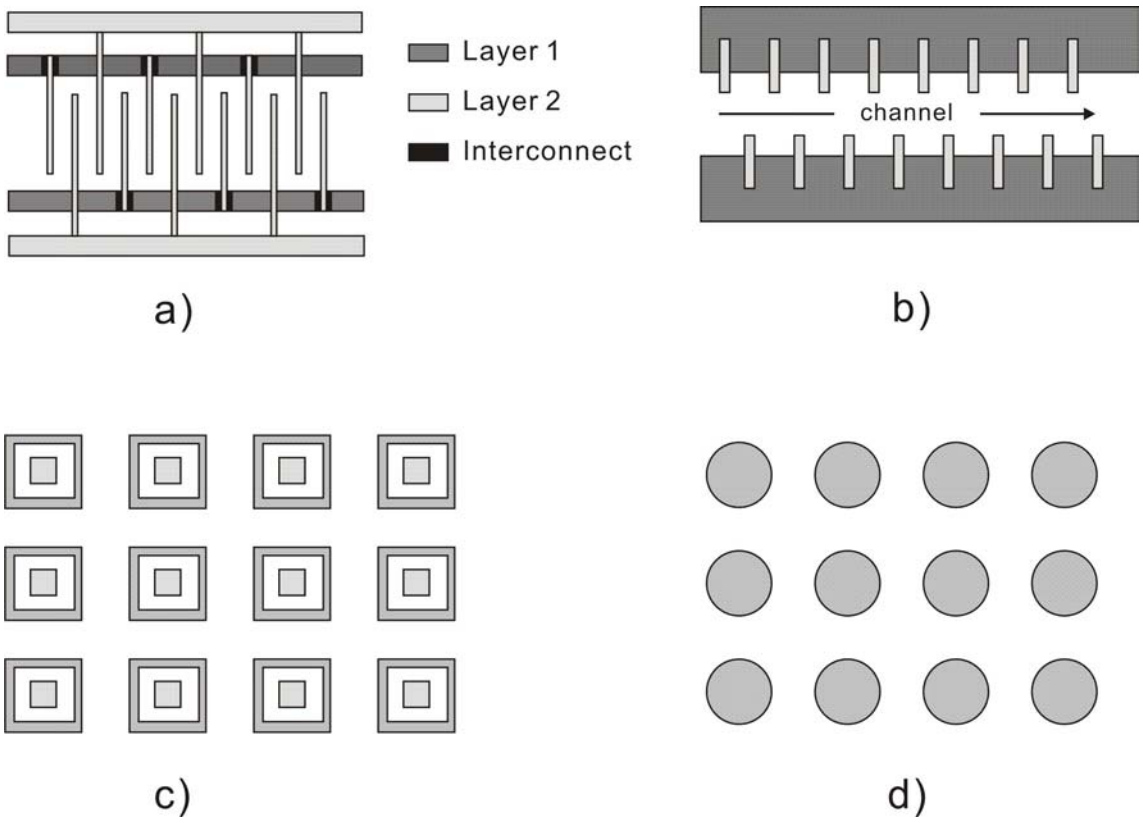

Figure 10 Common electrode array designs: a) two-layer parallel array, b) two parallel arrays on sides of channel, c) array of concentric squares, d) array of metallic circles [51, 58-60]

3.1.5 Parabolic Electrodes

Parabolic electrodes are often used in ROT studies where the rotation speed and direction of the particle are useful data in single cell characterization [32, 33]. A set of four electrodes at four corners are used, leaving a small uncovered space in between them. The desired particles are then loaded into the small space by activation of pDEP or nDEP. The loading of the particles is immediately followed by activation of quad-pole signals (0, 90, 180, 270 phase shifted sinusoidal waves) in the configuration shown in Figure 13 a). The activation of quad-pole signals results in a rotational movement of the particles in the loading zone. A video camera then monitors the movement. Rotation speeds and directions are then recorded and graphed against the frequency and voltage of the applied waveforms. Such data are

valuable for further experiments in cell sorting and transportation because ROT happens at the same frequency as TWD.

Another function of parabolic electrodes is the manipulation of small subcellular particles such as protein [61] and DNA [62]. These are often done with modifications to the parabolic geometry. In one experiment, four small electrode wires are used to maximize the electric fields in the loading zone. Since the subcellular particles are hard to image and their rotations are not easily observed, in the most of these proof-of-concept experiments, levitations and alignments to electric fields are used instead as evidences of DEP effects.

3.1.6 Castellated Electrodes

Castellated electrodes shown in Figure 13 b) are useful in generating multiple zones of electric field maxima and minima [63]. The four separated electrodes are castellated with intrusions and successive electrodes are activated with opposing voltages to generate strong non-uniform electric fields in between the electrodes. The electric field maxima are located at the middle of the channel between two opposing electrodes. The minima are located in the areas between the digits of the electrodes. Since the electric field maxima and minima are well defined, two particles can be separated by the nDEP and pDEP effects. Particles that experience nDEP will seek out the minima while those that experience pDEP effect will move to reside in between the electrodes. Further operations can then be used to remove the cells in the nDEP zones by fluidic pressure. Cells at pDEP zones will stick to the electrodes and hence stay. In one experiment, viable (live) cells are separated from nonviable (dead) cells using this method [64]. It also has been demonstrated that live cells can be trapped by nDEP in the electric field minima for live cell imaging and assay. The locations of the trapped cells are known and can be held there for indefinite amount of time. Another advantage is that since pDEP are used, the cells are not in contact with electrodes and their survival rate increases. The one drawback of the castellated design is that the movements of the cells are limited to fluidic pressure and are not useful for TWD.

3.1.7 Spiral Electrodes

Spiral electrode design for TWD, seen in Figure 13 c), is one of the more popular alternatives to the parallel track design. The reason for its popularity is simple – it is relatively easy to draw and inexpensive to manufacture. Spiral designs involve four parallel lines running in a growing concentric geometric shape such as a square or a circle. Examples of a square spiral design and a circular spiral design are shown in Figure 11 and Figure 12. As the four lines spiral outward, more and more parallel tracks are created for TWD. If a snap shot is taken at one of the four sides of the spiral square design, it will look like the parallel track design in Figure 10 a). Furthermore, extending the spirals will not increase the number of required metal contacts. This is a crucial advantage for spiral electrodes over the conventional parallel track design.

Research literature has shown that the spiral design is able to transport particles from the outer rings to the inner rings efficiently. However, there are several drawbacks. First, the area requirement grows exponentially as the number of tracks increases. The outside track has to circle a far bigger area then the inner tracks. In a structure as small as a MEMS device, area is scarce and a large spiral design has too much wasted area to be practical. Second, the spiral design spreads outward in a radial direction meaning that instead of transporting targeted particle from a fixed point to another, particles move into the inner circle from all angles regardless of their initial position. This shortcoming excludes the spiral design any applications that required a conveyor-belt like transportation. Furthermore, once the particles are gathered inside the concentric circle, it is difficult to move them elsewhere. Additional experiments have shown that the corners of the square spirals produce unwanted local electric maxima where cells are trapped.

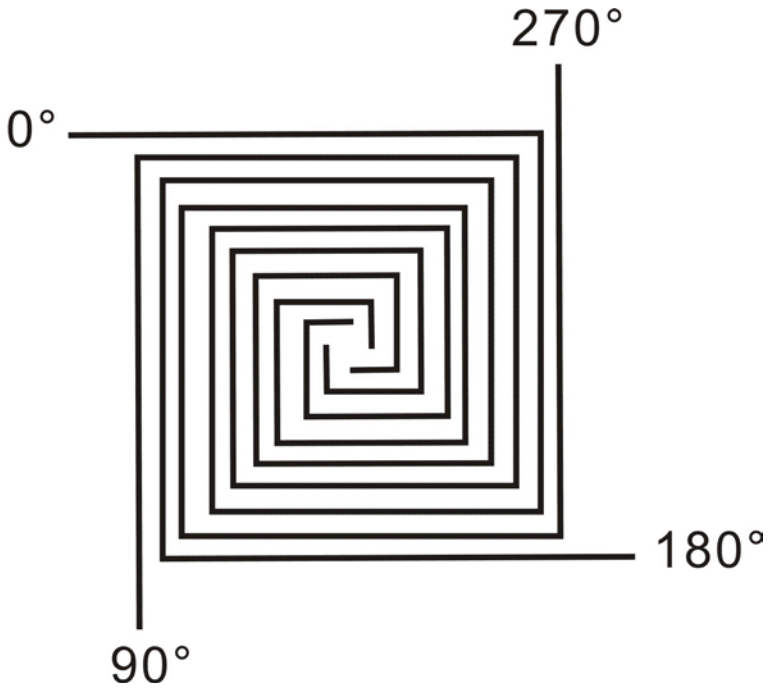

Figure 11: Square Spiral Electrode Design

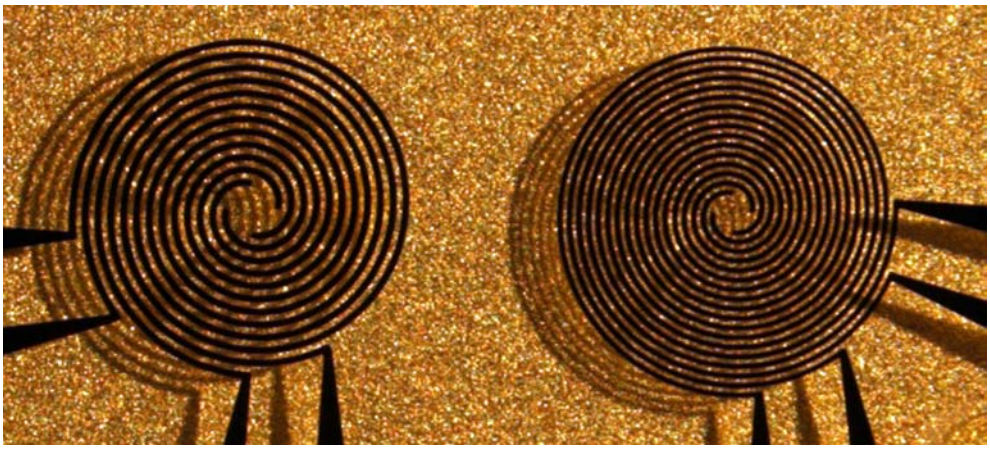

Figure 12: Circular Spiral Electrode Design

3.1.8 Insulator-Based Devices

Insulator-based devices use blocks of polydimethylsiloxane (PDMS) or polystyrene inside a fluidic chamber to manipulate the path of the electric fields. Since the permittivity of such insulator blocks is very low, the background electric fields generated by the opposing electrodes usually bend around them. This creates zones of non-uniform electric fields in between the insulator blocks. Like castellated electrodes, zones of electric field maxima and minima are present for particle separation [65] as well as trapping [66]. Insulator-based devices have several advantages. First, unlike metal, insulator blocks do not deteriorate over time and the surface uniformity is not a significant issue. Second, since insulator-based devices lack metallic electrodes, they are suitable for metal-sensitive biosamples. In addition, the insulator-based devices can be coupled with fluidic flow for high throughput cell sorting applications [67, 68]. Such device combines the high throughput quality of a flow through device and the customizability of a DEP device. An example of the insulator-based devices is shown in Figure 13 d).

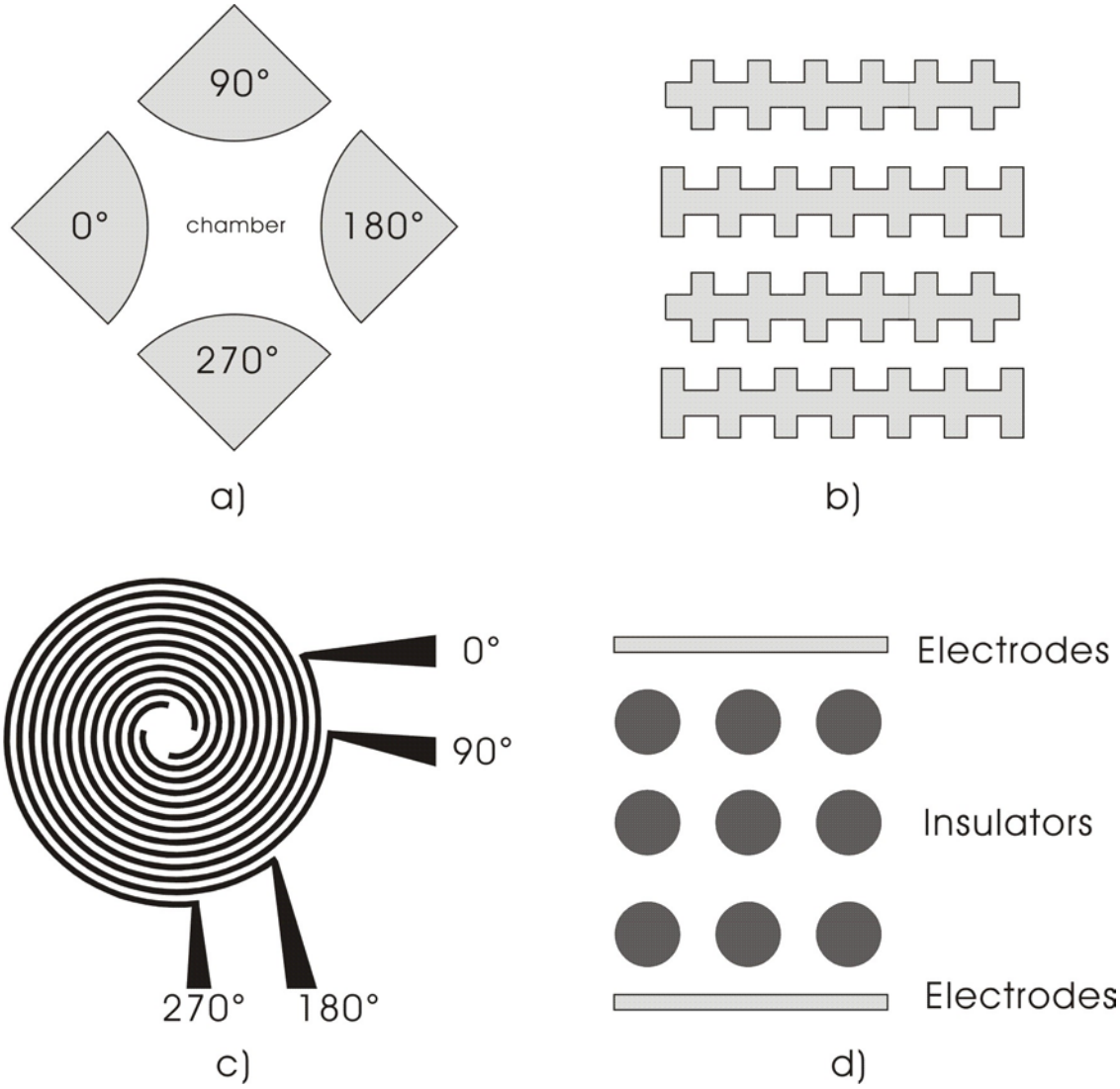

Figure 13 Typical designs of DEP electrodes: a) quad-pole parabolic electrodes, b) castellated electrodes, c) spiral electrodes, d) insulator-based device [31, 32, 35, 43, 61]

3.2 Manipulation Techniques

3.2.1 Field Flow Fractionation

The simplest method to achieve dielectrophoretic separation is by flow separation. The mixture of particles to be separated is pushed through a separation chamber consisting of an electrode array on the bottom of the chamber, enclosed by sides and a lid. There is a single inlet and outlet. The mixture is pumped across the electrode array using an external source such as a syringe pump, and the electrodes are energized so that the mixture separates – one population experiences pDEP, the other, nDEP. The former population is attracted to the electrodes and is trapped there, while the other is repelled into the center of the chamber and is pushed by the flow through to the outlet, where the particles can be collected. [69].

Figure 14 shows the schematic diagram of one such device [70]. In this device, the separation chamber is formed using an interdigitated electrode. The generated DEP force is the strongest at the surface and decreases exponentially into the chamber center. By applying a chosen frequency to the electrodes, the particles of interest are collected on the electrodes through pDEP while others are repelled into the middle of the channel and are removed by the fluid flow. Furthermore, the strength and the direction of the DEP forces depend on the conductivities of the target particles as well as the conductivity of the medium. If a medium with conductivity between that of the target particles and the rest of particles is found, a wide range of frequencies are available. If the conductivity of the target particles is similar to the rest of particles, it can mean that flow separation will not work as well as other methods.

Flow separation method has its challenges. First, the conductivity of target cells must be significantly different from the rest of the particles. Sometimes this is not possible and more than one particle will be attracted to the electrodes at all frequencies. This results in a mixed sample with more than one type of particles present. Second, the fluidic strength must be well controlled that it flushes away only the unwanted particles and not the target particles. But it also has to be strong enough to flush away the unwanted particles.

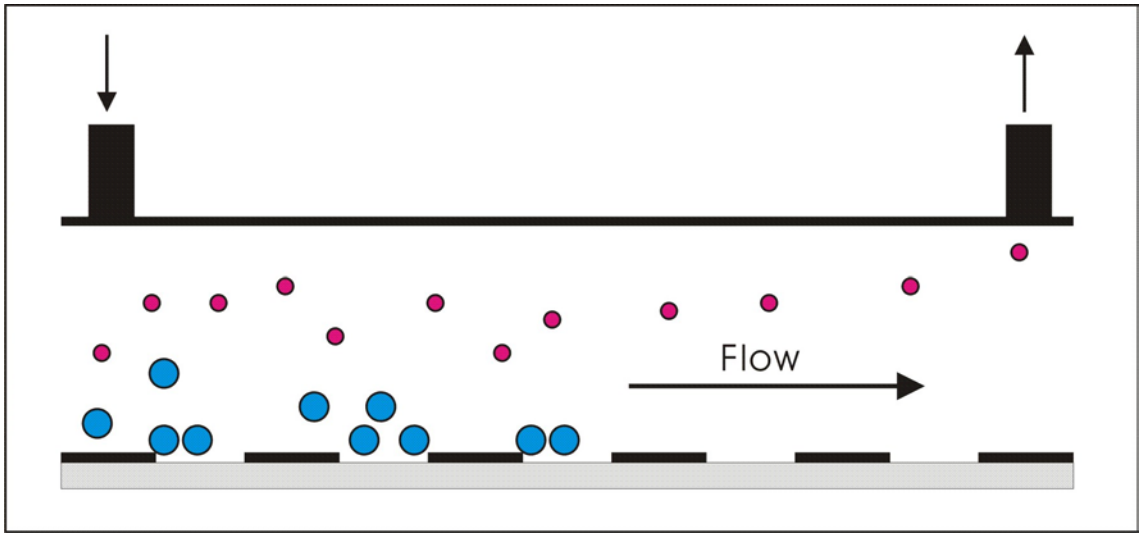

Figure 14: Schematic Diagram of a Flow- Through Cell Separation Device

There are many novel variations of the flow separation techniques. Figure 15 shows a two-chamber design [70]. The first part of the device uses negative DEP force to generate a random distribution of particles entering the device into a well-defined sheet. The second electrode array separates the particles using the classic flow separation by a combination of pDEP and nDEP. A more advanced version of the flow separation is called field-flow fractionation (FFF). This widely-used technique employs the effect of viscous force on the flow of liquid near a surface and applies a force field to place different types of particles at different heights above the surface. This results in the particles traveling at different speeds according to their distance from the surface. The use of uneven flow rate at different heights inside the channel to separate particles have been coined the term Hyperlayer DEP-FFF [71]. The velocity profile of an aqueous sample in a microchannel seen in Figure 16 a) is almost parabolic. It is defined by the following equation [72],

$$v_p(h) = 6v\frac{h}{H}(1-\frac{h}{H}) \qquad (23)$$

where h is the height above the chamber bottom, v is the mean fluid velocity, and H is the chamber height.

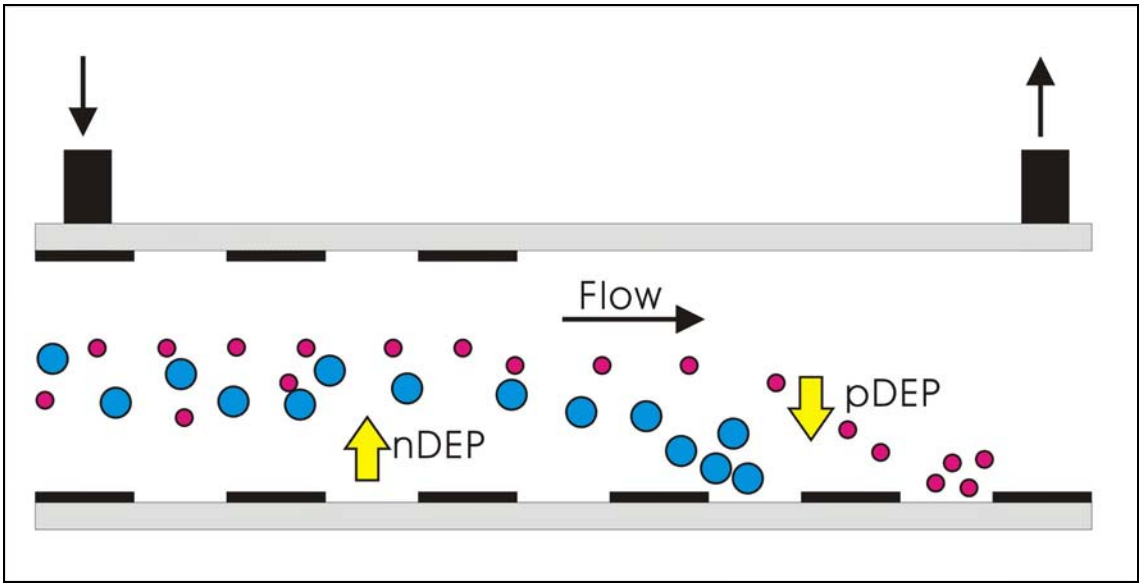

Figure 15: A schematic of two chamber flow through device

The field in FFF acts unconventionally; it does not directly drive separation. Instead, the field is applied at right angles to flow and serves to drive components into different laminae in a thin channel. The unequal velocities of the laminae then cause the separation, which unfolds along the flow axis [72]. The FFF mechanism is illustrated in Figure 16. Figure 16 a) shows the design of a typical FFF device and the force vectors on the target particles and the parabolic flow profile in the channel. In Figure 16 b) two particles are separated into two component bands in a thin ribbon-like channel. The flow of the fluid is much faster in the middle of the flow profile than the fluids that are beside the upper and lower chamber walls. A force field is perpendicular to the direction of the flow and it is influencing the position of the particles in the flow. The force field does not have to be dielectrophoretic. There are many variations and some of the typical fields include gravity (sedimentation FFF), temperature gradient (thermal FFF) and a crossflow (flow FFF). Overall, FFF devices have shown great promise for the fractionation of a number of particles including latex beads, bacteria and cancer cells.

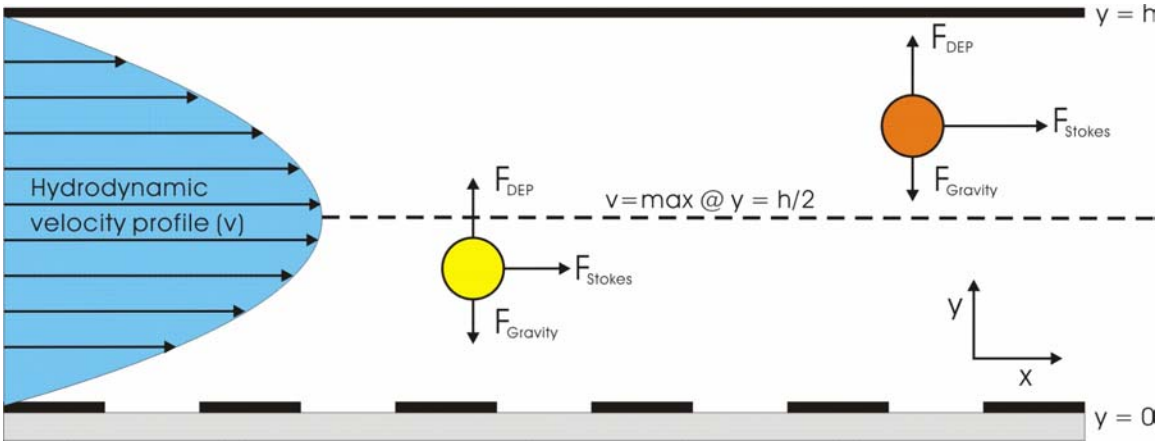

a)

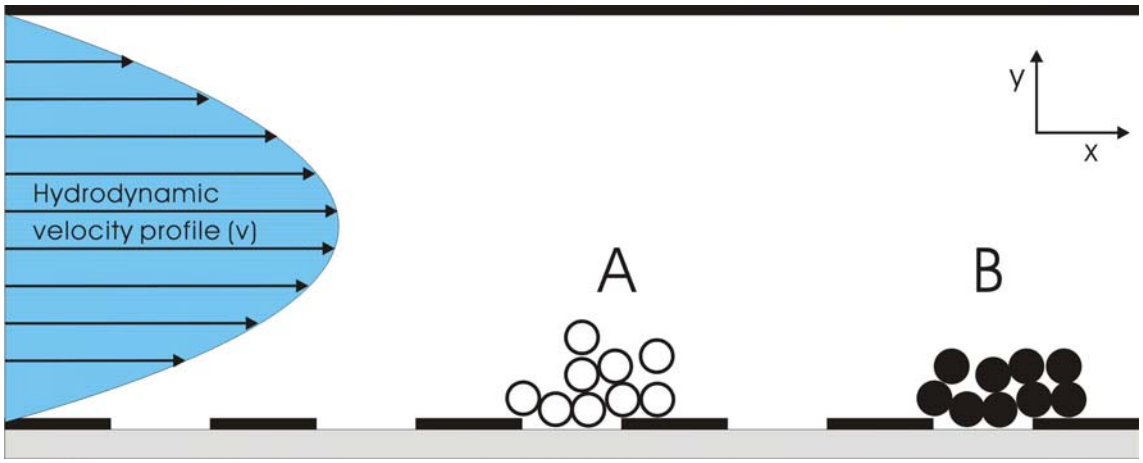

b)

Figure 16 a) Design of typical FFF device showing force vectors on particles, b) Flow profile and separation of particles

3.2.2 Traveling Wave Dielectrophoresis

Besides transporting particles in a conveyor belt like fashion, TWD has the ability to perform particle separation as well. Because of the physiochemical properties of dissimilar particles are different, one type of particles can be made to move in one direction while another type of particles in the opposite direction [73]. The goal for TWD separation is to achieve the transportation and the sorting of the biological sample in one elegant motion. Studies have shown that the multiple sets of TWD signals can be superimposed to achieve greater flexibility. In one experiment, two sets of waveforms running at different frequencies and amplitudes are simultaneous applied to the same electrode array. The two different types of particles over the electrode array, T cells and monocytes, respond to the mixed signals by moving in different directions [74]. In effect, different types of particles respond to their dominant signals running at the desired range of frequency and amplitude while ignoring the other signals. Signal superposition exploits this by running two or more signals at the same time, the particles naturally respond to their own signals and ignore the rest as noise. In addition, the transportation of particles by TWD method is one of the most common cell manipulation techniques and it is a promising alternative to particle transportation by fluidic pressure. The transportation of a cell-containing medium such as blood is hard to simulate. Clogging and uneven speed due to layer flow are some of problems encountered with active pumping in experiments. With TWD, the containing medium does not move and instead the particles within a still medium move along the electrode array in a microfluidic channel. TWD does not require an active pump and it can be miniaturized further for single cell applications. A fully integrated LOC device based on TWD transportation has been demonstrated by Medoro et al [75].

To achieve proper TWD effect, the layout of the electrodes is the most crucial factor. The geometry of the electrodes, the dimension, and the inter-electrode distances will all influence the TWD phenomenon. There are several design rules and limitations for TWD electrodes. First, the inter-electrode distances are kept at a minimum. The optimal distance is comparable to the diameter of the target particle. The major reason to have shorter distances

is to increase the electric field strength in between the electrodes. With increased electric field strength, the TWD translational force is also increased. Second, the deposition thickness of the electrode is kept at a minimum because thick electrodes often hamper the translational movements of the particles during TWD. Generally the electrode thickness is in the range of a fraction of a micron. Third, the range of materials used for the electrode is very limited. The ideal material for TWD must be highly conductive yet inert chemically. Gold is often used since it possesses both qualities but an adhesive material must go in between gold and the glass plate. Gold does not adhere to glass well and chromium is usually used as an interface substance to adhere gold onto glass. The need for an adhesion layer adds to the total thickness of the electrodes. Indium Tin Oxide (ITO) has been used in very specific applications that require good visibility since ITO is highly conductive yet transparent [76].

TWD evolved from early DEP experiments. Thus it is not surprising that the most popular design for the electrodes is the parallel track array. Usually the parallel tracks are laid in such ways that the particles are either placed directly above the tracks or in between two separate parallel tracks. Figure 10 a) shows the TWD design where particles are placed on top of the electrodes and Figure 10 b) shows the design where particles are placed in between electrodes. Both designs have proven to generate TWD translational force on the targeted particles. However, complexity is one major roadblock for performing TWD on the parallel track array. Normally, parallel track design is simplistic and straight-forward. However, since four different electric signals are used, unless each electrode in the array is individually controlled and bonded, any four sets of wires will have to make at least one cross. Several manufacturing strategies have been developed to cope with the crossing wires. The most common strategy is to utilize insulating semiconductor layers. In other words, the wires for the four electrodes are deposited in separate layers with insulating layers in between two conducting layers. Another design utilizes localized double layers to create a bridge for one wire to cross the wire underneath. Novel bonding techniques have also been developed for bonding individual electrode in the parallel track array. In one example, the contact pads for the electrodes are aligned following the Peripheral Component Interconnect (PCI) standard on a glass slide. The glass slide with the contact pads is then inserted mechanically into a PCI

slot inside the personal computer [77]. There is no doubt that the interface between electrodes and signal sources has become one of the most difficult steps in implementing TWD. Several options are available to minimize the number of required bonding pads. However, the more successful solutions often increase the complexity and the cost of the system at the same time. Despite the overhead, the parallel track design is still the most studied and the best understood structure for generating TWD phenomenon. To sum up, the major advantage of a TWD design is that it requires no fluidic pressure and thus it avoids the complicated fluidics. The disadvantage of TWD is that it requires four independent signals which add to the overall complexity and cost.

3.2.3 Deflector Design

Electrodes placed strategically near the intersections of microfluidic channels can be used to deflect target particles by negative or positive DEP forces [78, 79]. The type of DEP forces depends on the size of the particle as well as the frequency and voltage of the applied signals. Figure 17 shows a typical deflector electrode design. In this particular design by Durr et al [80], two types of particles are released from the inlet and a steady fluidic pressure by syringe pump maintains the flow rate at 5 – 500 μL/h. The deflector was activated with DEP signals and nDEP force deflects the smaller type of electrodes. The larger particles are unaffected by the nDEP since the electric field frequency is near the particle's cross-over frequency and DEP force is at the minimum. The larger particles thus pass the deflector electrode and into outlet 1.

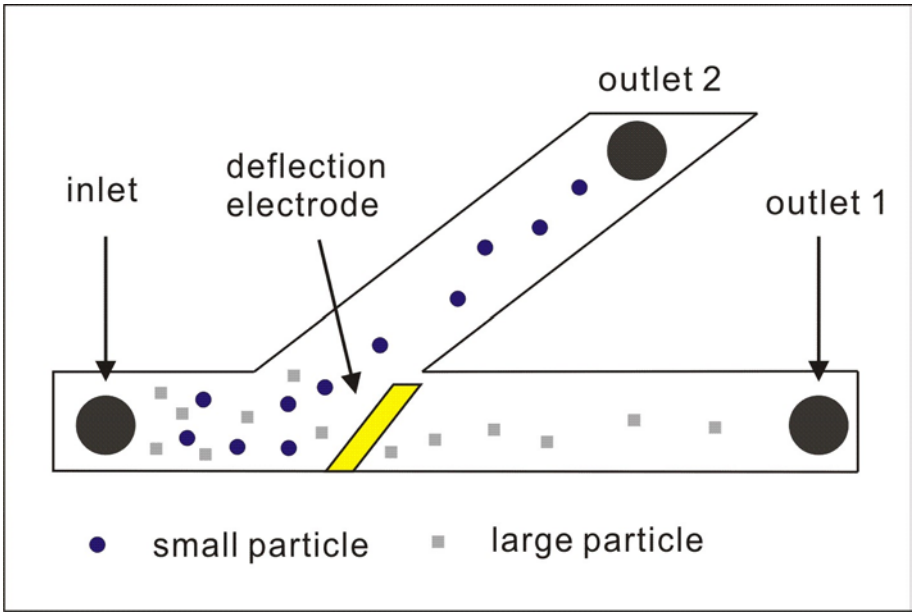

Figure 17: Typical deflector electrode design

A more novel way of deflector design is the use of insulating blocks inside a PDMS microchannel shown in Figure 18 [79]. The edge of the insulator block changes the path of electric fields and generates zones of high electric field strength and the target particles experience a repulsive force by nDEP at the corners of the block. The particles then deviate from their original path and are redirected into one of the two channels. The degree of deviation is dependent on the strength of the nDEP force. In this case, polystyrene beads of different sizes experience different strengths of electric fields. As seen in Equation (12), a larger particle experiences a stronger force than a smaller particle. In Figure 18, the discrepancy in size is evident. The larger particles, represented by squares, are deflected away from corners and into the upper stream. The smaller particles with their weaker deflections follow the downward stream. The uniqueness about this system is that the underlying electric fields are generated by direct current and further demonstrates that DEP can work with both alternating and direct current conditions.

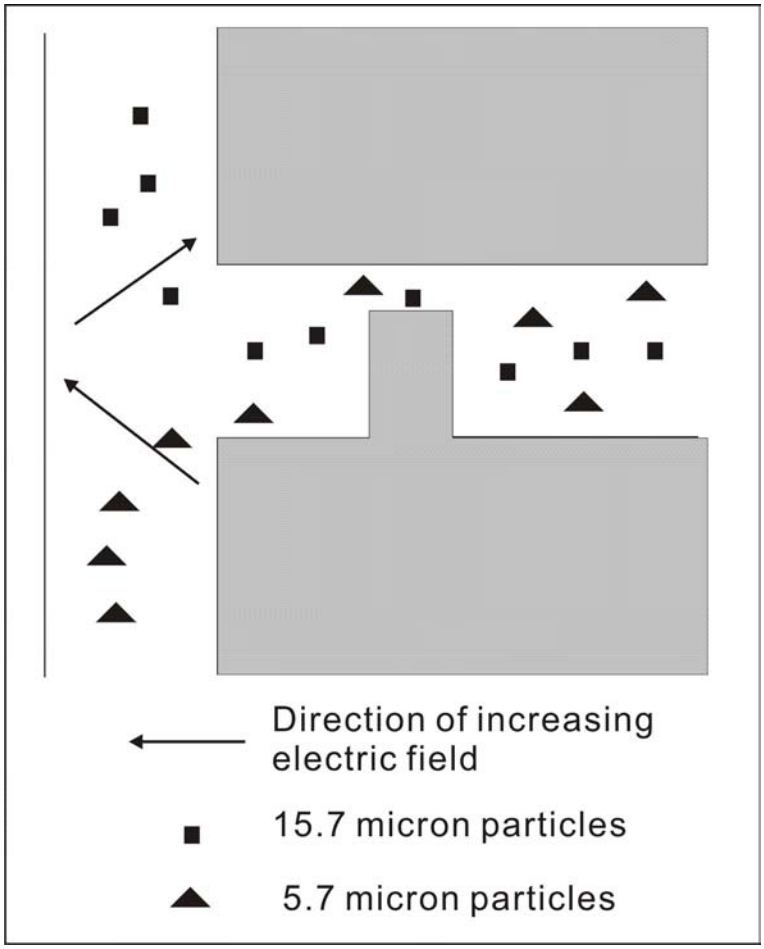

Figure 18 Typical deflector design using insulator blocks

3.2.4 Three-Dimensional Devices

Three-dimensional devices are another common DEP structure. In a design by Suehiro et al [81], a three-dimensional grid design is made possible by the application of ITO as the upper electrodes on gold-on-chrome lower electrodes shown in Figure 19 a). ITO has the unique characteristic of being transparent and conductive. The use of ITO as upper electrodes allows the visualization of particles underneath using an upright microscope. The two parallel arrays of upper and lower electrodes are placed perpendicular to each other to form a grid. This grid design allows the precise manipulation of a single biological cell by nDEP. Each electrode is individually controlled by a switch circuit and nDEP cages can be formed everywhere on the

grid to trap target cells. The movement of an nDEP cage from one grid intersection to another also transported the cells within the cage. This effect is exploited for transporting target cells to precise locations over the gird.

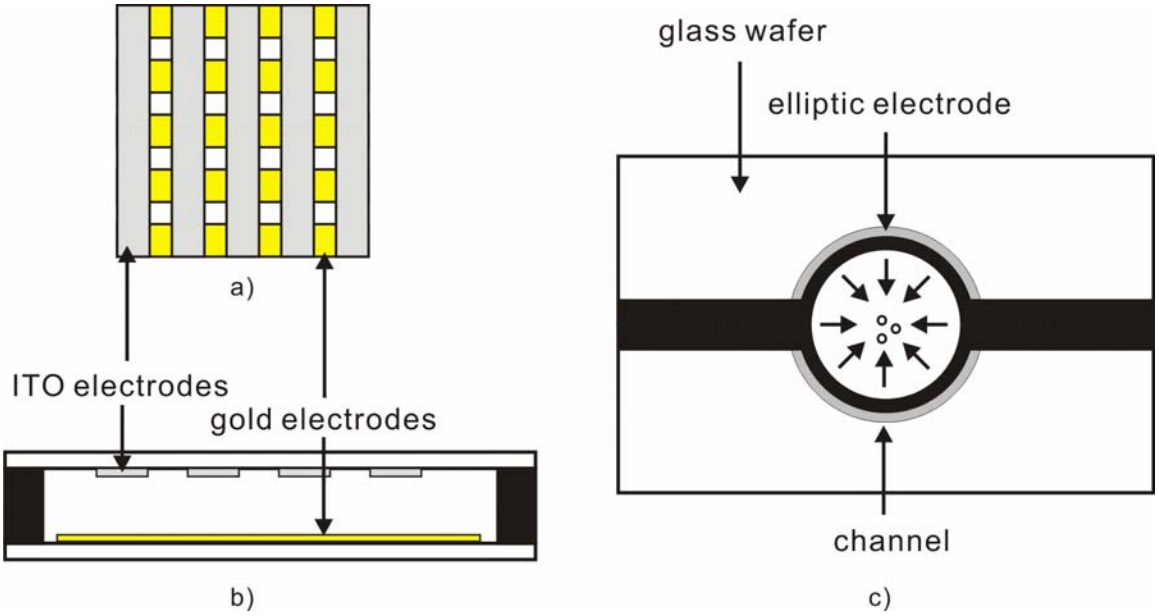

Figure 19 a) Top view of 3D grid electrodes, b) side view of 3D grid electrodes, c) side view of 3D elliptic electrode

Another three-dimensional design is the elliptic-like electrodes that surround the circular microchannel shown in Figure 19 c) [82]. The goal of the elliptic-like electrodes is to focus the target particles to the center of the microchannel and eliminate uneven flow rate of the transported particles. The implementation is to activate the elliptic-like channel with AC voltage waves of 15 $V_{peak\text{-}to\text{-}peak}$ at a frequency under 100 kHz. The alternating fields generate nDEP conditions and the resulting force lifts the particle into the center of channel. Uneven flow near the surface, or sheath flow, is unable to reach the particles near the middle and does not skew the optical sensing in flow cytometry applications. The novelty of this design is mostly in its fabrication. A glass wafer is first etched to produce a shallow trench. Chromium and then gold is deposited on the shallow trench and the electrode pattern is

produced with a lift-off process. The process is repeated to produce two identical halves of the channel. The two halves are then aligned and sealed together using high-strength epoxy. This two-step process of PDMS and metal-deposition is the fundamental building block of many three-dimensional designs and has proved popular for microfluidic applications as well.

Chapter 4
Current Cell Separation Design

4.1 Uniquely Shaped Electrode Design

The general template for the electrode design is shown in Figure 20. Most of the electrode designs are based on this template and it is designed with two goals in mind: portability and customizability. The template consists of 36 bonding pads. Each bonding pad can be individually controlled and the 36 electrodes can source 36 different wave patterns if necessary. The number of wires can be reduced for designs that do not need all 36 connections. The size of the entire microchip is fixed at 10 mm by 10 mm. The size is determined by fitting 4 microchips on one single wafer. The wafer is 25.4 mm by 25.4 mm (one inch by one inch) in dimension and 0.1 mm is left in between the four microchips for dicing.

The white block in the middle of the template is where the designs differ. The first design, the parallel track array, is shown in Figure 21. Because of its popularity in research literature, the parallel track array is used as a reference design. The experimental results performed on other novel electrode designs are compared to the experimental result on the reference design. The parallel track array is used to demonstrate some key phenomena including DEP trapping and TWD transportation. Each electrode is manufactured to be as thin as possible to generate the strongest electric fields. The electrodes are 20 μm wide and 1000 μm long.

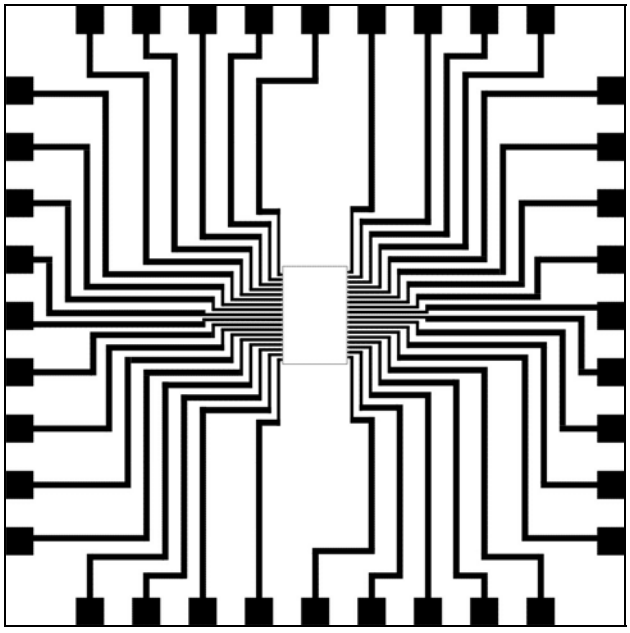

Figure 20 Template of DEP chip showing 36 bonding pads

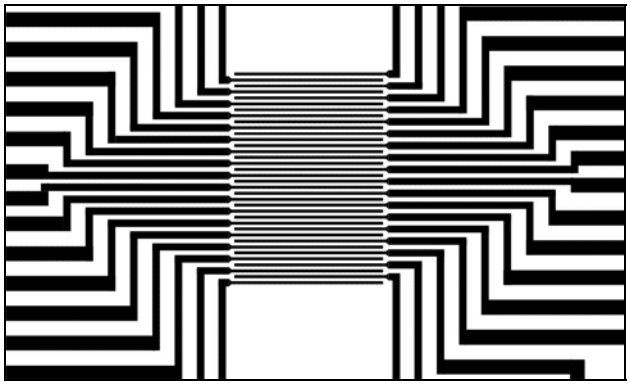

Figure 21 Parallel electrode array design

The triangular shaped electrodes shown in Figure 22 and Figure 23 are variations of the same design scheme. The concept is to create zones of varying electric field strengths. By varying the width to length ratio of the electrode, slightly different designs are produced. In Figure 22, the shorter electrodes are 500 μm in length and 20 μm to 40 μm in width. In Figure 23, the longer electrodes are 1000 μm in length and 20 μm to 40 μm in width. Both electrode designs are used in particle positioning applications as well as particle separations. The differences in results are recorded and compare to the simulation results to provide a better understanding of the impact of the electric field distribution on DEP.

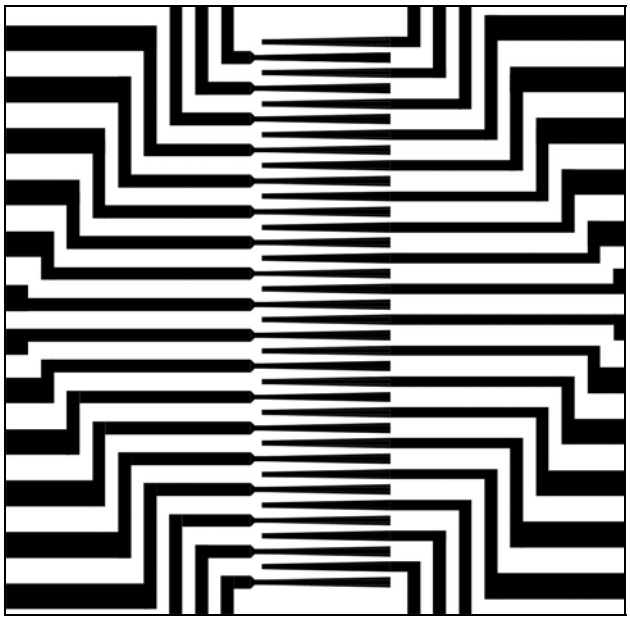

Figure 22 Wide triangular-shaped electrode array

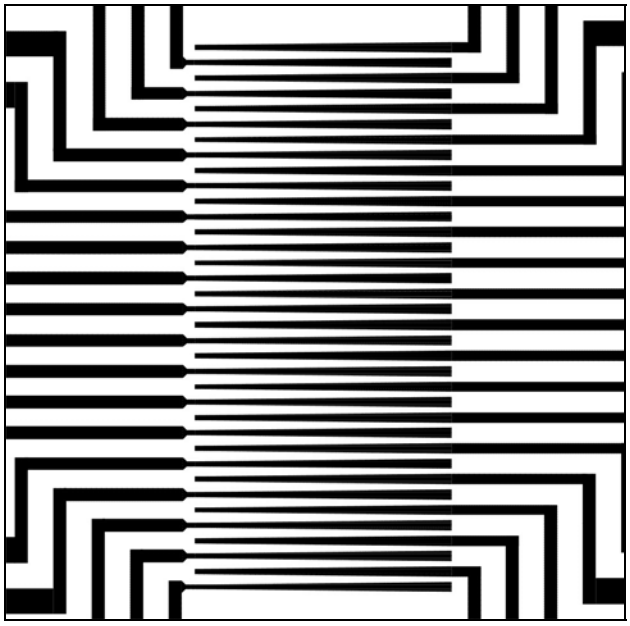

Figure 23 Narrow triangular-shaped electrode array

Figure 24 shows a "flip-flop" electrode array where two sets of electrodes in Figure 23 are arranged so that the successive electrodes flip flop in direction. The concept behind the design is to demonstrate a particle positioning device for microfluidic applications. The two sets of electrodes are called the upper and the lower electrodes based on their directions. The activation of the upper electrodes is followed by the activation of the lower electrodes and then the deactivation of the upper electrodes. The described procedure will create a shift in the density of electric fields which allows the target particles to shift and realign themselves on the electrodes. Because of the unique arrangement of the electrodes, new electronic circuits are needed to source the required 8 independent voltage signals. Section 5.4 illustrates in detail several cell manipulation techniques based on the flip flop design.

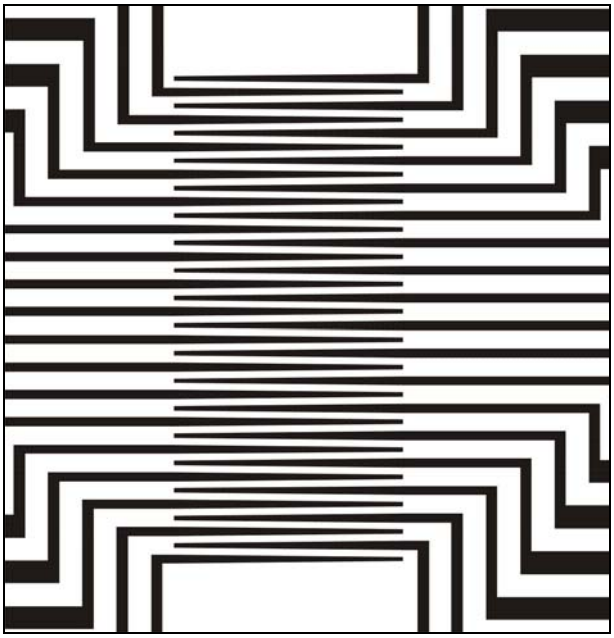

Figure 24 Flip-flop electrode array design

The lone exception to the template design shown in Figure 20 is the spiral design shown in Figure 25. The spirals are created specifically for gathering particles. The four spirals have different numbers of curves and various sizes of the gaps between the curves. The smallest gap in between the curves is 20 μm and the largest gap is measured at 50 μm. The gathered particles will be collected at the centers of the spirals. Each of the four spirals designs requires a specific holding well to contain the particle medium as well as four individual bonding connections. The four bonding connections are used to source TWD signals for the transportation of particles into the center of the spiral.

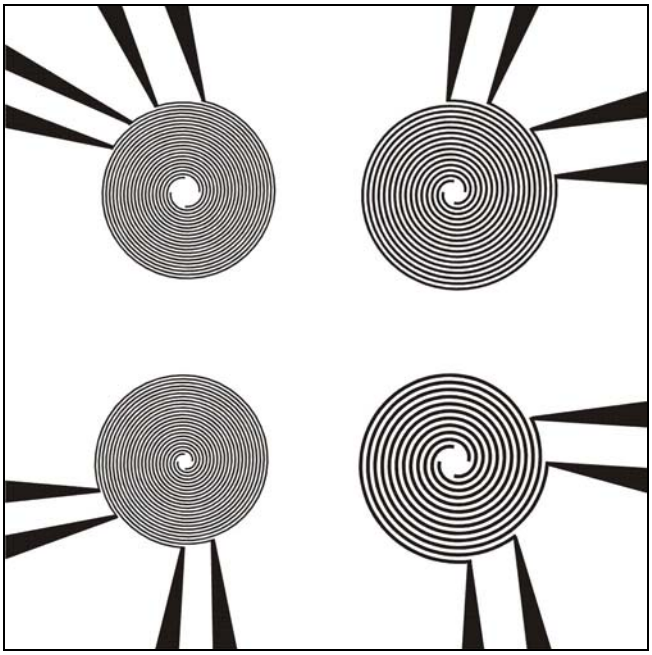

Figure 25 Spiral Electrodes with 20 µm and 50 µm gaps

The final mask file is shown in Figure 26. The file is created in LEDIT GDSII format and later converted into a CorelDraw 10 CDR file format. The CorelDraw file is made into a photo mylar film that is approximately 10 times the size of an actual glass wafer. The magnified electrode pattern on the mylar film is used as photomask to develop the photoresist in a microfabrication procedure shown in Section 4.2 of this report. Up to four different designs can fit in one glass wafer which greatly reduced the cost for each microchip. The square outline and the four short lines on the sides are not part of the electrodes. However, they are used to align the dicing machine for the dicing of the glass wafer into four microchips. Each of the short lines marks the starting point for dicing. The spacing between each design is 0.1 mm which leaves enough space for the dicing head and ensures the bonding pads are untouched. A summary of the five designs shown in this section is displayed in a logical manner in Table 6.

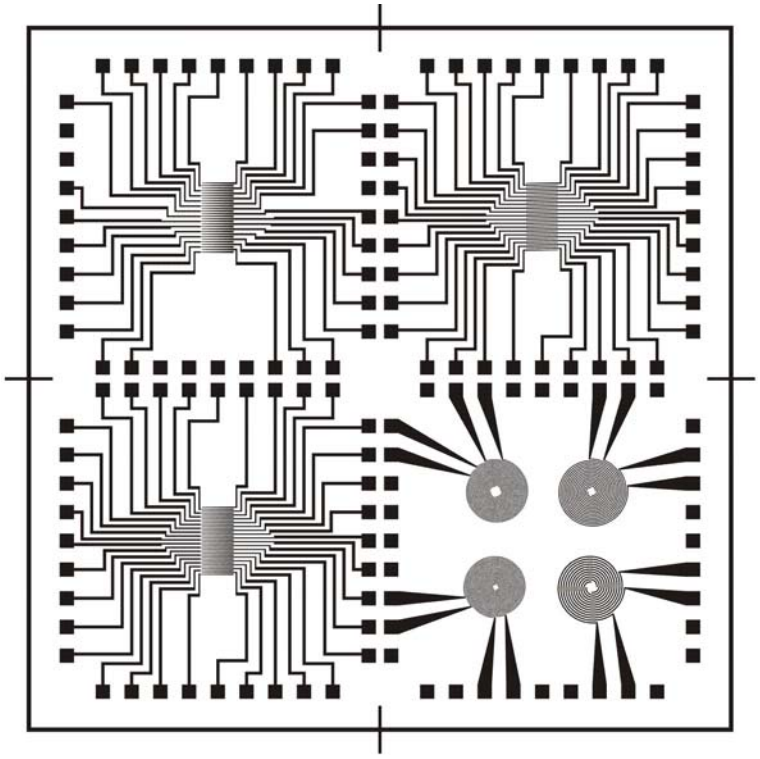

Figure 26 Final masks consisting of 4 separate designs

Table 6 Summary of different electrode designs

	Number of Electrodes	*Electrode length*	*Size of Gap between Electrodes*	*Functionality*	*Journal Reference(s)*
Parallel Electrode Array	36	1000 μm	20 μm	As a reference for DEP and TWD	[51, 70, 74]
Wide triangular-shaped electrode array	36	500 μm	40 μm (widest) to 20 μm (narrowest)	Cell positioning and separation	[83]
Narrow triangular-shaped electrode array	36	1000 μm	40 μm (widest) to 20 μm (narrowest)	Cell positioning and separation	[83]
Flip-flop electrode array	36	1000 μm	20 μm	Cell positioning	[83]
Spiral Electrodes	16	n/a (circular)	20 μm and 50 μm	Cell gathering	[45, 84-86]

4.2 Microfabrication

We fabricated our microchip using standard one layer metal process. After the glass wafer was RCA-cleaned to remove the organic coating and residue, 0.04 μm of chromium was deposited as an adhesion layer followed by 0.4 μm of gold applied using the E-beam evaporation technique. Subsequently, AZ3312 photoresist was spin-coated on top of the metal layer. Following standard photolithography procedure, the photoresist was exposed and developed, leaving the majority of the gold surface exposed. The exposed gold and the chromium layer underneath were then removed by two successive wet etching processes. The unexposed photoresist was stripped by acetone, leaving behind the patterned electrodes on the glass substrate. Figure 27 shows the step-by-step fabrication process.

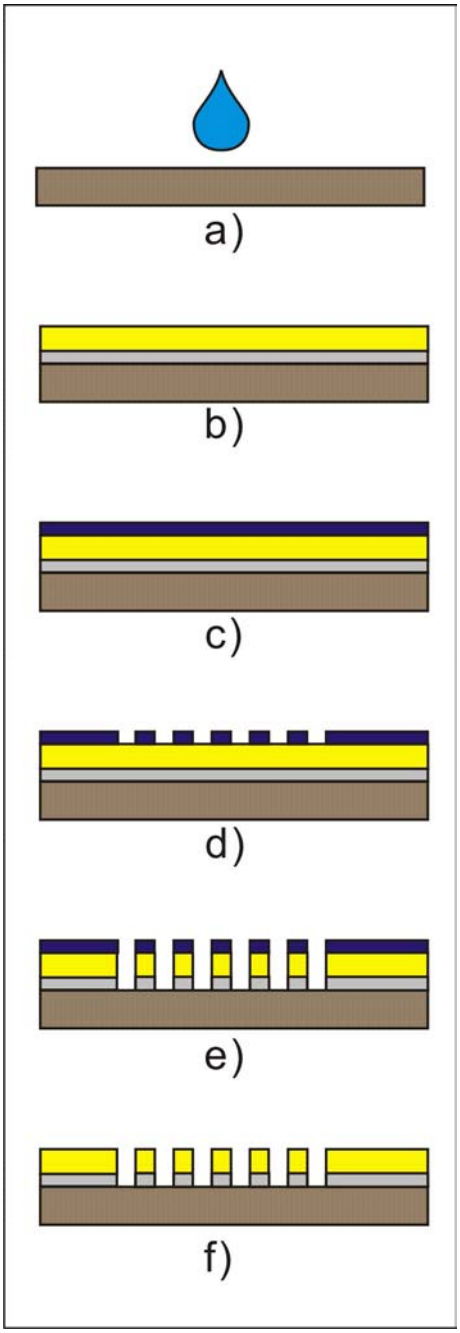

Figure 27 a) Wafer RCA-cleaned, b) deposition of chromium (grey) and gold (yellow), c) deposition of photoresist layer (dark blue), d) photoresist layer developed and etched, e) chromium and gold etched, f) removal of photoresist layer to expose gold electrodes

4.3 Device Packaging

Figure 28 presents the integration of the hardware used for packaging the microchip device. Each microchip was 10 mm by 10 mm in dimension and it consisted of 36 bonding pads, evenly distributed along the four edges for connecting the 36 electrodes. To house our microchip, we applied epoxy to the backside of its glass substrate and fixed the microchip to the die attach area of the 44-pin leadless chip carrier (Spectrum Semiconductor Materials, San Jose, CA). The 44-pin leadless chip carrier was selected because it had sufficiently large die attach area to house the microchip. Electrical connections were made by wire bonding the bonding pads on the microchip to the pads on the leadless chip carrier.

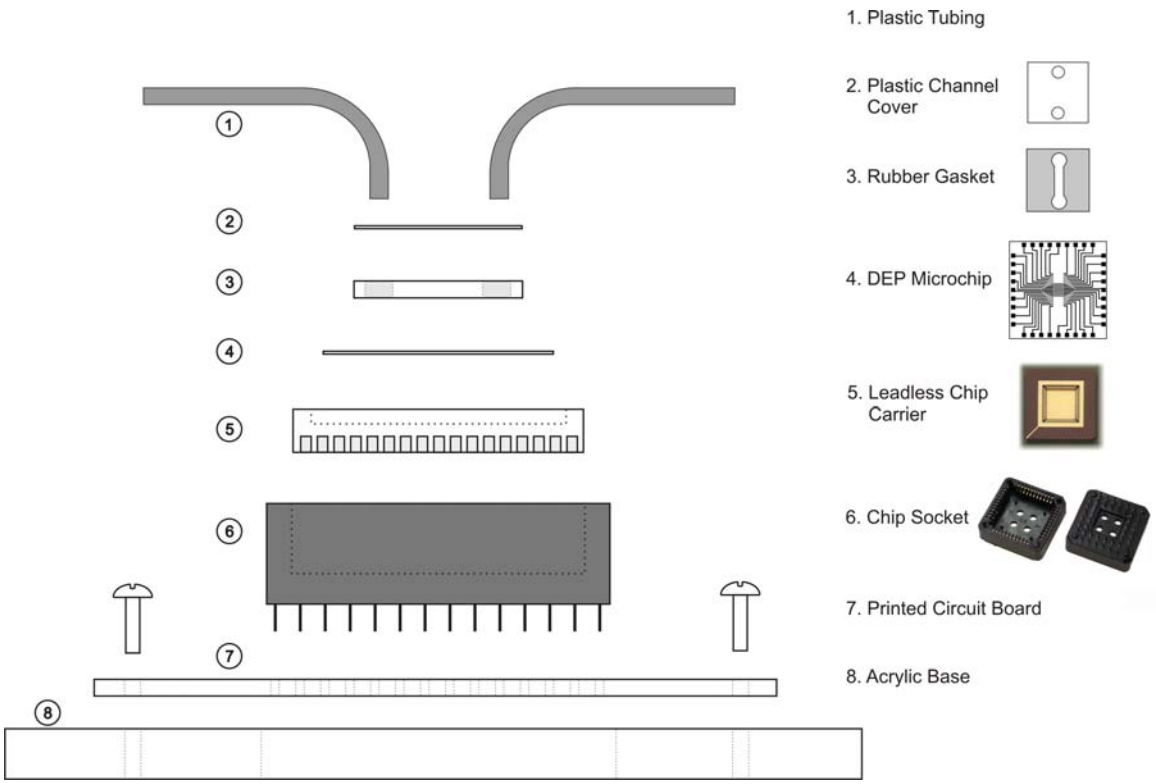

Figure 28 Schematic diagram of the DEP device showing the microchip and its packaging

The microfluidic channel was created by carefully affixing a custom-designed silicone rubber gasket to the microchip using a fast cure epoxy (Loctite Fixmaster, Rocky Hill, CT).

The silicone rubber gasket was a square slab, measured 7 mm by 7 mm in dimension and 250 μm in thickness, with a dumbbell-shaped cutout. The cutout was 1 mm in width and 3.75 mm in length and exposed the electrode array as the bottom of the microfluidic channel. Figure 29 shows the diagram of the silicone rubber gasket.

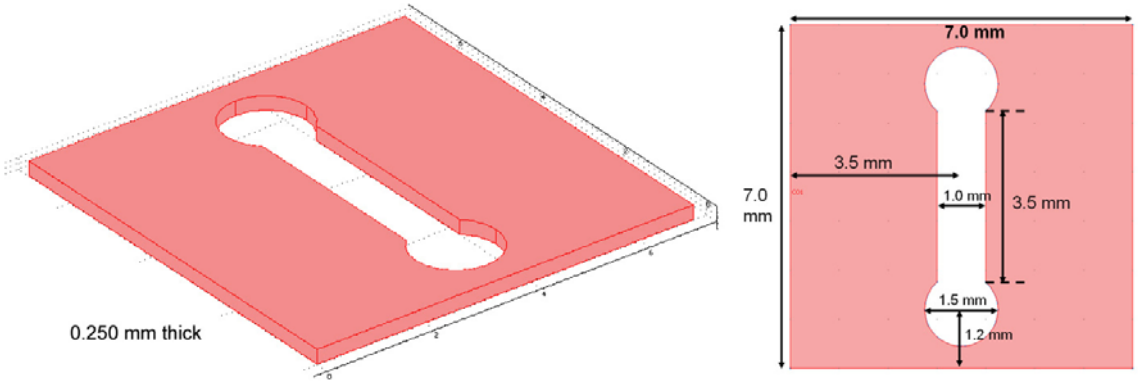

Figure 29 Diagram of silicone rubber gasket showing dimensions

The transparent cover on top of the channel was provided by a square piece of common transparency slide, razor-cut to exactly 6.5 mm by 6.5 mm in dimension. Before gluing the cover on the rubber gasket, two holes were drilled with standard 1/16-inch drilling bit to serve as the inlet and outlet port. Two 10-cm-long, 1/32-inch-inner-diameter plastic tubes (Tygon R-3603, Akron, OH) were connected to the inlet an outlet port for fluidic accesses to the channel. The tubes were first attached in place by an instant adhesive gel (Loctite Quicktite, Rocky Hill, CT) and then the interface was sealed with the epoxy. After the completion of the microfluidic channel, the microchip device shown in Figure 29 was inserted into a 44-pin plastic leadless carrier socket (Mill-Max, Oyster Bay, NY). The socket was then soldered onto a custom-made printed circuit board (PCB). To control stability for imaging, the PCB was mounted on a custom-machined acrylic base and the base was screwed tightly to the metallic stage of the microscope.

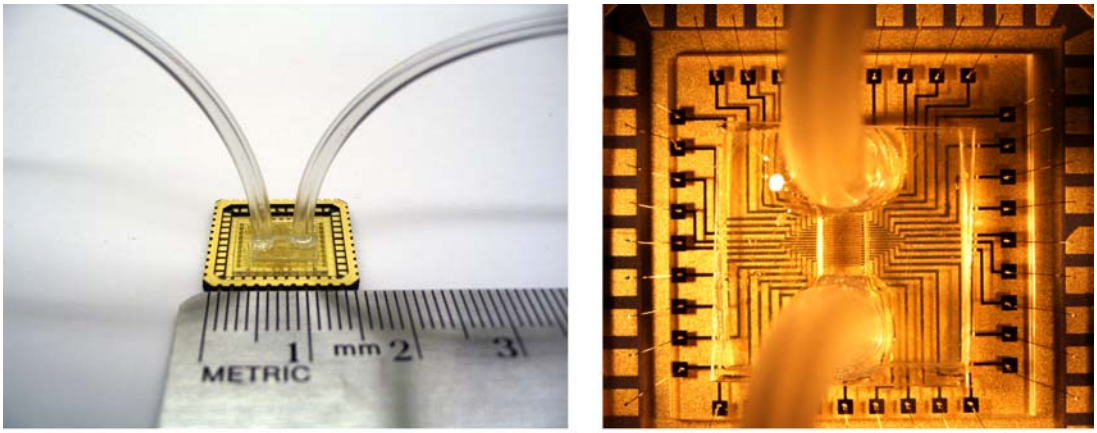

Figure 30 Photographs of the microchip after the completion of the microfluidic channel. (a) the microchip from the side with its dimension marked by a ruler, (b) a stereomicroscope photograph of the microfluidic channel and the electrode array underneath it

4.4 Electrical control

DEP waveforms were generated by a custom-built signal process circuit involving AD847J op-amps and ADG333 analog switches (Analog Devices, Norwood, MA). The circuit took the input reference waveform from a Tabor arbitrary waveform generator Model 3362 (Tabor Electronics, Yucaipa, CA) and processed it into dipole signals (0° and 180° out of phase) for DEP experiments and quad-pole signals (0°, 90°, 180°, and 270° out of phase) for TWD experiments. It was capable of producing 10 $V_{peak\text{-}to\text{-}peak}$ waveforms in frequencies from 10 kHz to 10 MHz. We used the ADG333 and a switch to select between the different sets of signals. Figure 31 shows the simplified block diagram of the circuit. Electrical connections between the waveform generator, the custom-built circuit, and the PCB were provided by coaxial cables with bayonet Neill-Concelman (BNC) connectors.

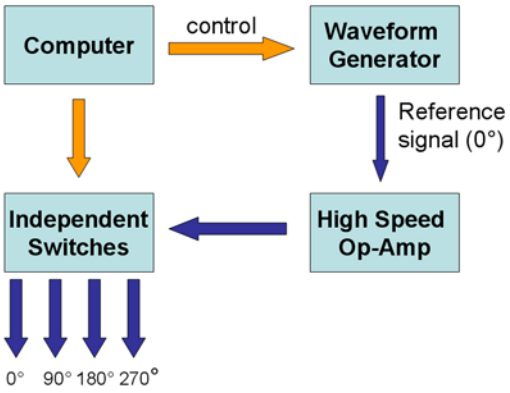

Figure 31 Block diagram of the electronic control for generating DEP and TWD signals

4.5 Fluidic Control

A peristaltic pump (Instech, Plymouth Meeting, PA) was the main mechanism of our active fluidic control. The peristaltic pump consisted of an inflow and an outflow connector. The outflow connector was connected directly to the inlet tube of the microchip device. The inflow connector was connected to a 10-cm tube with one end immersed in the microbead-containing medium. The waste from the outlet tube of the microchip device flowed into a vial and was collected after each experiment. Before injecting the actual microbead-containing solution, the entire microfluidic channel was flushed with 70% ethanol and then followed with a medium solution with the desired conductivity to establish a clean and controlled environment. Figure 32 shows the fluidic connections between the peristaltic pump and the microchip device.

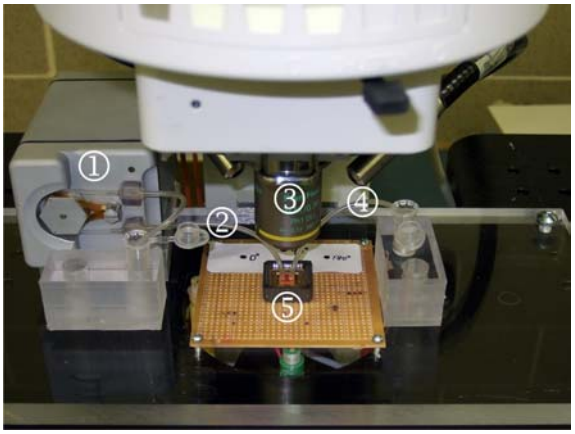

Figure 32 A photograph of the experimental setup showing (1) peristaltic pump, (2) inlet tube, (3) 10x objective lens, (4) outlet tube, and (5) the microchip device

4.6 Optics

A Nikon Eclipse E600FN microscope with a Plan Fluor Series 10x objective lens (Nikon Instrument, Melville, NY) was used for the visual observation of the experiments. A Fiber-Lite halogen fiber optic illuminator MI-150 (Dolan-Jenner Industries, Boxborough, MA) provided the light source for bright-field imaging. In addition, we performed dark-field fluorescent imaging with a Nikon D-FL EPI-Fluorescence attachment and a Nikon triple band excitation filter. We recorded all images and videos using a Nikon DigitalSight DS-5Mc camera. Figure 32 shows positions of the microscope and its lens in relation to the microchip device.

4.7 Bead Experiment

Commercially available Constellation polystyrene microbeads (Invitrogen, Carlsbad, CA) were used in the experiments. The microbeads are 5 μm, 10 μm, and 15 μm in diameters and compatible with our fluorescent excitation filter. The medium containing the microbeads was made with deionized water adjusted to 1 mS/cm with KCl. The solution was injected into the microfluidic channel via a peristaltic pump. Prior to injection, the electrodes were grounded

to avoid the activation of nDEP lifting force. After observing that a good amount of microbeads had been injected into the area of interest, the electrodes were activated with 6 $V_{peak\text{-}to\text{-}peak}$ sinusoidal waves. The conductivity of the microbeads was much less than the conductivity of the medium and nDEP was observed in all experiments.

4.8 Cells Experiments

4.8.1 HeLa

HeLa cell is one of the three types of cells used in the DEP experiments. HeLa cell line is derived from cervical cancer cells from Henrietta Lacks [87]. One HeLa cell line is maintained at the Department of Chemistry at the University of Waterloo by Dr. Shirley Tang's research team. HeLa cells are chosen because their availability and their visibility under the microscope. A fully grown HeLa cell is about 20 μm in diameter. Even without dyes, HeLa cells are easy to spot under 100X magnificent under our microscope. In addition, the cell line is passaged every week for research purposes. HeLa cells are grown in the DMEM media (containing 10% fetal calf serum, penicillin streptomycin, 2mM L-glutamine, and 1mM sodium pyruvate). The subculture of HeLa cells is fluorescently tagged for better imaging.

HeLa cells are treated with CFDA SE Tracer kit (Invitorgen, Carlsbad, CA). The kit contains a cell-tracing reagent CFDA SE (carboxy-fluorescein diacetate, succinimidyl ester). CFDA SE works by first passively diffusing into HeLa cells. CFDA SE then is digested by HeLa cells to produce a highly fluorescent ester group which binds with intracellular amines [88]. The resultant, a dye-protein product, is retained by HeLa cells throughout development, meiosis, and in vivo tracing [89]. To label HeLa cells in suspension, the solution containing HeLa cells is first centrifuge to obtain a cell pellet. The cells are then resuspended in 37°C phosphate-buffered saline (PBS) buffer containing CFDA SE. HeLa cells are then incubated at 37°C to allow diffusion. After 15 minutes in the incubator, PBS buffer is replaced with regular cell medium and the culture is again placed in the incubator for another 30 minutes at 37°C. The fluorescently tagged HeLa cells are then centrifuged and washed with ultra-pure

distilled water. The dyed HeLa cells are then micropipetted into KCl medium with the predetermined conductivity. About 50 μL of HeLa cells in water is placed in 1.0 mL of KCl solution. A sample is smeared on a microscope slide and checked for the proper concentration. Ideally, we like to see 20 – 30 cells in a 1 mm by 1 mm square under 100X magnification. HeLa cells labeled with CFDA SE can be seen under the Nikon DPI-fluorescent microscope with FICT (fluorescein isothiocyanate) filter attachment. FICT filter has an excitation filter range of 475-490 nm and emission range of 505-535 nm which matches the excitation and emission peaks of CFDA SE tracer kit which are 492 and 517 nm, respectively.

4.8.2 Yeast

Pichia pastoris is a species of methylotrophic yeast. It is widely used for protein expression using recombinant DNA techniques. A *Pichia* cell line is maintained at the Department of Chemistry Engineering at the University of Waterloo by Dr. Perry Chou's research team. *Pichia pastoris* differs from the more commonly used *Saccharomyces cerevisiae* (common baker's yeast) in that *Pichia* is a methylotroph and can grow with simple alcohol as its only source of energy. In addition, *Pichia* is well studied and is considered as a model organism for biology [90]. The advantages of using *Pichia* are that it is readily available and it remains viable under harsh conditions with minimum supervision. However, the experiments involving *Pichia* are hindered by its small size. Each *Pichia* cell is roughly 5 – 7 μm in diameter which makes it really hard to image using the current optical microscope. Because of its small size, *Pichia* usually behaves very differently from the larger mammalian cells as well as the microbeads. It experiences the attracting pDEP forces where other, larger particles experience the repelling nDEP forces. In addition, it moves in a faster speed under TWD than larger particles do. These differences make *Pichia* a prime particle for separation studies. *Pichia* in our experiment is grown in a nutrient-rich medium such as Yeast extract Peptone Dextrose (YPD) for three days. It is then centrifuged and washed with ultra pure distilled water for two times. 75 μL of resuspended *Pichia* is then micropipetted into 1 mL of

KCl solutions with fixed conductivities. In separation experiments, 50 μL of microbeads are added to the medium as a reference for the faster moving *Pichia*.

4.8.3 Hematopoietic stem cell

Hematopoietic stem cells or blood precursor cells are the third type of cells used in the DEP experiments. It is maintained by Dr. Eric Jervis's research team in the Department of Chemistry Engineering at the University of Waterloo. Hematopoietic stem cells are the early precursor cells that give rise to all the blood cell types [91]. Hematopoietic stem cells are obtained from the bone marrows of animals. The mentioned cell line is obtained from rodents. In appearance, they are rounded and slightly smaller than HeLa cells in size. A microscope picture of Hematopoietic stem cells under 200X magnification is shown in Figure 33. Hematopoietic stem cells are used because of their availability and their similarity to human blood cells which are the ultimate target cells for our device. Hematopoietic stem cells are grown in conditions similar to HeLa cells. They are maintained in an incubator that is temperature controlled to 37°C with injection of CO_2 gas to maintain the pH of the cell medium.

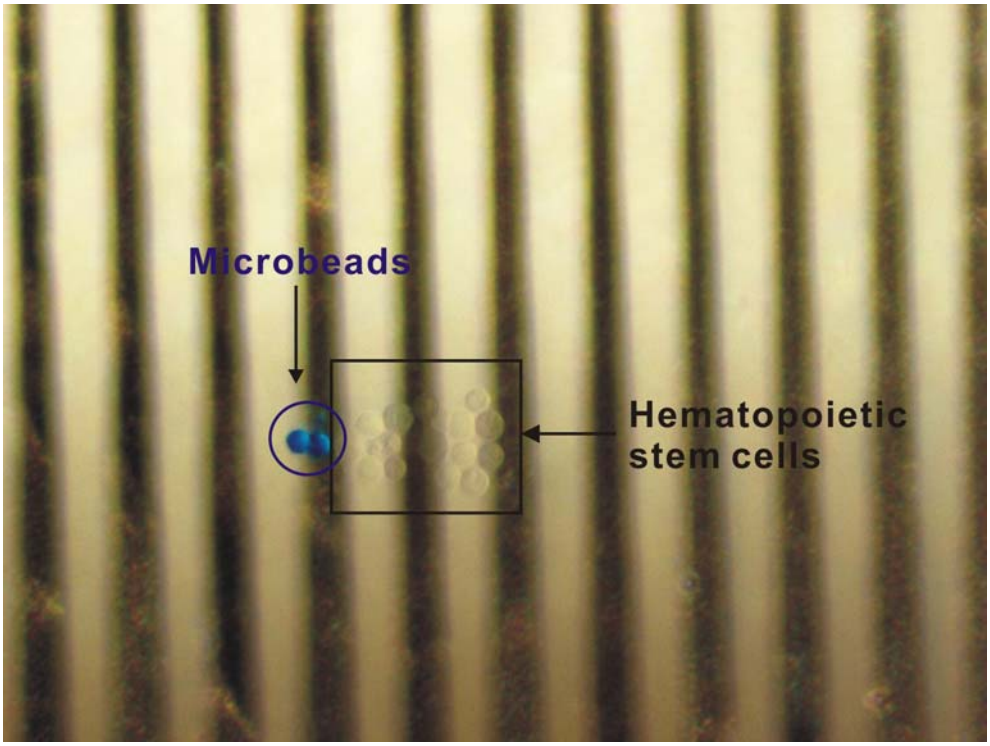

Figure 33 Blue microbeads next to a group of 15 Hematopoietic stem cells

Chapter 5
Experimental Results

5.1 Enhancing Dielectrophoresis Effects with Novel Electrode Geometry

The design process started with MEMS Pro v5.0 (SoftMEMS, Los Gatos, CA) where several variations of the triangular-shaped electrodes were created. Figure 35 shows the configuration of a triangular-shaped electrode array. The orientation convention is defined by a Cartesian coordinate system where the vertical (*y*-) axis is parallel to the electrodes and the horizontal (*x*-) axis is perpendicular to the electrodes. Each electrode design was characterized by its height (*h*), top electrode width (*t*), bottom electrode width (*b*), and gap size (*g*).

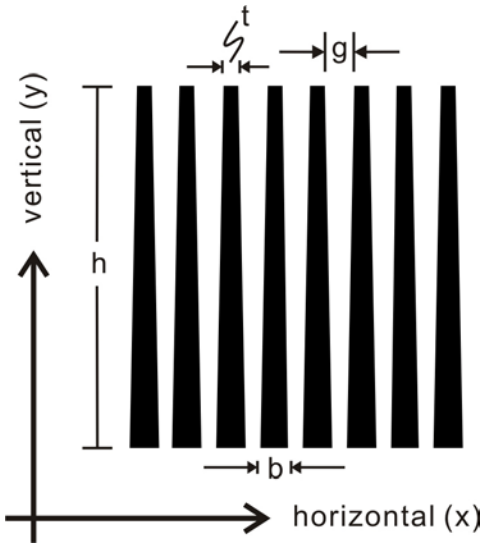

Figure 34 Configuration of the triangular-shaped electrode array

We simulated the electric field strength generated by each design in Comsol Multiphysics. Figure 35 (a) shows the result of our final electrode design under DEP conditions where the electrodes alternated in voltages of +5 V and -5 V. For reference, the surface electric field

plot of a parallel track electrode array with the same applied voltages is shown in Figure 35 (b). With the two simulation plots side-by-side, it is clear that the electric field strengths between the triangular-shaped electrodes increased from top to bottom while the electric field strengths remained constant between the rectangular electrodes of the parallel track array. For the triangular-shaped electrode array, the rate at which the electric field strength increased depended on the geometry of its electrodes – more specifically, the bottom electrode width to the top electrode width ratio (*b/t*). A larger *b/t* value resulted in a faster rate of increase in electric field strength and the field remained constant if *b/t* ratio equaled to 1. During the design process, the goal was to achieve the most varied electric field strengths with the thinnest electrodes possible within our manufacturing capabilities. Essentially, the *b/t* ratio was desired to be as large as possible while *b* and *t* to be as small as possible. In the end, the best result was obtained from an electrode design that had height of 1000 μm, base width of 40 μm, top width of 20 μm, and top gap size of 40 μm. From the simulation plot in Figure 35 (a), the maximum electric field strength between the electrodes was approximately twice the minimum. Figure 35 (a) also shows that the triangular-shaped electrode array can generate bands of different electric field strengths across the electrodes. In the 2D model, any two points on a line drawn between the gaps of the electrodes will have identical field strength. The points immediately above and below the line will experience comparable electric field strengths. Further from the line, the differences in the magnitudes of the electric fields increased. Since similar electric fields were closer than distinct ones, the triangular-shaped electrodes had essentially created horizontal bands of distinct electric fields. These bands of electric field were crucial in creating the "banding effect" where the microbeads aggregate in a straight horizontal line across the electrodes.

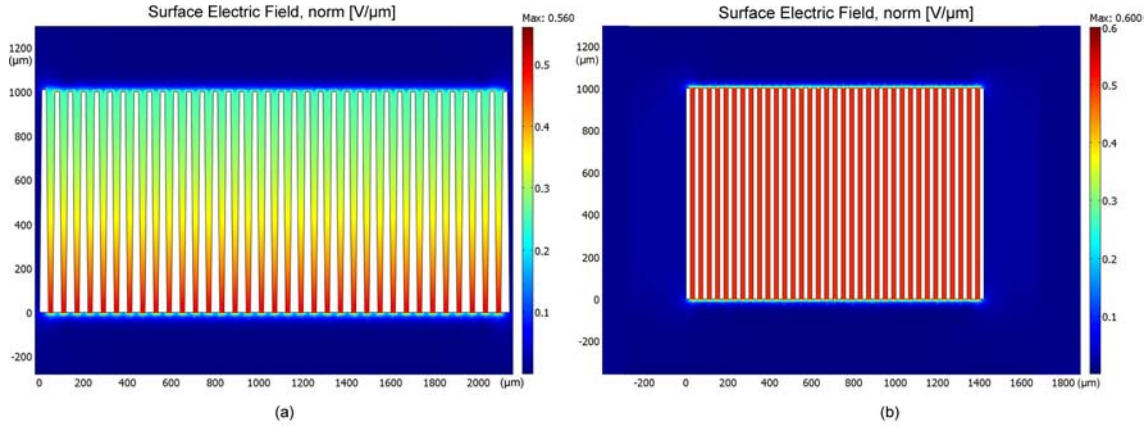

Figure 35 Surface diagrams of electric field of (a) triangular-shaped electrodes, (b) parallel track electrodes

Figure 36 (a) – (d) shows the banding of microbeads in progress. The banding effect was activated with regular DEP waveforms (0° and 180°). During banding, the microbeads first experienced nDEP force and were lifted over the electrodes. Depending on their initial positions, the microbeads then moved up or down vertically along the electrodes to align themselves in a straight horizontal line. During the vertical movements, the horizontal (x) positions of the suspended microbeads did not change. The same experiment was performed on the parallel track electrode array shown in Figure 35 (b). The microbeads on the array also experienced nDEP force and were suspended over the electrodes. However, the microbeads remained stationery over the gaps of electrodes and did not exhibit any banding effect.

The experiments were repeated with various frequencies and the banding effects occurred when microbeads experienced an nDEP force. The band of microbeads exhibited some interesting properties. The microbeads organized themselves into a horizontal line at a predictable position. The positions of the microbeads, measured from the bottom of the electrodes, were sensitive to the frequencies of the waveforms. In all experiments, the banding effect occurred at a range of positions from 330 μm to 400 μm. Figure 37 shows the relative positions of the microbead bands in a 1 mS/cm KCl medium for the DEP waveforms with frequencies from 10 kHz to 5 MHz. To confirm our findings, we performed the experiment with 10 kHz waveforms and observed the microbeads line up at 347 μm. The

waveforms were then turned off and turned on again at 1 MHz. The shifting of microbeads was immediately visible. The microbeads reorganized themselves in a band at 381 μm, 34 μm above its previous position.

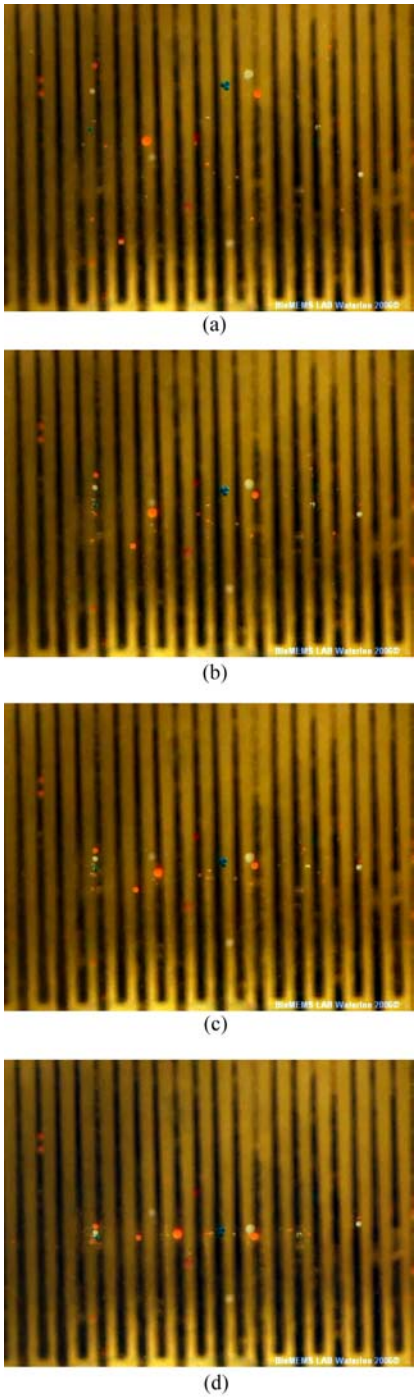

Figure 36 Photographs of banding effect in a 1 mS/cm under 100 kHz DEP waveforms. (a) the positions of microbeads right after the activation of DEP signals, (b) the position of the microbeads after 43 seconds, (c) the position of the microbeads after 75 seconds, (d) the position of microbeads at 125 seconds

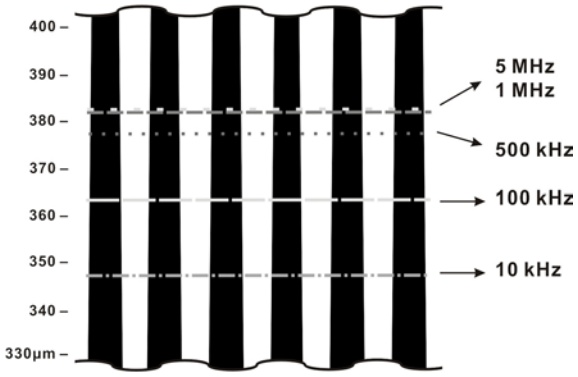

Figure 37 Vertical positions of the microbead bands with respective frequencies of the applied waveforms

In addition, it was possible to move the entire band of microbeads in the horizontal (*x*-) direction by applying the appropriate TWD waveforms. The applied TWD waveforms were identical to the DEP waveforms that generated banding effects except the four sinusoidal waves were out of phase by 90° from one another (0°, 90°, 180°, and 270°). The TWD signals instantly drew the particles to the right or the left depending on the direction of the traveling waves. When the DEP signals were applied first, the vertical position of the band was unchanged during the horizontal movement. The band of microbeads eventually gathered at the end of the electrode array. Figure 38 shows the line of microbeads moved to the left when TWD signals were applied.

The triangular-shape electrode array possesses three potential advantages over the parallel track array design. First, the final vertical location of the particles on a triangular-shaped electrode array was known before experiments. Given data on the waveforms and the medium, we can predict with accuracy the final vertical position of the particles. This differs from the regular parallel track electrode array where the particles remain at their initial vertical positions and their final positions are impossible to predict if the initial vertical positions are not known beforehand. Therefore, our triangular-shaped electrode array has the advantage over the parallel track electrode array in applications that demand precise control of the particles' final positions such as cellular imaging. Secondly, the banding effect makes

moving the target particles into a microfluidic channel easier. Since the banding effect by DEP congregates the particles into a thin line on the electrodes, the line of particles can be easily transported into a microfluidic channel with fluidic pressure. This allows us to move particles into narrowing channels with high efficiency in an organized fashion. For a system designed without flowing fluids, TWD effect can be used to move the cells across the electrodes without breaking formation as demonstrated in Figure 38. To move the line of microbeads into a smaller channel, it is a simple task of extending the underlying electrodes. In addition, DEP signals can be easily switched to TWD signals by adjusting the phase differences between the sinusoidal waves without incurring additional complications. Thirdly, we suspect that if the two particles' physiochemical properties are sufficiently different, they might seek out and occupy regions with two different electric field strengths. This is shown in Figure 39 where the larger red-fluorescent microbeads and the smaller green-fluorescent particles occupied distinct lanes. There are two important advantages for organizing particles into lanes. First, the collection and separation of the particles are done in one single step and only one set of DEP waveforms is required. Secondly, since each lane is very thin, as long as two types of particles do not occupy the same position, there is enough room on the electrodes for several lanes. Multiple lanes allow the simultaneous processing of two or more types of particles which greatly increases the throughput over conventional separation methods. Figure 40 shows a conceptual drawing of processing particles in multiple lanes.

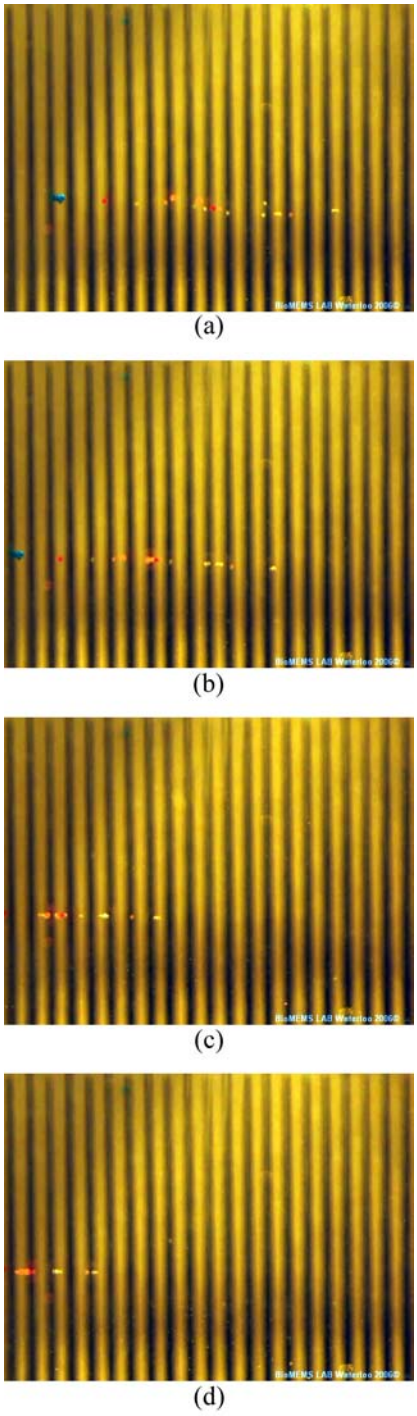

Figure 38 Photographs of TWD effect on microbead band. From (a) to (d) the microbead band moved to the left without breaking formation. Its vertical position was maintained throughout.

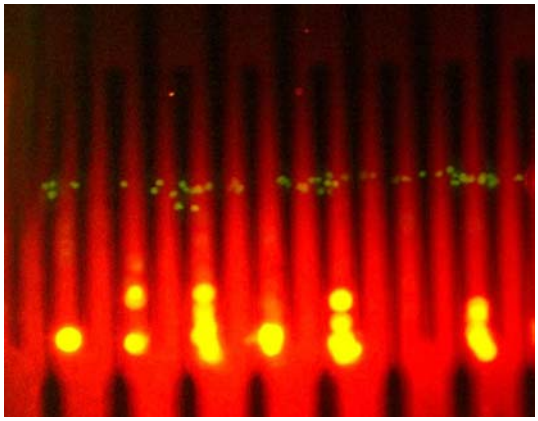

Figure 39 Separation of two particles into distinct lanes

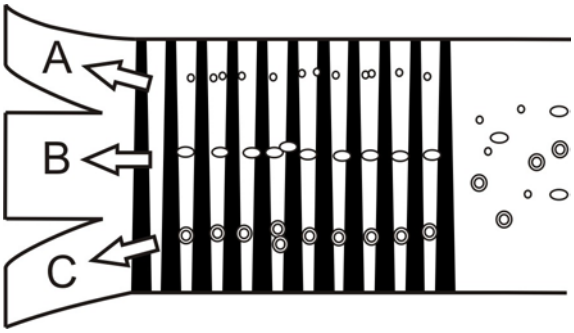

Figure 40 Conceptual drawing of the separation of 3 different types of particles into lane A, B, and C

5.2 Cell Collection, Separation and Transportation

The DEP microchip device's ability to collect and then trap biological cells was demonstrated with the activation of nDEP. The concentration of the fluorescently tagged HeLa cells is shown in four frames from Figure 41 (a) to (d). Initially, the HeLa cells in the field of view were randomly distributed as shown in Figure 41 (a). After activating the electrodes, nDEP forces lifted up the HeLa cells and moved them into the middle of the channel where the electric field strength was at minimum. The cells remained trapped at the middle of the channel for further operations. The transportation of the trapped HeLa cells was performed

with the activation of the TWD signals and can be seen in Figure 41 (e) – (h). The cells moved across the electrodes in the direction of the TWD signals and stopped at the end of the electrode track shown in Figure 41 (h). In this experiment, the distance that the cells traveled under TWD was only limited by the length of the electrode array. Thus the use of TWD on the parallel electrode array can serve as a "conveyor belt" to move cells from one reaction chamber to another.

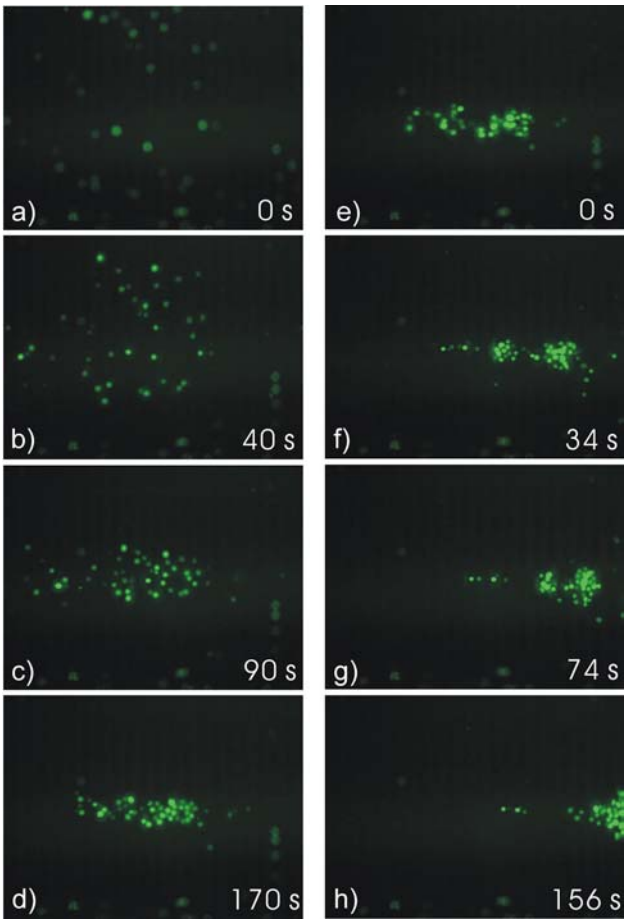

Figure 41 (a) – (d) Concentration of HeLa cells in the middle of channel, (e) – (h) Transportation of cells to end of channel

In addition to its ability to transport cells, TWD can also be used to separate different particles. Figure 42 (a) – (d) shows the simultaneous transportation and separation of

microbeads and yeast cells. In this experiment, a mixture of microbeads and yeast cells was pumped into the DEP microchip device. TWD was then activated and both type of particles started to move across the electrodes. The separation was based on the difference in traveling speed of the particles over the electrodes. Yeast cells were shown in the experiment to travel faster than the microbeads. The variation in speed is due to the physiochemical differences of the two particles [79]. In Figure 41 and Figure 42, we have demonstrated the collection, transportation, and separation of three types of particles based on purely electrical means. The advantages of using a DEP-based cell sorting system, when compared to a fluidic-driven device, include the reduction of simulation complexity, its easiness in manufacturing, and its versatility in functions. A plan for an integrated blood analyzer system based on DEP is discussed in great detail in Chapter 6 of this report.

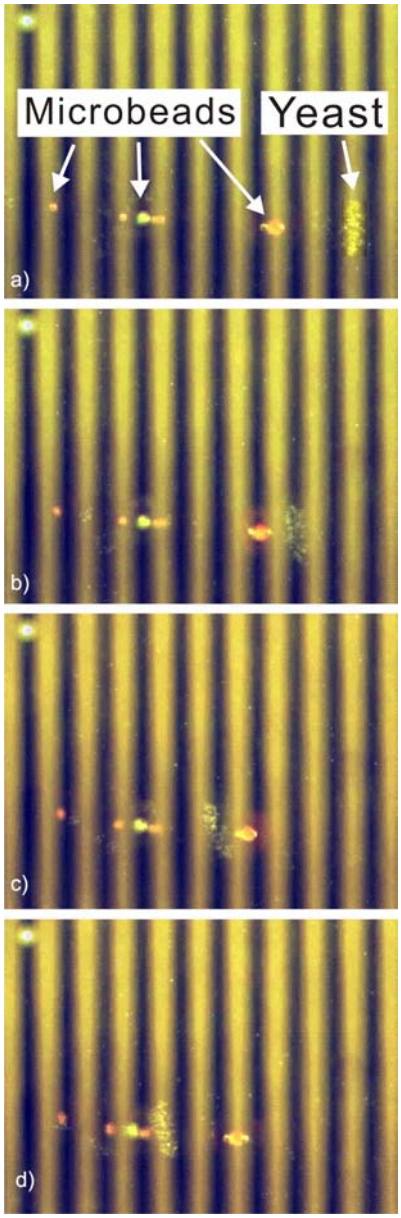

Figure 42 (a) – (d) Simultaneous transportation and separation of microbeads and yeast

5.3 Flip-flop Electrodes and 4-Directional Movement

The third set of experiment takes place on the flip-flop electrodes shown in Figure 24. The flip-flop electrodes are so named because the successive electrodes flip-flop in direction. The electrodes are divided into an upper electrode component and a lower electrode component. In Figure 43, the upper electrodes are composed of upside down triangular-shaped electrodes marked by the colors red, orange, yellow, and green. The lower electrodes are represented by the colors blue, violet, black, and white. The color codes and their corresponding electrodes are listed in Table 7. For convenience, a code consisted of one letter (U or L) and one number (1 to 4) will symbolize one of the eight electrodes in Figure 43 which pattern is repeated for the length electrode array. Each of the flip-flop electrodes has a single top width (t) of 20 μm, a bottom width (b) of 40 μm, and an inter-electrode distance (d) of 120 μm. The Cartesian coordinate system is defined as shown in Figure 43 with x as the horizontal axis and y as the vertical axis. Since independent DEP and TWD experiments are to be performed on both electrode components, the upper and the lower electrodes each require 4 independent signals for a total of 8 independent signals. The new circuits shown in Figure 44 are custom designed for the flip-flop electrodes. It can source up to 8 independent signals with 4 different phases. Two single-pole-double-throw (SPDT) switches allow the upper and lower electrodes to be turned on and off independently. A third SPDT switch allows the switching between DEP and TWD signals and provides the proper signals to the two on-off switches. With the customized circuit, independent DEP and TWD signals can be sourced to either the upper electrodes or the lower electrodes which crucial in controlling the position of the target particles.

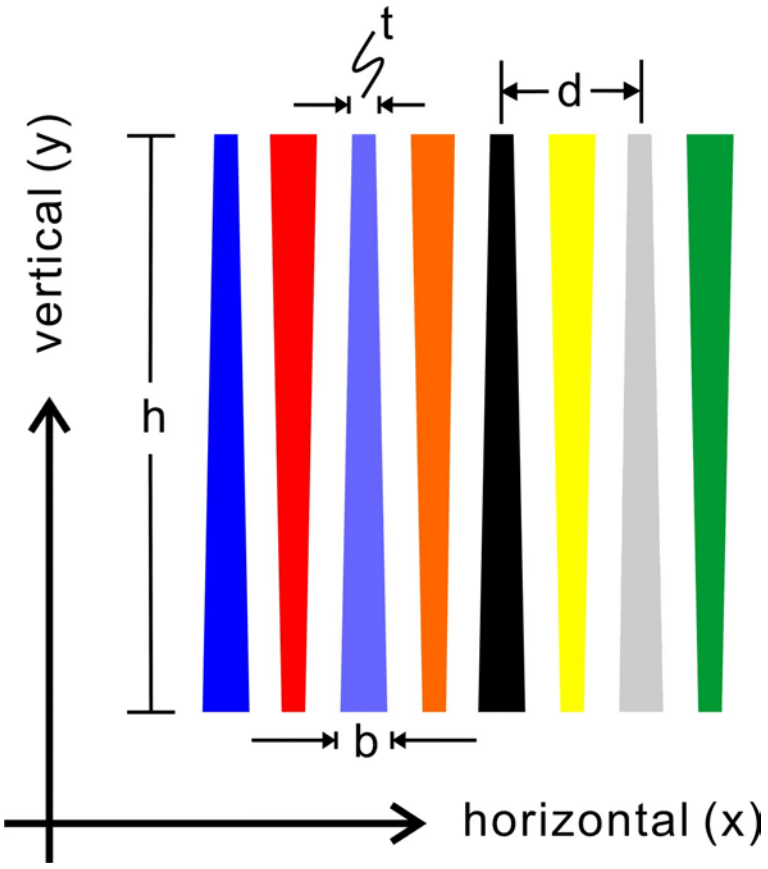

Figure 43 Color-coded flip-flop electrodes

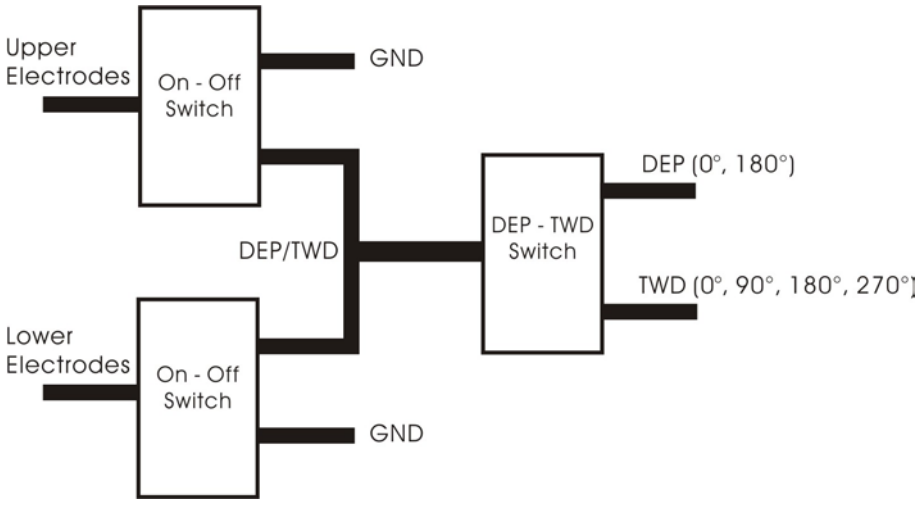

Figure 44 Modified switch circuits for flip-flop electrodes

Table 7 Electrode color code for upper and lower electrodes

Electrode	*Color Code*
U1 (Upper 1)	Red
U2	Orange
U3	Yellow
U4	Green
L1 (Lower 1)	Blue
L2	Purple
L3	Black
L4	Grey

The concept behind the flip-flop electrodes and the 4-directional movement is based on the idea that TWD can be performed on the flip-flop electrodes at three distinct vertical positions with the banding effect discussed in Section 5.1. The three vertical positions are labeled as upper, medium, and lower bands. The bottom of the lower electrodes is used as the bottom reference and the top of the upper electrodes as the top reference for a measured distance of 1000 μm in between. The upper band is located at 650 μm above the lower reference point and it is achieved by activating DEP signals on the upper electrodes while grounding the lower electrodes. The voltage pattern of the upper band is shown in Mode 1 of Table 8. The medium band is accomplished by activating both the upper and the lower electrode with DEP signals. Because of the structure of the flip-flop electrodes, the upper electrodes are activated with DEP signal of phase 0° while the lower electrodes are activated with phase 180° signals. Together they form a repeated 0° to 180° phase pattern horizontally across the electrodes and the band forms at 500 μm, the medium point between the upper and the lower reference points. The voltage pattern for the medium band is shown in Mode 3 of

Table 9. The lower band is achieved by inversing the voltage pattern of the upper band. The upper electrodes are grounded while the lower electrodes are activated with DEP signal. The voltage pattern for the lower band is shown in Mode 2 of Table 8 and the lower band forms at 350 μm above the reference point.

Table 8 Waveform pattern for vertical movements

Electrode	*Mode 1 (Up)*	*Mode 2 (Down)*
U1	0°	GND
U2	180°	GND
U3	0°	GND
U4	180°	GND
L1	GND	0°
L2	GND	180°
L3	GND	0°
L4	GND	180°

Table 9 Waveform pattern for medium band

Electrode	*Mode 3 (Medium)*	*Mode 4 (Left)*	*Mode 5 (Right)*
U1	0°	90°	180°
U2	0°	270°	0°
U3	0°	90°	180°
U4	0°	270°	0°
L1	180°	0°	270°
L2	180°	180°	90°
L3	180°	0°	270°
L4	180°	180°	90°

The vertical movements to the three band positions are created with the DEP activations of the upper electrodes, the lower electrodes, and both. Similarly, the TWD activation of the upper electrodes, the lower electrodes, and all electrodes are responsible for the horizontal movements at the upper band, the lower band, and the medium band respectively. The direction of the horizontal movement is controlled by the signal generator. The signal generator sources the first two of four TWD sinusoidal waveforms in phase 0° and 90°. By changing the order of the phase shift to 90° and 0° for the first two waveforms, the direction of the TWD waves is reversed and hence the direction of horizontal movements is reversed as well. Mode 6 and 7 of Table 10 show the voltage patterns for achieving horizontal movements at the upper and the lower band positions respectively. At the medium position, both the upper and the lower electrodes are involved in sourcing the voltage patterns in Mode 4 and 5 of Table 9.

Table 10 Waveform pattern for horizontal movements

Electrode	*Mode 6 (Left)*	*Mode 7 (Right)*
U1/L1	0°	270°
U2/L2	90°	180°
U3/L3	180°	90°
U4/L4	270°	0°

To demonstrate the flip-flop electrode design, a mixture of microbeads in 1 mS/cm KCl medium was pumped into the microfluidic chamber and DEP signals of 8 $V_{peak\text{-}to\text{-}peak}$ were activated at either the lower or the upper electrodes. The banding of the microbeads was immediately visible. The upper and the lower band positions were then recorded and compared at different frequencies. Figure 45 shows the shifting of microbeads from the lower band to the upper band. To demonstrate the repeatability of the shifting technique, the band positions are marked with black lines. The medium band position was then turned on with the activations of both the lower and the upper electrodes. At each of the vertical positions, TWD was applied to demonstrate horizontal movements. The activation of TWD was preceded by DEP to establish the vertical position. The residue banding effect from DEP allowed the particles to move in one straight line when activated with TWD later. Without DEP activation first, applying TWD to the upper electrodes caused particles to move individually toward the end of the upper electrodes without any group formations. In addition, frequencies from 1 KHz to 10 MHz were tested with the flip-flop electrodes and at each frequency banding effect was observed. However, microbeads responded quicker and formed bands faster in relative higher frequencies than the lower frequencies. Above 1 MHz, however, no major discrepancies in speed or band position were observed. By increasing the voltage to 10 $V_{peak\text{-}to\text{-}peak}$, faster particle movements were observed in the experiment. However, irregular particle movements due to electroosmotic flow at higher voltages negated any possible improvements.

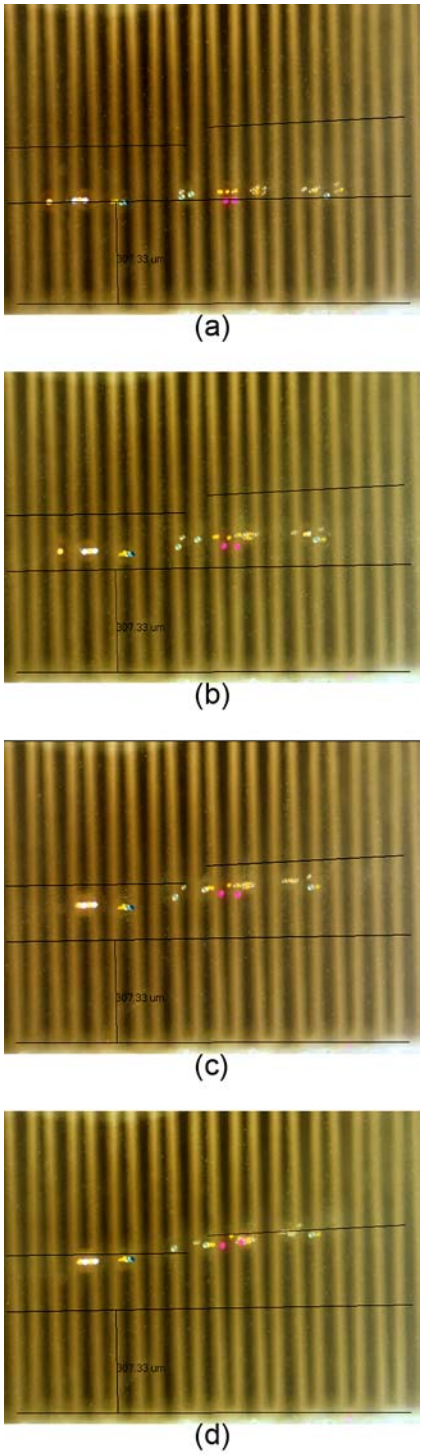

Figure 45 Photographs of shifting in vertical band positions

The ability to move the target particles vertically to one of three band positions and then manipulate them to move horizontally is useful in many applications. First, the flip-flop electrode design is immediately applicable to particle sorting applications. With the use of an optical microscope and the flip-flop electrodes, particles in the microfluidic chamber can be monitored and moved to one of the vertical three positions using DEP and then into one of the six split channels using TWD as shown in Figure 46. Because of the lower throughput and the requirement of an optical microscope, this is best suited for single-cell manipulation where precision is a more important quality than efficiency. In addition, with some minor modifications to the electrode structure, we can create a particle distributor that is capable of dividing a sample into two or three equal parts. This can be achieved by continuously pumping the sample into the microfluidic chamber while carrying out repeated DEP activations for the three vertical positions in the background. With a careful control of the time between the lower, medium and upper band positions, the particle stream has an equal chance of being directed into one of the three channels. This application works best with a large sample of small particles where the flow rate can be tuned down for the vertical deflections to take place.

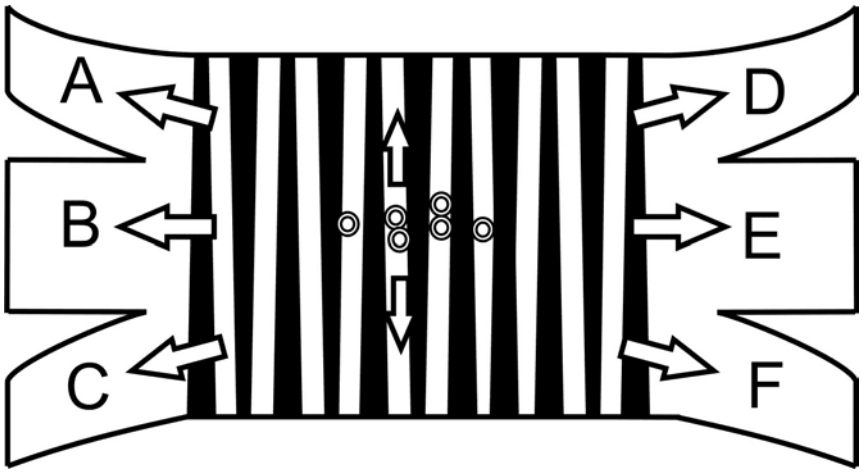

Figure 46 Conceptual drawing of a cell separator with 6 exits

Chapter 6
Future Outlook

6.1 Three Dimensional Design Enhancement

Figure 47 shows the conceptual design of a three-dimensional (3D) enhancement to the existing parallel track design. The three-dimensional design adds a height dimension (z-axis) to the electrode tracks. Two identical glass wafers with gold electrodes are placed so their electrode sides face each other with separation provided by two polystyrene spacers. The upper electrodes are aligned so they are placed directly over the interdigit gaps of the lower electrodes. In this way, there are no electric field minima in between the electrodes except the nDEP cages in the middle of the channel. The electrodes on each layer are applied with DEP signals and together they form nDEP cages that can gather and trap target particles. Since each electrode is individually controlled, a specific number of nDEP cages can be generated at the desired locations. Simulations show that to generate a single nDEP cage, a minimum of 6 electrodes are required. In Figure 47, voltage configuration of 5 V and -5 V are displayed within the electrodes to simulate an instance when the nDEP cages are generated.

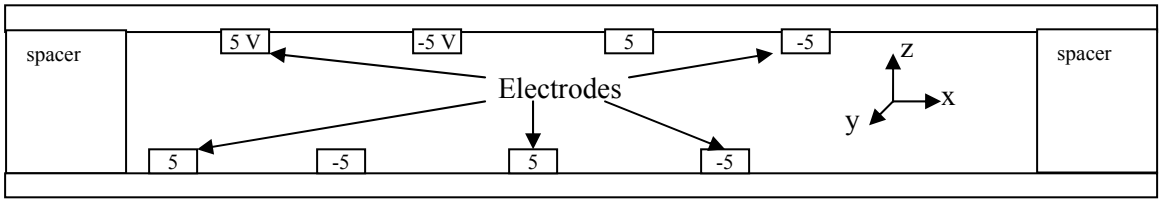

Figure 47 Three dimensional parallel track design with electrode voltage 5 and -5 V

6.1.1 Simulation and Explanation

The simulation of electric field strength in the proposed 3D system is shown in Figure 48. It shows three distinct electric minima represented by the dark blue circles in the middle of the channel. The electric field minima are circular in shape and can be used as nDEP cages. The nDEP cages suspend the target particles in the space between the upper and the lower electrodes where the electric field minima occur. The three cages are supported by 10 activated electrodes in a voltage configuration identical to the one shown in Figure 47.

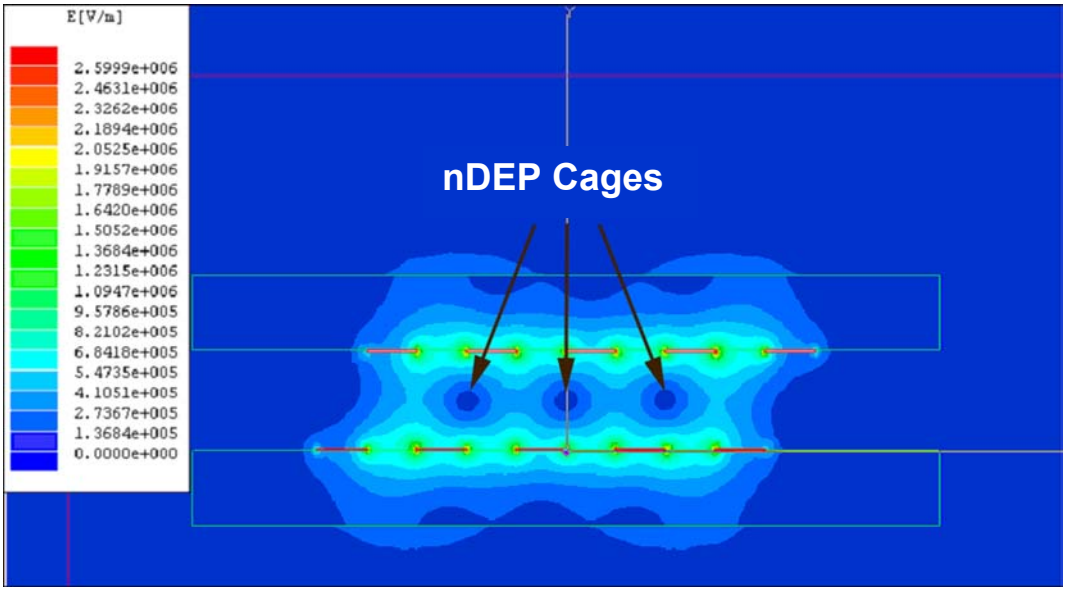

Figure 48 Simulation of electric field strength for 3D design

For reasons of simplicity and clarity, the number of simulated nDEP cages is reduced from three to one. Each of the nDEP cages is supported by a minimum of 6 activated electrodes. In Figure 49 a) – f), the nDEP cage is controlled by voltage switching to go from left to right. The size of nDEP cage is stable and the transition from one stage to another is smooth. The speed of the transition is determined by the speed of voltage switching and can be slowed down if the particles contained have trouble following the movement of the nDEP cage. The

strength of the nDEP cages can also be adjusted by changing the magnitude of the voltage, the height of the channel, and the conductivity of the fluid medium.

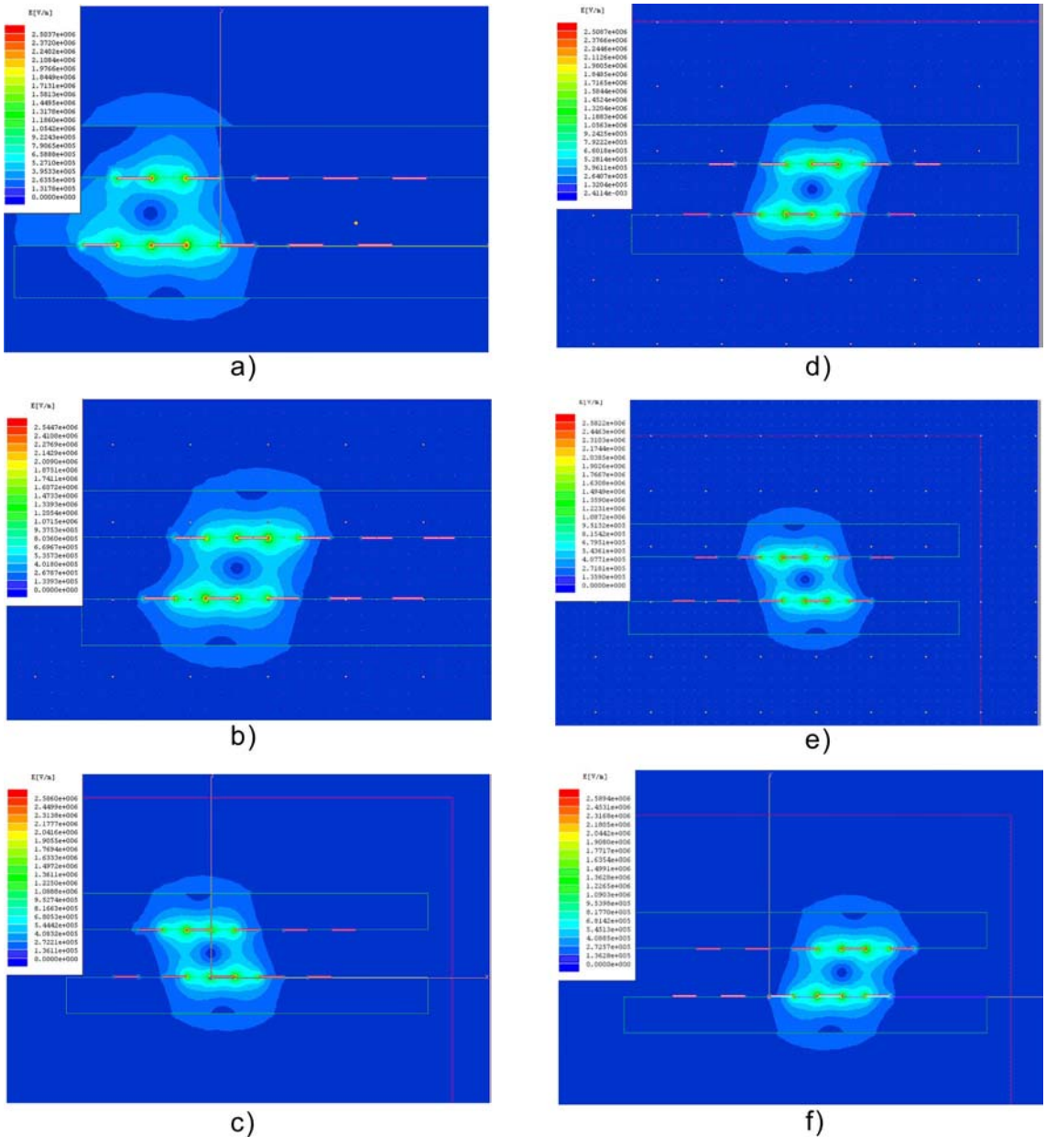

Figure 49 Transition of electric field minima from left to right

The generation of the electric field minima and the nDEP cages is achieved through a pattern of voltage signals sourced by 6 surrounding electrodes. The voltage configuration is shown in Table 11. The key to a well-defined nDEP cage is marked by an X configuration generated by the four nearest electrodes. Because of the two pairs of opposite electrodes have the same voltage, an electric field minimum ($E_{\min}$) is created at the center of the X shown in Table 11. The transportation of the nDEP cage shown in Figure 49 a) – f) is achieved by shifting the voltage pattern in Table 11 by one electrode to the right. This involves grounding the left-most electrode and turning on the electrode adjacent to the right-most electrode.

Table 11 Electric field minima pattern

5	-5	5
	E_{min}	
5	-5	5

6.1.2 Advantages and Challenges

The major benefit of the 3D enhancement is the addition of one vertical dimension in the parallel track design. Many more electric field configurations can be formed by combining the voltage patterns of the upper and the lower electrodes. Because electric fields are inherently three-dimensional, the ability to manipulate electric fields in all three dimensions is very important. The 3D design also allows us to increase the strength of electric fields through constructive interferences. A summary of the advantages offered by the 3D system are listed below,

1. The 3D enhancement is easy to understand and simulate. nDEP is a well-studied phenomenon.

2. Two one-layer electrodes are required. The complexity of construction is reduced compared to other 3D systems.

3. Implementation of the control system is simplified. Only two opposing voltage signals are used.

4. The 3D device will generate very strong negative elevation and trapping force at the center of the minima through constructive interferences of the electric fields.

5. The 3D device allows us to control the direction, movement, and speed of the transportation to the resolution of the width of one single electrode.

In addition to particle trapping and transportation, the separation of particles can be achieved by exploiting the particles' differences in permittivity values. Particles with high permittivity will experience pDEP and stick to the edge of electrodes where the electric field maxima reside. Those with a lower permittivity than the surrounding medium will experience nDEP force and suspend in the middle of the channel. Once the target particles are removed by the transportation method shown in Figure 49, the remained particles are washed away and collected.

To implement this design, two major challenges present themselves. First, the top layer electrodes obscured the field of view under an upright microscope. One possible solution to enhance visibility is by the use of transparent and conductive material for constructing the top electrodes. ITO is one candidate material since it provides good visibility and is highly conductive. Second, accurate positioning of electrodes is crucial in generating nDEP cages and thus aligning the two glass wafers with electrodes become a difficult task. Calibration wires in both X-axis and Y-axis can assist the alignment. Micromanipulators can be used to move the top glass plate into place. A technique will need to be developed to improve the precision of the alignment.

6.2 Cell Superhighway Concept

Cell superhighway refers to the DEP device that mimics the concept of today's highway. Like our expressways, fast moving particles are separated from the slow ones by lanes. Two or more lanes are created on the surface of the electrodes and each one is reserved for a specific type of cells. The horizontal differentiation of cells can be created while still maintaining TWD, meaning that faster cells will move forward as they "change lanes." This is achieved by exploiting DEP's dependence on geometric shapes of the electrodes. Certain geometric shape can be found so that the invisible boundaries of each lane are created by the differences in the electric field strengths. The further investigation of an interdigit triangular electrode structure is proposed here. Figure 50 displays a concept drawing of the cell superhighway. It is a simplified representation of the final goal of the cell sorting device.

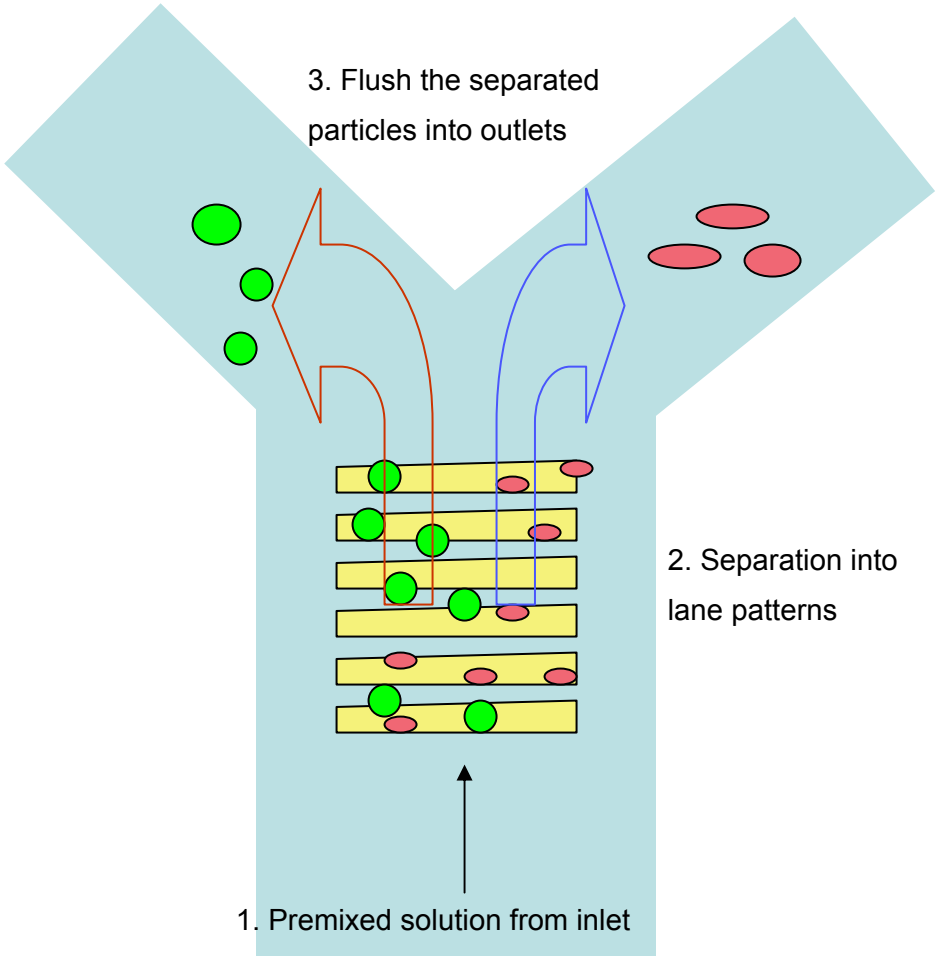

Figure 50 Cell superhighway concept

6.2.1 Simulation and Explanation

In Figure 51, across the electrodes from left to right, bands of electric fields are created with different intensities. These bands of electric fields form the lanes of the cell superhighway. Cells with different permittivity values will congregate at different bands. For example, cells with a higher permittivity than the medium will experience pDEP forces and move to the areas of electric field maxima, represented by the color red, in Figure 51. Conversely, cells that experience nDEP forces will move to the left of the electrodes where the electric fields are the lowest.

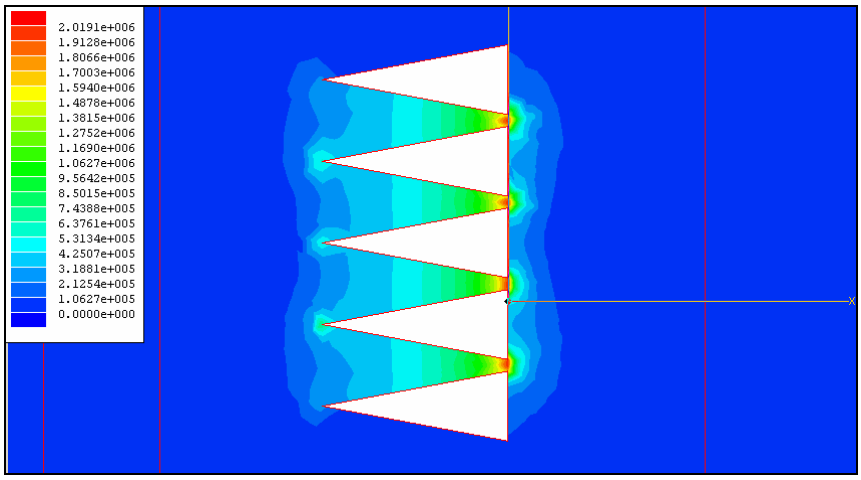

Figure 51 Cell superhighway with DEP voltage 5V and -5V

The challenge for the electrode design in Figure 51 is to eliminate the unwanted electric field maxima at the tips of the triangles. Because of the geometry effect, sharp points create regions of slightly higher electric fields than their immediate surroundings. Cells that experience pDEP and locate close to the tips will congregate at the local maxima instead of moving to the desired lane at the right. One potential solution is to dull the tips of the triangle as shown in Figure 52. In addition, the electrodes in Figure 52 are more elongated by design to generate more varied electric field strengths. The longer electrodes also provide more room for wider lanes and thus a more effective separation of cells.

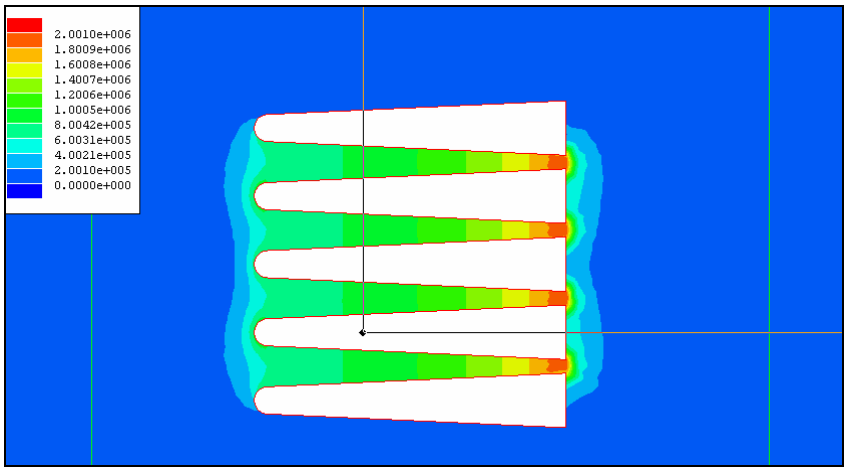

Figure 52 Modified electrodes with more elongated form

6.2.2 Advantages and Challenges in Superhighway Design

The advantages of the cell superhighway are apparent. The use of a purely electrical device to perform collection, separation, and transportation in one step is a considerable improvement over the existing microfluidic separation devices. Lane structures on the cell superhighway result in the parallel processing of multiple target cells at the same time. The elimination of a microfluidic pump will save substantial power and expense in a portable analysis system. The further advantages of the superhighway design are summarized in the following list:

1. Cell sorting in the cell superhighway means immediate structure-based cell sorting. No microfluidic is involved.

2. The highway analogy is easy to understand and easy to explain.

3. More complex structures can be built on the simple lane structure. For example, express lanes can be created for transporting more important cells. Highway entrance points and highway exit points are established for adding and subtracting cells and reagents. Merging and splitting lanes are made for mixing and separation of particles.

4. The cell superhighway design is immediately applicable. Everything is built on existing knowledge of DEP and TWD. Thus it should be relatively easy to simulate and analyze.

The challenges in the cell superhighway concern mostly the manufacturing of the elongated electrodes with rounded tips. The lanes are created by the varying distances in between the electrodes. However, the electrode gap at its widest cannot be too large. The ideal gap width is the same as the diameter of the target particles [69, 92]. If the mammalian cells are the target, the ideal width of the separation will be 10 to 20 μm. This poses a nontrivial challenge for designing the electrodes. The ideal dimensions for the electrodes will balance several criteria, 1) long and thin electrodes, 2) interdigit gap less than 50 μm, 3) small rounded tips, and 4) large width differences between the tip and the base. It is possible that a small change in interdigit gap distance will make a large difference in electric fields and criterion 4) will not be as significant. If the assumption is correct, the change in the width of the electrodes is best to remain gradual and within the manufacturing limitation. Another challenge for the cell superhighway lies in the fundamentals of TWD. In Chapter 2, it is shown that one of the precursors for TWD is nDEP. TWD needs nDEP forces to levitate the particles before the translational movements can take place. Target particles that experience pDEP forces will be trapped on the electrodes. In other words, the cell superhighway design will create only one fast lane and one stalled lane where pDEP particles are stuck on the electrodes and unable to move. One possible solution is to increase the translational force so TWD is large enough to overcome the attractive force of pDEP. At this point, it is not clear that the large countering TWD force is possible. However, from results shown in Chapter 5 it is promising that different particles will experience different levels of nDEP and occupy different lanes. Thus the medium conductivity can be adjusted so that all cells experience pDEP force over the cell superhighway. The chance of a “traffic jam” by sticky cells is then eliminated.

6.3 Field Programmable Gate Array Enhancement

FPGA stands for Field Programmable Gate Array. It contains programmable logic blocks that can be programmed to perform functions of basic logic gates. Programming of the hardware is achieved with a development tool that translates codes written in hardware description language (HDL) or schematics to machine language. Advantages of FPGA over Application Specific Integrated Circuit (ASIC) include cost and shorter development time. These advantages make FPGA very attractive for prototyping an analog waveform generator that can generate arbitrary voltage waves for DEP. The FPGA prototyping station provided by Canadian Microelectronics Corporation (CMC) uses a Xilinx Virtex-II Pro core. The Xilinx Virtex-II Pro is a power development tool that contains advanced logic, performance, memory, an IBM 400 MHz PowerPC processor, and 622 Mbps to 6.25 Gbps full duplex serial transceivers. Its high clock speed is ideal for generating high frequency sinusoidal waves.

The Xilinx Virtex-II Pro development core comes with the Amirix AP1000 development board that contains a multitude of connectors including a serial port, an Ethernet port, a JTAG interface through Parallel-IV connector, and a CompactFlash card port. The functionality of the FPGA board is expanded by the installation of an Analog I/O expansion card over the PCI mezzanine card (PMC) interface. With a breakout board, the Analog I/O expansion card can source up to 64 independent digital signals and 8 analog signals via coaxial cables. The Digital to Analog Converter (DAC) provides an 8-bit resolution for the analog signals which means up to 256 levels in the voltage signal can be achieved.

6.3.1 New Circuit Design

In order to use the FPGA board, a new electronic circuit is needed to protect the expensive equipment in the events of a short circuit or a power surge. The isolation circuitry will serve as a safety measure and completely isolates the FPGA board from the rest of circuitry. The isolation circuit is achieved using the opto-isolators. The opto-isolator is an electronic device that uses optics to transfer a signal while keeping the receiving and transmitting circuits

electrically isolated. This is done using light emitting diode on the transmitting end and light sensitive photo-diodes on the receiving end. A typical isolation provided by Toshiba TLP 332 photocoupler is 10^{11} Ω. In Figure 53, the schematic shows the position of the opto-isolator in the entire circuit. It is placed in between the FPGA and the differential amplifier AD8132AR. The opto-isolator's fast response time means the integrity of the FPGA signal is maintained and any distortion is kept at a minimum.

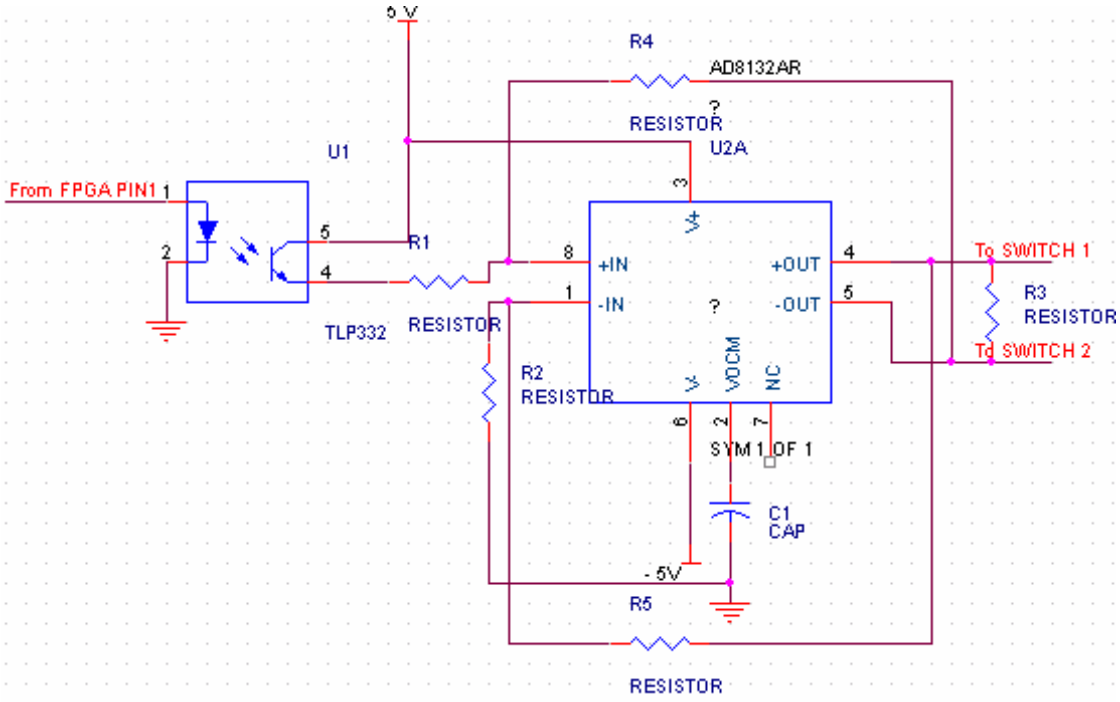

Figure 53 Schematic of isolation circuit

6.3.2 Software Design

The Virtex-II Pro FPGA on the AP1000 board can be programmed in several ways including the use of the following, a Xilinx Parallel-IV download cable, a CompactFlash memory card, and Flash memory. The software development is accomplished with the Xilinx Platform

Studio. Specifically, the Embedded Development Kit (EDK) and the Xilinx EDK supporting C language programming are used. Any FPGA-based signal generator is required to output 4 independent sinusoidal waveforms with frequency exceeding 1 MHz and duty cycle of 50% in order to perform DEP experiments. The flow chart diagram for the software program is presented in Figure 54. Interrupt Service Routine (ISR) is used to toggle the voltage high or low depending on the counter. Each time the ISR finishes, the timer flag and the count register are updated. With the FPGA idling most of the time, it is possible for FPGA to control other electronic equipments such as the oscilloscope and the conductivity meter since the AP1000 board is capable of communicating in serial via the RS232 port as well as TCP/IP via the Ethernet port. Most of the modern laboratory equipments come equipped with either RS232 port or Ethernet port. In a connected system, the experiment data can be downloaded from the sensor equipment and stored onto the CompactFlash memory card for easy access. An Apache web server is built into the Linux core operation system on AP1000's Read Only Memory (ROM). Thus data can be accessed and the experiment parameters can be changed in real time from a website hosted by AP1000. The final integrated system will have a command center in the AP1000 FPGA board, an online component for downloading results, a communication block for talking to the connected instruments, and a DEP waveform generator that can perform DEP and TWD experiments.

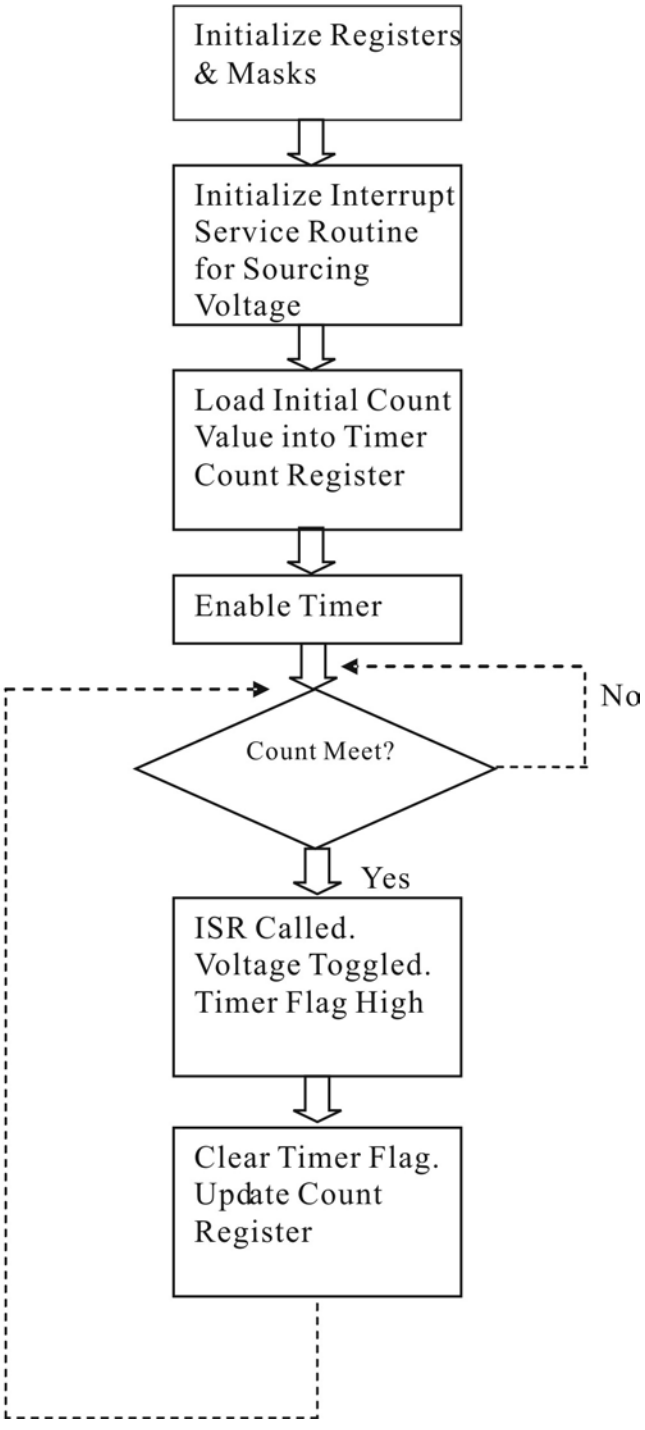

Figure 54 Flow chart diagram for FPGA

6.3.3 Improvements over Existing Design

The current design in Chapter 4 uses an expensive, non-portable waveform generator which only function is to generate sinusoidal waveforms in the range of 500 KHz to 5 MHz. The waveform generator can be replaced by a portable FPGA station that is less expensive and consumes less power. Furthermore, the FPGA station can be used to control other instruments in the system. It can talk to the oscilloscope and the conductivity meter by means of RS232 serial communication. It is able to store the measurement data on a CompactFlash card or a network drive for online access. Figure 55 is a graphical representation of the role of FPGA in an integrated DEP system. Table 12 compares the waveform generator system with the new FPGA system on cost, portability, power consumption and more.

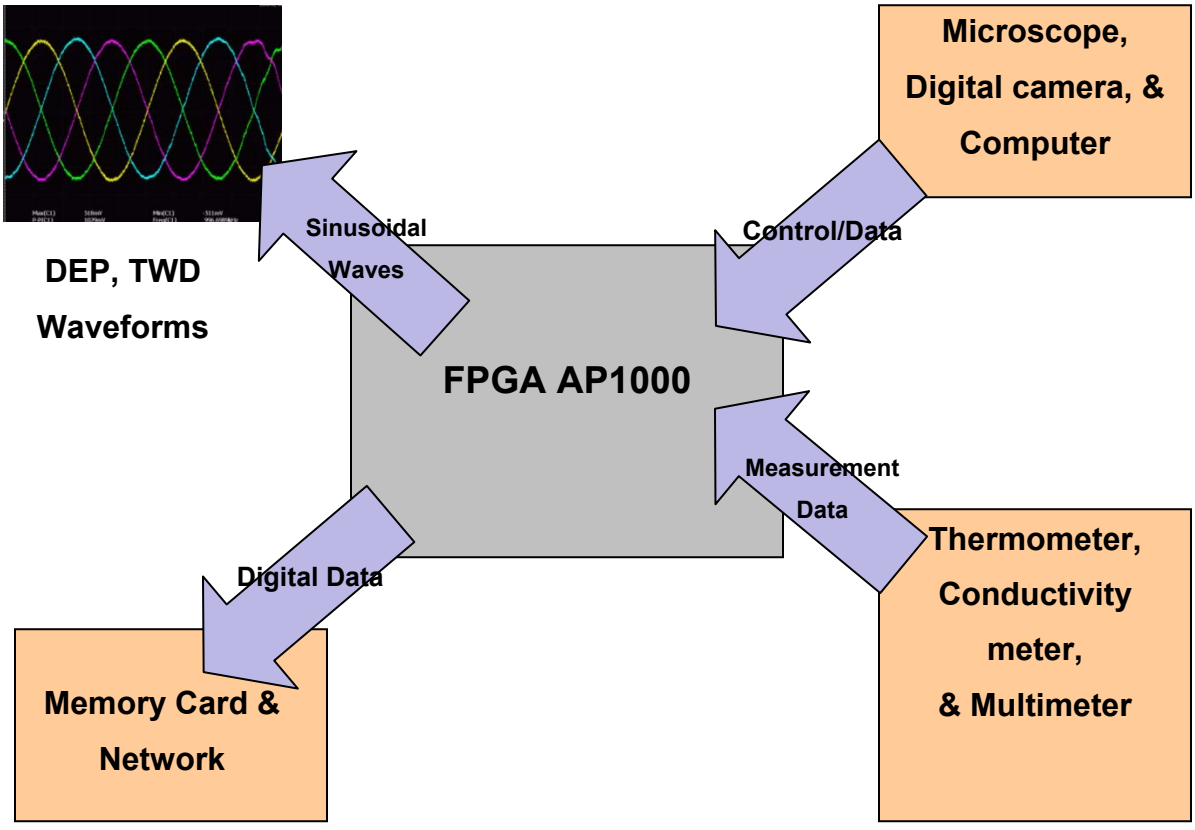

Figure 55 Role of FPGA in TWD experiments

Table 12 Comparison of waveform generator and FPGA

	Waveform Generator	**FPGA**
Cost	~$10,000	~$1000
Portable	No	Yes
Power by Battery	No	Yes
Generate sinusoidal waveform	Yes	Yes (with I/O card)
Serial communication with devices	With controlling computer	Input/Output with devices via RS232 serial or TCP/IP communication
Data	Manually captured and stored	Automatic recorded and stored on memory card

6.4 Conceptual Blood Analysis System

Figure 56 shows the conceptual drawing of a complete blood analysis system. The design of the system is modular with different stages that can perform independent processes. The first stage, the injection of sample into the biochip, is carried out with an external fluidic system. A tiny sample of blood is collected from the patient and injected from the syringe directly into the system. A holding chamber collects the blood sample. Through fluidic pressure the blood cells reach the second stage where the separation of different cell types occurs. The organization of cells into distinct lanes is based on the cell superhighway concept noted in

Section 6.2. The separation and the extraction of white blood cells occur on the parallel array structure and further transportation of the target cells is carried out by TWD. TWD carries the cell into the third stage of cell processing which involves high voltage and non-reversible electroporation. Electroporation is a well documented phenomenon where high strength electric fields create pores on cell membranes [93, 94]. The non-reversible electroporation utilizes longer and stronger pulses of electric fields which cause the disintegration of the cell membrane. Even after the pulses stopped, the cell membrane is unable to maintain its normal shape and the contents of the cell diffuse out. Since the innards of cell remain intact, the non-reversible electroporation provides an effective way to expose DNA and other organelles to the outside world. The electroporation of the white blood cells is followed by the final stage of the analysis system – the collection of cellular DNA via electrophoresis or DEP. DNA strands are inherently charged particles. Traditionally electrophoresis is used to collect DNA strands which can be incorporated in the system [95-97]. However, recent studies have shown that DEP is also an effective means to collect DNA strands [47, 66].

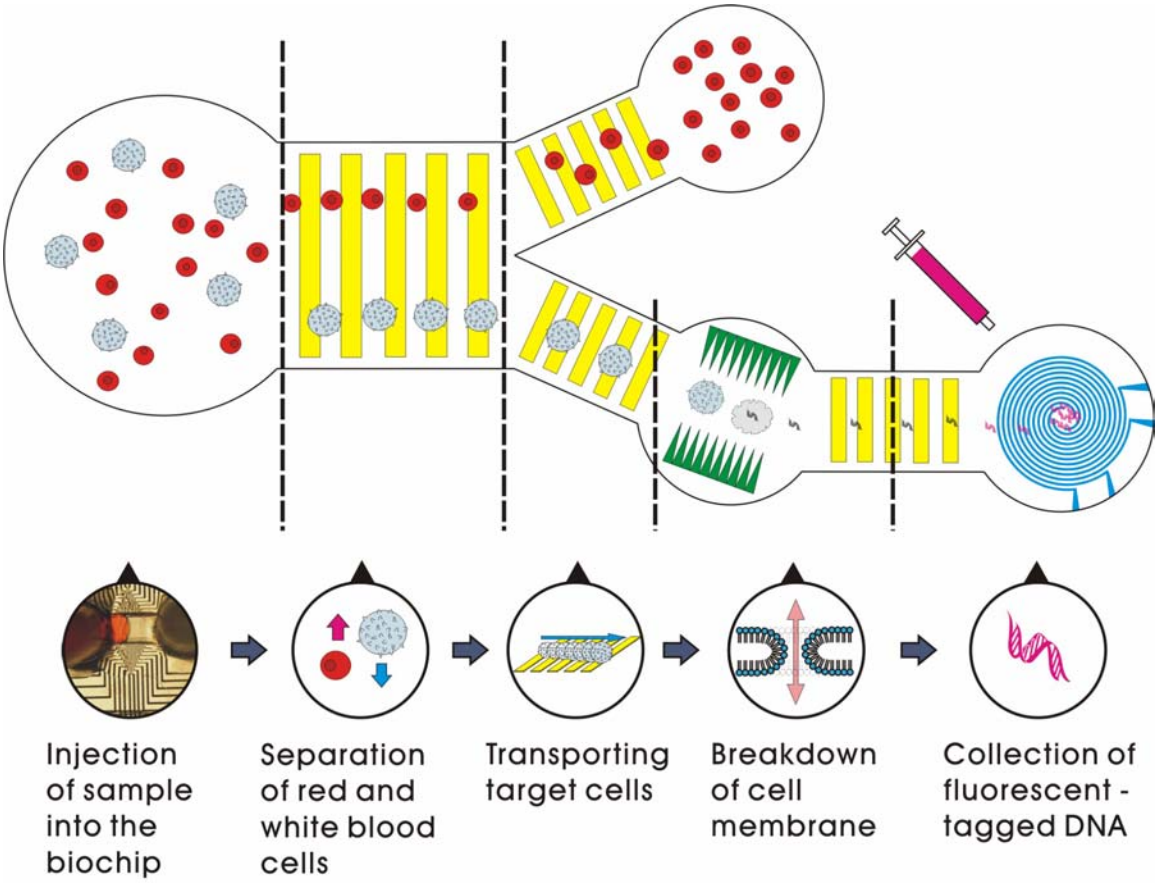

Figure 56 Conceptual drawing of a blood analysis system

6.5 Summary and Outlook

The overall goal of this research is to present an original device to enhance DEP effects through novel geometry of the electrodes. Implemented with a simple single-layer metal process, the microchip device consists of individually triangular-shaped electrodes in a parallel array. When activated with DEP waveforms, the novel-shaped electrodes generate horizontal bands of increasing electric fields. With these bands of electric fields, dielectric microbeads in a suitable medium can be manipulated to form a straight horizontal line at a predictable location over the electrodes. Further experiments show that the location of the microbeads is sensitive to the frequency of the applied DEP waveforms. By changing the

frequency, the line of microbeads can be shifted vertically along the electrodes. In addition, horizontal movements of the microbeads can be achieved with TWD. With an accurate control of both vertical and horizontal positions and a potential multi-lane separation strategy, our device delivers substantial improvements over the existing electrode array devices. In addition, three future enhancements to the current microchip device are described in detail. The 3D enhancement adds an identical microchip to the existing device by separating them with polystyrene spacers. When both microchips are activated with DEP waveforms, strong nDEP are formed over the electrodes by constructive interference. The nDEP cages are used to suspend target particles in the middle of the channel. The major advantage of the 3D enhancement is the improved control over the electric fields. It allows precise control of the direction, movement, and speed of the traveling particle to the resolution of the width of one single electrode. The second improvement is the cell superhighway. The cell superhighway is a concept that the current microchip can be made to mimic today's highway system in its structure and function. Separation of target particles can be achieved by creating multiple lanes with each lane occupied by single type of particle. Additional structures for the purpose of merging, splitting, and priority transportation can be built on the existing highway structure. A successful cell superhighway device will be a high-throughput, electrical device that handles collection, separation, and transportation of target particles with a high level of parallel processing. Another simple yet important enhancement for the microchip device is the replacement of the bulky waveform generator with a portable FPGA board. An AP1000 FPGA board with a digital-to-analog converter card and a breakout board can source up to 8 independent analog signals with a 256-level resolution. The processing power and connectivity of a FPGA board can be used to control other measurement instruments and store the recorded data onto a memory card. An integrated data acquisition system with the FPGA board at its core can automate the entire experiment process including waveform generation, data collection, and data storage. This system can be realized with a fraction of the cost of the current waveform generator.

In today's world of rising healthcare cost, cell manipulation technology has become an increasingly important research topic. With recent advances in microfabrication techniques, researchers have made great stride in making ubiquitous point-of-care testing a reality. The trend today is toward a computer chip device with electrode-embedded chambers and an interconnecting fluidic channel network. Since most of the cell manipulation techniques utilize DEP and electroporation, the same electrode patterns can be reused to reduce manufacturing cost. The introduction of μTAS such as i-STAT's blood analyzer into the medical market signals the commercialization of LOC technology is well underway. The research presented in this report contributes to the undertaking by providing the foundation and the blueprint for an automated blood analysis system. In the near future, it is clear a downloading of responsibilities will take place in the medical hierarchy. The family doctors will be the ones that perform biosample analysis and we will begin to see a more personal and efficient healthcare system for the patients.

Bibliography

[1] S. Whitley, "Review of the gas centrifuge until 1962. I. Principles of separation physics," *Reviews of Modern Physics,* vol. 56, pp. 41-66, 01. 1984.

[2] S. Whitley, "Review of the gas centrifuge until 1962. II. Principles of high-speed rotation," *Reviews of Modern Physics,* vol. 56, pp. 67-97, 01. 1984.

[3] J. Gehl, "Electroporation: theory and methods, perspectives for drug delivery, gene therapy and research." *Acta Physiologica Scandinavica,* vol. 177, pp. 437, 2003.

[4] A. J. Tudos, G. A. J. Besseling and R. B. M. Schasfoort, "Trends in miniaturized total analysis systems for point-of-care testing in clinical chemistry," *Lab on a Chip,* vol. 1, pp. 83-95, 12. 2001.

[5] P. R. C. Gascoyne and J. V. Vykoukal, "Dielectrophoresis-based sample handling in general-purpose programmable diagnostic instruments," *Proc IEEE,* vol. 92, pp. 22-42, 01. 2004.

[6] Y. Ghallab and W. Badawy, "Sensing methods for dielectrophoresis phenomenon: from bulky instruments to lab-on-a-chip," *IEEE Circuits and Systems Magazine,* vol. 4, pp. 5-15, 2004.

[7] G. J. Kost, S. S. Ehrmeyer, B. Chernow, J. W. Winkelman, G. P. Zaloga, R. P. Dellinger and T. Shirey, "The laboratory-clinical interface: point-of-care testing." *Chest,* vol. 115, pp. 1140, 1999.

[8] G. Davis, "Microfabricated sensors and the commercial development of the i-stat point-of-care system," in Anonymous 1998, pp. 47.

[9] K. A. Erickson and P. Wilding, "Evaluation of a novel point-of-care system, the i-STAT portable clinical analyzer." *Clinical Chemistry,* vol. 39, pp. 283, 1993.

[10] P. A. Gibson and A. D. Stoyenko, "Development and integration of a concurrently executing interactive user interface for the I-STAT portable clinical analyzer. A case study in real-time systems integration," *Journal of Systems Integration,* vol. 2, pp. 349-87, 10. 1992.

[11] i-STAT Corp. (1997), Comparing traditional blood analysis costs to point-of-care testing costs. [Online]. *2007(Jun. 23),* pp. 12. Available: www.i-stat.com/products/docs/151420.pdf

[12] P. Stubbs and P. O. Collinson, "Point-of-care testing: a cardiologist's view," *Clinica Chimica Acta,* vol. 311, pp. 57, 2001.

[13] L. Thiebe, K. Vinci and J. Gardner, "Point-of-care testing: Improving Day-Stay services," *Nurs. Manage.,* vol. 24, pp. 54-56, 1993.

[14] J. Janata, "Electrochemical microsensors," *Proc IEEE,* vol. 91, pp. 864-869, 2003.

[15] C. D. Chin, V. Linder and S. K. Sia, "Lab-on-a-chip devices for global health: past studies and future opportunities," *Lab on a Chip,* vol. 7, pp. 41-57, 01. 2007.

[16] A. Manz and J. C. T. Eijkel, "Miniaturization and chip technology. What can we expect," *Pure and Applied Chemistry,* vol. 73, pp. 1555, 2001.

[17] A. Manz, D. J. Harrison, E. M. J. Verpoorte, J. C. Fettinger, A. Paulus, H. Ludi and H. M. Widmer, "Planar chips technology for miniaturization and integration of separation techniques into monitoring systems: capillary electrophoresis on a chip," *Journal of Chromatography,* vol. 593, pp. 253, 1992.

[18] A. Manz, N. Graber and H. M. Widmer, "Miniaturized total chemical analysis systems: A novel concept for chemical sensing," in *5th International Conference on Solid-State Sensors and Actuators and Eurosensors III,* 1990, pp. 244-8.

[19] S. C. Jakeway, de Mello, A. J. and E. L. Russell, "Miniaturized total analysis systems for biological analysis." *Fresenius' Journal of Analytical Chemistry,* vol. 366, pp. 525, 2000.

[20] D. Meldrum, M. Holl, P. Seriburi, S. Phillips, S. H. Chao, L. Jang and F. Kosar, "MEMS modules for life-on-a-chip," in *Proceedings of the 2003 IEEE International Symposium on Circuits and Systems,* 2003, pp. 638-641.

[21] G. Ramsay, "DNA chips: state-of-the art." *Nature Biotechnology,* vol. 16, pp. 40, 1998.

[22] K. M. Kurian, C. J. Watson and A. H. Wyllie, "DNA chip technolgy," *J. Pathol.,* vol. 187, pp. 267-271, February 1999. 1999.

[23] R. Bogue, "MEMS sensors: Past, present and future," *Sens Rev,* vol. 27, pp. 7-13, 2007.

[24] M. P. Hughes, R. Pethig and X. Wang, "Dielectrophoretic forces on particles in travelling electric fields," *J. Phys. D,* vol. 29, pp. 474-482, 1996.

[25] T. B. Jones, "Basic theory of dielectrophoresis and electrorotation," *IEEE Engineering in Medicine and Biology Magazine,* vol. 22, pp. 33-42, 11. 2003.

[26] N. G. Green, "Electrode polarisation, dielectrophoresis and electrorotation," in *Electrostatics 2003,* 2004, pp. 193-8.

[27] H. A. Pohl, "Some effects of nonuniform [electric] fields on dielectrics," *J. Appl. Phys.,* vol. 29, pp. 1182-1188, 08. 1958.

[28] M. P. Hughes, "Micro- and Nano-electrokinetics in Medicine," *IEEE Engineering in Medicine and Biology Magazine,* vol. 22, pp. 32, 2003.

[29] H. Zou, S. Mellon, R. R. A. Syms and K. E. Tanner, "2-dimensional MEMS dielectrophoresis device for osteoblast cell stimulation," *Biomed. Microdevices,* vol. 8, pp. 353-9, 12. 2006.

[30] T. P. Hunt and R. M. Westervelt, "Dielectrophoresis tweezers for single cell manipulation," *Biomed. Microdevices,* vol. 8, pp. 227-230, 2006.

[31] E. G. Cen, C. Dalton, Y. Li, S. Adamia, L. M. Pilarski and Kaler,K. V. I. S., "A combined dielectrophoresis, traveling wave dielectrophoresis and electrorotation microchip for the manipulation and characterization of human malignant cells." *Journal of Microbiological Methods,* vol. 58, pp. 387, 2004.

[32] R. Holzel, "Electrorotation of single yeast cells at frequencies between 100 Hz and 1.6 GHz," *Biophys. J.,* vol. 73, pp. 1103-9, 08. 1997.

[33] Y. Huang, R. Holzel, R. Pethig and X. Wang, "Differences in the AC electrodynamics of viable and non-viable yeast cells determined through combined dielectrophoresis and electrorotation studies," *Phys. Med. Biol.,* vol. 37, pp. 1499-517, 07. 1992.

[34] R. Zhou, P. Wang and H. Chang, "Bacteria capture, concentration and detection based on ac dielectrophoresis, electro-osmotic transport and self-assembly of single-wall carbon nanotubes," in *05AIChE: 2005 AIChE Annual Meeting and Fall Showcase,* 2005, pp. 14215.

[35] B. H. Lapizco-Encinas, B. A. Simmons, E. B. Cummings and Y. Fintschenko, "Insulator-based dielectrophoresis for the selective concentration and separation of live bacteria in water," *Electrophoresis,* vol. 25, pp. 1695-704, 06. 2004.

[36] Y. Huang, J. M. Yang, P. J. Hopkins, S. Kassegne, M. Tirado, A. H. Forster and H. Reese, "Separation of simulants of biological warfare agents from blood by a miniaturized dielectrophoresis device," *Biomed. Microdevices,* vol. 5, pp. 217-25, 2003.

[37] A. Docoslis, L. A. T. Espinoza, B. Zhang, L. Cheng, B. A. Israel, P. Alexandridis and N. L. Abbott, "Using nonuniform electric fields to accelerate the transport of viruses to surfaces from media of physiological ionic strength," *Langmuir,* vol. 23, pp. 3840-3848, 2007.

[38] F. Grom, J. Kentsch, T. Muller, T. Schnelle and M. Stelzle, "Accumulation and trapping of hepatitis A virus particles by electrohydrodynamic flow and dielectrophoresis," *Electrophoresis,* vol. 27, pp. 1386-93, 04. 2006.

[39] M. P. Hughes and H. Morgan, "Diffuse double layer effects observed by dielectrophoresis of Herpes Simplex Virus, type 1 (HSV-1)," *Annual International Conference of the IEEE Engineering in Medicine and Biology - Proceedings,* vol. 1, pp. 90, 1999.

[40] H. Morgan and N. G. Green, "Dielectrophoretic manipulation of rod-shaped viral particles," *J. Electrostatics,* vol. 42, pp. 279-293, 1997.

[41] S. Tuukkanen, J. J. Toppari, A. Kuzyk, L. Hirviniemi, V. P. Hytonen, T. Ihalainen and P. Torma, "Carbon nanotubes as electrodes for dielectrophoresis of DNA," *Nano Letters,* vol. 6, pp. 1339-1343, 2006.

[42] R. Holzel, N. Calander, Z. Chiragwandi, M. Willander and F. F. Bier, "Trapping single molecules by dielectrophoresis," *Phys. Rev. Lett.,* vol. 95, pp. 128102-1, 2005.

[43] N. G. Green and H. Morgan, "Dielectrophoresis of submicrometer latex spheres. 1. Experimental results," *J Phys Chem B,* vol. 103, pp. 41-50, 1999.

[44] G. H. Markx, R. Pethig and J. Rousselet, "Dielectrophoretic levitation of latex beads, with reference to field-flow fractionation," *J. Phys. D,* vol. 30, pp. 2470-2477, 1997.

[45] C. Ho, R. Lin, W. Chang, H. Chang and C. Liu, "Rapid heterogeneous liver-cell on-chip patterning via the enhanced field-induced dielectrophoresis trap," *Lab on a Chip,* vol. 6, pp. 724-34, 2006.

[46] L. Yang, P. P. Banada, M. R. Chatni, K. Seop Lim, A. K. Bhunia, M. Ladisch and R. Bashir, "A multifunctional micro-fluidic system for dielectrophoretic concentration coupled with immuno-capture of low numbers of Listeria monocytogenes." *Lab on a Chip,* vol. 6, pp. 896, 2006.

[47] D. J. Bakewell and H. Morgan, "Dielectrophoresis of DNA: Time- and frequency-dependent collections on microelectrodes," *IEEE Transactions on Nanobioscience,* vol. 5, pp. 139-146, 2006.

[48] T. B. Jones, *Electromechanics of Particles.* Cambridge, U.K.: Cambridge Univ. Press, 1995,

[49] Wikipedia. (2007, May 29). Electrical conductivity. [online]. *2007(June/01),* Available: http://en.wikipedia.org/wiki/Electrical_conductivity

[50] Wikipedia. (2007, May 23). Dielectric constant. [online]. *2007(June 01),* Available: http://en.wikipedia.org/wiki/Electrical_conductivity

[51] L. Cui and H. Morgan, "Design and fabrication of travelling wave dielectrophoresis structures," *J Micromech Microengineering,* vol. 10, pp. 72-79, 2000.

[52] Y. Huang, X. -. Wang, J. A. Tame and R. Pethig, "Electrokinetic behaviour of colloidal particles in travelling electric fields: studies using yeast cells," *J. Phys. D,* vol. 26, pp. 1528-1535, 1993.

[53] X. -. Wang, M. P. Hughes, Y. Huang and F. F. Becker, "Non-uniform spatial distributions of both the magnitude and phase of AC electric fields determine dielectrophoretic forces," *Bulletin of the Russian Academy of Sciences. Physics,* vol. 5843, pp. 185, 1994.

[54] B. M. Taff and J. Voldman, "A scalable addressable positive-dielectrophoretic cell-sorting array," *Anal. Chem.,* vol. 77, pp. 7976-7983, 2005.

[55] L. Qian, M. Scott, K. Kaler and R. Paul, "Integrated planar concentric ring dielectrophoretic (DEP) levitator," *Journal of Electrostatics,* vol. 55, pp. 65, 2002.

[56] J. Cheng, E. L. Sheldon, L. Wu, A. Uribe, L. O. Gerrue, J. Carrino, M. J. Heller and J. P. O'Connell, "Preparation and hybridization analysis of DNA/RNA from E. coli on microfabricated bioelectronic chips." *Nature Biotechnology,* vol. 16, pp. 541, 1998.

[57] C. Jing , S. L Edward, W. Lei , H. J Michael and O. P James, "Isolation of cultured cervical carcinoma cells mixed with peripheral blood cells on a bioelectronic chip," *Anal. Chem.,* vol. 70, pp. 2321-2326, 1998.

[58] R. Pethig, "Dielectrophoresis: Using Inhomogeneous AC Electrical Fields to Separate and Manipulate Cells," *Crit. Rev. Biotechnol.,* vol. 16, pp. 331, 1996.

[59] A. Narayanan, Y. Dan, V. Deshpande, N. D. Lello, S. Evoy and S. Raman, "Dielectrophoretic integration of nanodevices with CMOS VLSI circuitry," *IEEE Transactions on Nanotechnology,* vol. 5, pp. 101-9, 03. 2006.

[60] J. Cheng, E. L. Sheldon, L. Wu, M. J. Heller and J. P. O'Connell, "Isolation of cultured cervical carcinoma cells mixed with peripheral blood cells on a bioelectronic chip." *Analytical Chemistry,* vol. 70, pp. 2321, 1998.

[61] S. Asokan, L. Jawerth, R. L. Carroll, R. E. Cheney, S. Washburn and R. Superfine, "Two-dimensional manipulation and orientation of actin-myosin systems with dielectrophoresis," *Nano Letters,* vol. 3, pp. 431, 2003.

[62] S. Tsukahara, K. Yamanaka and H. Watarai, "Dielectrophoretic behavior of single DNA in planar and capillary quadrupole microelectrodes," *Chemistry Letters,* pp. 250, 2001.

[63] X. -. Wang, Y. Huang, J. P. H. Burt, G. H. Markx and R. Pethig, "Selective dielectrophoretic confinement of bioparticles in potential energy wells," *Journal of Physics D (Applied Physics),* vol. 26, pp. 1278-85, 08/14. 1993.

[64] K. F. Hoettges, M. B. McDonnell and M. P. Hughes, "Use of combined dielectrophoretic/electrohydrodynamic forces for biosensor enhancement," *J. Phys. D,* vol. 36, pp. 101-104, 2003.

[65] B. H. Lapizco-Encinas, B. A. Simmons, E. B. Cummings and Y. Fintschenko, "Dielectrophoretic Concentration and Separation of Live and Dead Bacteria in an Array of Insulators," *Anal. Chem.,* vol. 76, pp. 1571-1579, 2004.

[66] C. Chou, J. O. Tegenfeldt, O. Bakajin, S. S. Chan, E. C. Cox, N. Darnton, T. Duke and R. H. Austin, "Electrodeless dielectrophoresis of single- and double-stranded DNA," *Biophys. J.,* vol. 83, pp. 2170-9, 10. 2002.

[67] E. B. Cummings, "Streaming dielectrophoresis for continuous-flow microfluidic devices," *IEEE Engineering in Medicine and Biology Magazine,* vol. 22, pp. 75-84, 11. 2003.

[68] E. B. Cummings and A. K. Singh, "Dielectrophoretic trapping without embedded electrodes," in *Microfluidic Devices and Systems III,* 2000, pp. 164-173.

[69] M. P. Hughes, "Strategies for dielectrophoretic separation in laboratory-on-a-chip systems," *Electrophoresis,* vol. 23, pp. 2569-82, 08. 2002.

[70] D. Holmes, N. G. Green and H. Morgan, "Microdevices for dielectrophoretic flow - through cell separation," *IEEE Engineering in Medicine and Biology Magazine,* vol. 22, pp. 85-90, 11. 2003.

[71] J. Voldman, "Electrical forces for microscale cell manipulation," *Annu. Rev. Biomed. Eng.,* vol. 8, pp. 425-454, 2006.

[72] P. R. C. Gascoyne and J. Vykoukal, "Particle separation by dielectrophoresis." *Electrophoresis,* vol. 23, pp. 1973, 2002.

[73] L. Fu, G. Lee, Y. Lin and R. Yang, "Manipulation of microparticles using new modes of traveling-wave-dielectrophoretic forces: Numerical simulation and experiments," *IEEE/ASME Transactions on Mechatronics,* vol. 9, pp. 377-383, 2004.

[74] R. Pethig, M. S. Talary and R. S. Lee, "Enhancing Traveling-Wave Dielectrophoresis with Signal Superposition," *IEEE Engineering in Medicine and Biology Magazine,* vol. 22, pp. 43-50, 2003.

[75] G. Medoro, N. Manaresi, A. Leonardi, L. Altomare, M. Tartagni and R. Guerrieri, "A lab-on-a-chip for cell detection and manipulation," *IEEE Sensors Journal,* vol. 3, pp. 317-25, 06. 2003.

[76] V. Sundaram, H. Bang and H. J. Cho, "A DEP (dielectrophoretic) manipulator for bead-based assay using transparent ITO electrodes," in *IEEE Sensors 2004,* 2004, pp. 931-934.

[77] G. Lee and L. Fu, "Platform technology for manipulation of cells, proteins and DNA," in *2003 IEEE International Conference on Robotics and Automation,* 2003, pp. 3636-3641.

[78] J. H. Nieuwenhuis and M. J. Vellekoop, "Improved dielectrophoretic particle actuators for microfluidics," in *Proceedings of IEEE Sensors 2003,* 2003, pp. 573-7.

[79] K. H. Kang, Y. Kang, X. Xuan and D. Li, "Continuous separation of microparticles by size with direct current-dielectrophoresis," *Electrophoresis,* vol. 27, pp. 694-702, 02. 2006.

[80] M. Durr, J. Kentsch, T. Muller, T. Schnelle and M. Stelzle, "Microdevices for manipulation and accumulation of micro- and nanoparticles by dielectrophoresis," *Electrophoresis,* vol. 24, pp. 722-31, 02. 2003.

[81] J. Suehiro and R. Pethig, "The dielectrophoretic movement and positioning of a biological cell using a three-dimensional grid electrode system," *Journal of Physics D (Applied Physics),* vol. 31, pp. 3298-305, 11/21. 1998.

[82] C. Yu, J. Vykoukal, D. M. Vykoukal, J. A. Schwartz, L. Shi and P. R. C. Gascoyne, "A three-dimensional dielectrophoretic particle focusing channel for microcytometry applications," *J Microelectromech Syst,* vol. 14, pp. 480-487, 2005.

[83] J. T. Y. Lin and J. T. W. Yeow, "Enhancing Dielectrophoresis Effect Through Novel Electrode Geometry," *Biomedical Microdevices,* 2007.

[84] X. Wang, Y. Huang, X. Wang, B. F.F and G. P.R.C , "Dielectrophoretic manipulation of cells with spiral electrodes," *Biophys. J.,* vol. 72, pp. 1887-99, 1997.

[85] P. Gascoyne, C. Mahidol, M. Ruchirawat, J. Satayavivad, P. Watcharasit and F. F. Becker, "Microsample preparation by dielectrophoresis: isolation of malaria," *Lab on a Chip,* vol. 2, pp. 70-5, 05. 2002.

[86] A. D. Goater, J. P. H. Burt and R. Pethig, "A combined travelling wave dielectrophoresis and electrorotation device: applied to the concentration and viability determination of Cryptosporidium," *Journal of Physics D (Applied Physics),* vol. 30, pp. 65-9, 1997.

[87] Wikipedia. (2007, Jun 10). HeLa. [online]. *2007(Jun 12),* pp. 2. Available: http://en.wikipedia.org/wiki/HeLa

[88] Molecular Probes. (2006, Jan 24). Vybrant CFDA SE cell tracer kit. [online]. *2007(Jun 12),* pp. 4. Available: http://probes.invitrogen.com/media/pis/mp12883.pdf

[89] M. BRONNER-FRASER, "Alterations in Neural Crest Migration Antibody that Affects Cell Adhesion," *The Journal of Cell Biology,* vol. 101, pp. 610, 1985.

[90] Wikipedia. (2007, Apr 23). Pichia pastoris. [Online]. *2007(Jun 12),* pp. 1. Available: http://en.wikipedia.org/wiki/Pichia_pastoris

[91] Wikipedia. (2007, Apr 19). Hematopoietic stem cell. [Online]. *2007(Jun 12),* pp. 5. Available: http://en.wikipedia.org/wiki/Hematopoietic_stem_cell

[92] T. Muller, A. Pfennig, P. Klein, G. Gradl, M. Jager and T. Schnelle, "The potential of dielectrophoresis for single-cell experiments," *IEEE Engineering in Medicine and Biology Magazine,* vol. 22, pp. 51-61, 11. 2003.

[93] K. H. Schoenbach, R. H. Stark, J. Deng, R. E. -. Aly, S. J. Beebe and E. S. Buescher, "Biological/medical pulsed electric field treatments," in *50th Anniversary Edition,* 2000, pp. 42-6.

[94] S. B. Dev, D. P. Rabussay, G. Widera and G. A. Hofmann, "Medical applications of electroporation," *IEEE Trans. Plasma Sci.,* vol. 28, pp. 206-23, 02. 2000.

[95] W. D. Volkmuth and R. H. Austin, "DNA electrophoresis in microlithographic arrays," *Nature,* vol. 358, pp. 600-2, 08/13. 1992.

[96] L. Ulanovsky, G. Drouin and W. Gilbert, "DNA trapping electrophoresis," *Nature,* vol. 343, pp. 190-2, 01/11. 1990.

[97] H. Noguchi, "Dynamics of DNA electrophoresis in dilute and entangled polymer solutions," *J. Chem. Phys.,* vol. 112, pp. 9671-8, 06/01. 2000.